IMPLEMENTATION OF COUPLED THERMAL AND STRUCTURAL ANALYSIS METHODS FOR REINFORCED CONCRETE STRUCTURES

A THESIS SUBMITTED TO
THE GRADUATE SCHOOL OF NATURAL AND APPLIED SCIENCES
OF
MIDDLE EAST TECHNICAL UNIVERSITY

BY

UTKU ALBOSTAN

IN PARTIAL FULFILLMENT OF THE REQUIREMENTS
FOR
THE DEGREE OF MASTER SCIENCE
IN
CIVIL ENGINEERING

JANUARY 2013

Approval of the thesis:

IMPLEMENTATION OF COUPLED THERMAL AND STRUCTURAL ANALYSIS METHODS FOR REINFORCED CONCRETE STRUCTURES

submitted by **UTKU ALBOSTAN** in partial fulfillment of the requirements for the degree of **Master of Science in Civil Engineering Department, Middle East Technical University** by,

Prof. Dr. Canan Özgen
Dean, Graduate School of **Natural and Applied Sciences** ____________________

Prof. Dr. Ahmet Cevdet Yalçıner
Head of Department, **Civil Engineering** ____________________

Assoc. Prof. Dr. Özgür Kurç
Supervisor, **Civil Engineering Dept., METU** ____________________

Examining Committee Members:

Prof. Dr. Ahmet Yakut
Civil Engineering Dept., METU ____________________

Assoc. Prof. Dr. Özgür Kurç
Civil Engineering Dept., METU ____________________

Prof. Dr. Barış Binici
Civil Engineering Dept., METU ____________________

Assoc. Prof. Dr. Yalın Arıcı
Civil Engineering Dept., METU ____________________

Assoc. Prof. Dr. Görkem Külah
Chemical Engineering Dept., METU ____________________

DATE: ____________________

I hereby declare that all information in this document has been obtained and presented in accordance with academic rules and ethical conduct. I also declare that, as required by these rules and conduct, I have fully cited and referenced all material and results that are not original to this work.

Name, Last name : UTKU ALBOSTAN

Signature :

ABSTRACT

IMPLEMENTATION OF COUPLED THERMAL AND STRUCTURAL ANALYSIS
METHODS FOR REINFORCED CONCRETE STRUCTURES

Albostan, Utku
M.S, Department of Civil Engineering
Supervisor : Assoc. Prof. Dr. Özgür Kurç
January 2013, 105 pages

Temperature gradient causes volume change (elongation/shortening) in concrete structures. If the movement of the structure is restrained, significant stresses may occur on the structure. These stresses may be so significant that they can cause considerable cracking at structural components of large concrete structures. Thus, during the design of a concrete structure, the actual temperature gradient in the structure should be obtained in order to compute the stress distribution on the structure due to thermal effects. This study focuses on the implementation of a solution procedure for coupled thermal and structural analysis with finite element method for such structures. For this purpose, first transient heat transfer analysis algorithm is implemented to compute the thermal gradient occurring inside the concrete structures. Then, the output of the thermal analysis is combined with the linear static solution algorithm to compute stresses due to temperature gradient. Several, 2D and 3D, finite elements having both structural and thermal analysis capabilities are developed. The performances of each finite element are investigated. As a case study, the top floor of two L-shaped reinforced concrete parking structure and office building are analyzed. Both structures are subjected to heat convection at top face of the slabs as ambient condition. The bottom face of the slab of the parking structure has the same thermal conditions as the top face whereas in the office building the temperature inside the building is fixed to 20 degrees. The differences in the stress distribution of the slabs and the internal forces of the vertical structural members are discussed.

Keywords: Finite Element, Heat Transfer Analysis, Coupled Analysis, Thermal Gradient, Reinforced Concrete Structure.

ÖZ

BETONARME YAPILAR İÇİN ISI İLETİMİ VE YAPISAL ÇÖZÜMLEME METOTLARI KULLANILARAK İKİLİ ÇÖZÜMLEME YÖNTEMİNİN GELİŞTİRİLMESİ

Albostan, Utku
Yüksek Lisans, İnşaat Mühendisliği Bölümü
Tez Yöneticisi : Doç. Dr. Özgür Kurç
Ocak 2013, 105 sayfa

Betonarme yapılarda sıcaklık değişimi hacim değişikliğine (genleşme/büzülme) sebep olmaktadır. Eğer yapının eksenel yöndeki deformasyonu engellenirse yapı üzerinde ciddi mertebede gerilmelerin oluştuğu görülmektedir. Bu yüksek gerilmeler büyük betonarme yapılarda kırılma veya çatlamalara sebep olabilmektedir. Bu nedenle betonarme yapıların tasarımı sırasında, yapısal elemanlarda sıcaklık farklılıkları nedeniyle oluşan gerilme miktarlarının hesaplanabilmesi için, elemanlardaki sıcaklık dağılımı dikkate alınmalıdır. Bu çalışma betonarme yapıların sonlu elemanlar yöntemi ile geliştirilmiş ısı iletimi ve yapısal çözümleme yöntemleri ile ikili olarak çözümlenmesini incelemektedir. Bu amaçla ilk olarak zamana bağlı ısı iletimi çözümlemesi yapılarak betonarme elemanların içerisinde oluşan sıcaklık dağılımı elde edilmiştir. Sonrasında bu sıcaklık değerleri kullanılarak sistem yapısal olarak çözümlenmiş ve yapıdaki gerilme değerleri hesaplanmıştır. Bu çözümleme uygulamasında kullanılmak üzere 2 ve 3 boyutlu çeşitli sonlu elemanlar geliştirilmiştir. Bu elemanlar hem ısı iletimi hem de yapısal çözümlemelerde kullanılabilecek şekilde geliştirilmiş ve doğrulama testleri yapılmıştır. Test problemi olarak L şeklindeki betonarme park yeri yapısı ile ofis binasının en üst katları çözümlenmiştir. Her iki yapının çatı döşemesinin üst yüzeyine ısı konveksiyonu uygulanmıştır. Park yeri binasının çatı döşemesinin alt yüzeyine de üst yüzeye uygulanan ısı yükü aynen etki ettirilirken ofis binasının iç sıcaklığı 20 derecede sabit tutulmuştur. Her iki yapıda sıcaklık yükleri nedeniyle çatı döşemelerinde oluşan gerilmeler ve düşey elemanlarda oluşan iç kuvvetler karşılaştırılmıştır.

Anahtar Kelimeler: Sonlu Eleman, Isı İletimi Çözümlemesi, İkili Çözümleme, Sıcaklık Değişimi, Betonarme Yapılar.

To My Parents

ACKNOWLEDGEMENTS

I wish to express my utmost gratitude to my supervisor Assoc. Prof. Dr. Özgür Kurç for his guidance, advice, criticism, support, encouragements and insight throughout the research.

Assist. Prof. Dr. Serdar Göktepe is also sincerely acknowledged for his valuable support.

I am grateful for all continuous support, understanding and encouragement I have received from all of my family members, my mother Seval Albostan, my father, Erol Albostan, and my sister Duygu Albostan Yenerim and her husband Cengizhan Yenerim.

I would like to express sincere appreciation to my project members Tunç Bahçecioğlu and Tolga Kurt. I would also like to appreciate my friends for standing next to me during this process: Ali Baykara, Ezgi Berberoğlu, Başar Ataman, Aysim Damla Atalay, Muhammed Bulut, Oğuz Barın, Fırat Özel, Yunus Avcı, Hayati Arslan, Sadettin Uğur, Mehmet Tuna, and Mehmet Kemal Ardoğa. Finally, I would like to express my gratitude to Feyza Soysal for her continuous support and endless patience throughout this study and in all aspects of my life.

This study has been conducted with the funding provided by The Scientific and Technological Research Council of Turkey (TUBITAK) under the grant MAG108M586.

TABLE OF CONTENTS

APPENDICES

LIST OF FIGURES

FIGURES

LIST OF TABLES

TABLES

CHAPTER 1

INTRODUCTION

1.1. Problem Definition

Concrete is a composite material used commonly for any type of structures such as buildings, dams, pipes, roads, etc. due to its advantageous properties. In fact, its higher strength in compression, workability and being cheaper than the other construction materials are the reasons why concrete is the main construction material all over the world.

Concrete structures generally show volume change under four different time dependent effects; elastic deformation, creep, shrinkage and temperature change. Creep and shrinkage effects occur due to time dependent changes in the material properties. Indeed, creep mechanism is related to change of elastic properties of concrete with respect to time. In addition, temperature change, moisture content, humidity and stresses on the structure affect the mechanism of the creep. Similarly, shrinkage mechanism depends on moisture content and time. Unlike creep, it is independent of stress on the structure. Axial deformations due to temperature changes may cause significant stresses in structures with high degree of indeterminacy.

PTI, Post Tension Institute presents that according to ACI Committee 318, during the design of reinforced concrete structures, the aforementioned time dependent effects should be considered in serviceability and strength conditions. It also requires that these effects should be taken into account as reliable with the practical applications; accordingly, instead of upper bound values, more realistic conditions should be utilized. Current design approaches, however, use very simple assumptions and simple analysis methods for the consideration of time dependent axial deformations of concrete structures which may lead to excessive use of construction materials. Among the aforementioned time dependent effects, determination of maximum and minimum temperature gradient that can occur in the concrete structural components is always the problematic one. The common engineering approach is to use the yearly weather temperature information and come up with design temperature difference values. Unfortunately, this approach ignores the environmental conditions and heat transfer properties of concrete which might produce unrealistic design forces and stresses.

Change in temperature causes volume change (elongation/shortening) of the unrestrained structures without any stress if nonlinear thermal gradient is ignored. On restrained structures, however, stresses are generated due to the temperature gradient. Indeed, inability of thermal expansion/shortening causes stress on the body. Effects of temperature gradient depend on the volume of a structural component. For structural components with relatively small volumes such as columns, temperature change effects can be neglected. On the other hand, temperature gradient induces significant amount of stress on components with large volumes such as slab systems. For such components’ thermal stresses can cause significant cracking if necessary precautions are not taken.

Since concrete has low conductivity, temperature gradient occurs among the depth of the structure. This temperature gradient induces uneven stress distribution along the thickness of the structure. In addition, having high heat capacitance causes the change of the heat energy in the concrete structure slowly. In other words, the energy coming from the ambient conditions such as convection or radiation does not affect the inside of the section immediately. Therefore, warming and cooling of concrete structures occurs slowly and thus the temperature gradient of the concrete is not same with the temperature gradient of ambient. In order to consider these properties of concrete structures, more detailed solution procedures are required.

In this study, coupled, heat transfer and structural analyses, solution methods will be developed by utilizing finite element method. This way, thermal behavior of the reinforced concrete structure will be solved by considering the environmental thermal effects and actual temperature gradient in components of the structure will be obtained. Then, thermal strains due to thermal gradient will be computed and the structural solution will be performed. Accordingly, more realistic stress distribution and internal forces due to thermal gradient will be obtained.

1.2. Related Work

According to PTI, structures having large plans with short floor to floor distance such as parking structures are subjected to four different types of shortening. These are shortenings in post-tension slabs, creep, shrinkage and temperature change. In order to examine the effects of these four mechanisms, PTI analytically examined the floor shortening of a parking garage in Houston, Texas. According to the results of the example, the largest shortening occurs due to shrinkage with the percentage of 55%. Temperature change is the second largest shortening mechanism whose percentage is 27.7%. The percentages of elastic and creep shortenings are 8% and 9.3%, respectively. These results show that temperature change should not be ignored for designing of expansion joints for parking structures (PTI).

When a reinforced concrete structure is subjected to thermal loads due to temperature gradient, stress occurs on the structure if thermal expansion of the structure is restrained (Vecchio, 1987). Such stresses may cause cracking of the body. There are several techniques for represent the actual behavior of concrete structures under thermal loading. Temperature strains are calculated by multiplying thermal coefficient of concrete with temperature change values being maximum seasonal temperature changes for that location (PTI). This way, no temperature gradient through section thickness is taken into account.

Iqbal (2012) stated that most parking structures are concrete, open and unheated structures. Accordingly, creep, shrinkage and temperature affect such structures by changing volume. These effects induce displacements in structures. If these displacements are restrained, additional stresses occurs in the structure that cause crack, leaks and premature deterioration in the structure.

According to Iqbal (2012), in general, the duration of construction of such structures is more than one year. In order to simplify the determination of the construction temperature, T_c, mean value of the construction season is utilized. It was stated that minimum temperature, T_{min} is defined by Federal Construction Council (Technical Report No 65) as the equal or greater than the 99% of the temperature of winter months at that location. Accordingly, design temperature is calculated by utilizing the Equation 1-1.

$$T_{design} = T_{construction} - T_{min} \tag{1-1}$$

According to Saetta et al. (n.d.), for structures having large concrete bodies such as bridges or dams, temperature gradient occurs due to thermal loads; nevertheless, the difficulties of modeling the actual environmental conditions force designers to utilize simplified methods. This causes unreliable results. Accordingly, for analyzing such structures under thermal loads, temperature gradient occurring inside the concrete structure should be taken into account. For linear stress calculations, they followed three assumptions. First assumption is that heat transfer and structural analysis are performed independently (coupled analysis in weak form). The second one is utilizing small displacements and strains. Finally, linear elastic material properties are considered only.

By utilizing these three assumptions, Saetta et al. (n.d.) analyzed the Sa Stria dam, built in Sardegna (Italy) and a box girder bridge section subjected to climatic conditions of northern Italy. These structures were analyzed by utilizing coupled analysis in weak form. First, Sa Stria dam is a roller compacted concrete dam. They performed transient heat transfer solution to the dam by utilizing heat of hydration and heat convection conditions. This way, they obtained temperature gradient occurring in the dam body at several days. Then, they performed linear static analysis in order to obtain stresses on the dam body due to the temperature gradient. According to the results, tensile stress occurred near the edges where the temperature was lower; whereas, at core of the dam, compressive stress generated.

Similarly, Saetta et al. (n.d.) analyzed a box girder bridge section by utilizing actual thermal conditions such as heat convection, heat radiation etc. They applied coupled analysis in weak form and obtained temperature gradient and related stress and force distribution. According to the results, the maximum stress occurred in wings of the section. Accordingly, they indicated that if those regions are not designed properly, cracking may occur due to temperature gradient.

Vecchio stated that for continuous structures, thermal stress can be divided into two parts, primary and secondary thermal stresses (1987). Primary thermal stresses occur on unrestrained structures due to nonlinear thermal gradient through thickness. Indeed, since the thermal expansion coefficients of concrete and reinforcing bars are not same, internal restriction occurs between concrete and bars. Accordingly, internal stresses occur although the thermal expansion of the structure is not restrained. On the other hand, secondary thermal stresses generate on restrained structures. According to Vecchio (1987), the secondary thermal stresses are more critical than the first one.

Vecchio presented nonlinear frame analysis procedure for solution of reinforced concrete frames under thermal loading. The general solution procedure is the same with the most of the linear elastic frame analysis programs. On the other hand, this procedure provides to apply more factors such as nonlinear material, nonlinear thermal gradient, thermal creep, time history etc. Indeed, he added the effects of elevated temperatures to the physical and material properties such as strength or stiffness etc. He also implemented nonlinear temperature gradient through reinforced concrete section. He utilized the standard one dimensional heat transfer principals and he calculated the temperature values at any depth through thickness of the structure. Vecchio compared the performance of the solution procedure with the experimental results and obtained fair accuracy (1987).

In another paper, Vecchio et al. (1992) stated that reinforced concrete structures are subjected to thermal loads such as design function of the structure, ambient conditions, heat of hydration or fire. These loadings cause nonlinear temperature and strain profiles which produce increased level of stress, distortion and damage (i.e. primary thermal stresses). In addition to the primary thermal stresses, thermal loads induce restrained structural deformation (i.e. secondary thermal stresses). it was stated that second thermal stresses are more significant.

Vecchio et al. (1992) also stated that ACI Committee 349 includes less computation about the analysis of concrete structures under thermal load and this solution technique does not represent the actual behavior. In order to investigate the behavior of concrete shell structures under thermal load, they performed two tests. First, they tested concrete slab under both thermal and mechanical loadings. The slab was simply supported at each corner and concentrated load was applied to the center of the slab. In addition to mechanical load, the slab was subjected to heat at the top surface; whereas, temperature of bottom face was kept close to room temperature. Accordingly, temperature gradient was through the thickness. This test was repeated for different reinforcement ratios and orientations. The displacements at the center of the slab were compared with the analytical solutions. They computed analytical solution by utilizing the Equation 1-2.

$$\Delta_c = \frac{\alpha_c \Delta T l^2}{4h} \tag{1-2}$$

In Equation 1-2, Δ_c, h, l, α_c, ΔT are deflection at center of slab, thickness of slab, length of slab span, thermal expansion coefficient and temperature gradient, respectively. Since the slab was simply supported, no external stress due to thermal loading was expected. On the other hand, since reinforcement and concrete have different thermal coefficients, reinforcing bars restrained the slab; accordingly, internal stresses occurred in the slab body. In other words, nonlinear thermal gradient occurred. They, however, indicated that the effects of primary thermal stresses are negligible and no crack was occurred at the specimen during these tests.

Second, Vecchio et al. (1992) tested the same specimen under thermal load by restraining the center along thickness direction. This restriction caused stresses and related cracks on the slab. According to test results, internal forces increased up to occurring of first crack. This crack causes reduce in stiffness; accordingly, immediate relaxation occurred.

Chou and Cheng (n.d.) presented the study of measuring joint movements and seasonal thermal stresses of concrete slab located at the Chiang Kai-Shek international airport. They used optical fiber sensors to measure the joint displacements due to seasonal temperature change. These sensors were located at the middle layer of the slab through thickness and for approximately one year, displacements and temperature values had been stored. Since the sensors received temperature of only middle point layer, stresses on the slab were calculated with the assumption of constant temperature change along the thickness. They calculated stresses by considering the shrinkage mechanism also. According to their results, tensile stress will occur on concrete slab most of the time due to temperature changes if the casting of it is performed in hot temperatures. In addition to this, they made predictions about the future movement and thermal stresses by utilizing regression analysis.

According to Li et al. (2009), concrete slab bends if it is subjected to negative temperature gradient through thickness. This bending causes tensile stress at top layer of the slab. Although the maximum tensile stress is expected at the bottom layer of the slab, due to negative temperature gradient, it can occur at top layer. Accordingly, first cracking occurs at top layer. Because of this, they solved the system by acting the thermal and axle load together.

Li et al. (2009) utilized linear temperature gradient through thickness of the slab and solved the slab by considering each combination of axle load. This solution was performed by utilizing finite element method (FEM). According to their study, the maximum tensile stress occurred at top layer of the slab. This causes cracking from top to bottom; although, the designers in China expected cracks from bottom to top. On the other hand, these results are obtained from a structural model composed of a single slab. Behavior of an indeterminate system was not considered.

Thelandersson stated that thermal loading can be added to the mechanical analysis as initial strain for both linear and nonlinear solutions (1987). According to Thelandersson, this approach was developed for metals; whereas, for concrete, the mechanism is more complex than stated above because mechanical properties depend on temperature. Accordingly, Thelandersson stated change of strain by utilizing the Equation 1-3.

$$\dot{\varepsilon}_{ij} = -\frac{v}{E}\dot{\sigma}_{kk}\delta_{ij} + \frac{1+v}{E}\dot{\sigma}_{ij} + [(\alpha + \beta_1\sigma_{kk})\delta_{ij} + \beta_2\sigma_{ij}]\dot{T} \tag{1-3}$$

Where

$$\beta_1 = \frac{d}{dT}(-\frac{v}{E}) \tag{1-4}$$

$$\beta_2 = \frac{d}{dT}(\frac{1+v}{E}) \tag{1-5}$$

β_1 and β_2 represent change of elastic properties of concrete with respect to temperature and if these elastic properties are independent of temperature, isotropic linear thermo-elastic material behavior is obtained (Thelandersson, 1987). Thelandersson developed constitutive material model including the derivatives of elastic properties and verified the method with experimental results. According to the results, this tangent modulus gives reliable results; although, it is simple.

Borst and Peters presented the material behavior of concrete under elevated temperatures (1988). Indeed, they indicated that concrete behaves nonlinear under elevated temperature due to thermal dilatation, temperature dependent material properties, transient creep, and cracking. Transient creep mechanism includes both thermal expansion with thermal expansion coefficient whose function is nonlinear of the temperature and change of elastic properties of the material such as Modulus of elasticity etc.

According to Borst and Peters (1988), large scale structures should be solved by utilizing smeared crack formulation. Otherwise, reliable results are not obtained. However, derivation of the material behavior composed of smeared crack and other nonlinear mechanisms stated above is not appropriate. Accordingly, they utilized strain decomposition approach to handle this problem. Indeed, they used separate constitutive law for each strain rate. They simulated the test of plain concrete cylinders. They stated that this test was conducted by Anderberg and Thelandersson (1978) in order to discover the mechanical behavior under high temperatures. This simulation reveals that analysis of concrete structure does not represent the actual behavior if transient creep is not taken into account.

1.3. Objectives and Scopes

The main objective of this study is the development of finite element solution platform that enables the coupled, thermal and structural, analysis of civil engineering structures. This allows the detailed investigation of stress caused by thermal effects in any structure of any geometry.

For this purpose, linear heat transfer and linear structural analysis solution algorithms are combined as weak form of coupled analysis. Since for structural solutions, no significant geometry change is generated, thermoelastic property of the material may be ignored. Accordingly, weak form of coupled analysis is preferred. In other words, linear heat transfer analysis and linear structural analysis are performed in sequential order. Heat transfer analysis computes temperature values of certain locations at a body for a certain time period and structural analysis uses these temperature values for calculating the thermal strains. These thermal strains are then converted to equivalent nodal forces and the corresponding deformations are computed.

In addition, several types of 2D and 3D finite elements will be developed. This way, structures with complex geometries can also be analyzed. Each element will include both structural analysis and heat transfer solution related algorithms. Moreover the performance of each element for both cases for several benchmark problems will be investigated.

By utilizing the developed solution algorithms, the top floor of a typical L-shaped building will be analyzed as a case study. Indeed, the building will be solved twice with different thermal conditions. First, it will be analyzed as a parking structure being open and subjected to ambient temperature conditions only. For the second case, the same building will be analyzed as an office building thus the internal temperature of the building will be fixed to 20^{O}C. Both structures will be subjected to heat convection with ambient temperature of Adana at July 23rd (Bulut et al., n.d.) but the heat radiation effect will be ignored. Also, heat convection occurring on the columns and walls are neglected. Casting temperature of the structure is assumed to be equal to 14^{O}C and temperature gradient of slab through thickness for only one day will be investigated. For several hours of that day, stresses on the slab due to temperature gradient at that time will be calculated and compared with each other.

For both the heat transfer and structural analyses, all material properties will be assumed as linear. In other words, effects of nonlinear stress - strain relationship, nonlinear temperature gradient, transient creep, and shrinkage will be ignored. Only stresses generated due to temperature change will be discussed.

1.4. Thesis Outline

Outline of the thesis is as follows. Theory of solution methods of solid mechanics and heat transfer and finite element procedures are discussed in Chapter 2. All implementations are presented in Chapter 3. In this chapter, structures of solution algorithms, linear structural and linear heat transfer analysis and coupled system are presented. In addition, finite elements existing in finite element library of the platform and their basic properties are explained. Chapter 4 includes verification of the solution algorithms and finite elements stated in Chapter 3. Behaviors of L-shaped concrete structures under different thermal loads are going to be discussed in Chapter 5. Indeed, parking and office structures having same geometry and different thermal loading conditions are compared. Finally, Chapter 6 is conclusion part of the thesis. In addition to these, properties of integration points used for calculation of integrals numerically are tabulated in the appendices.

CHAPTER 2

THEORY

2.1. Introduction

In this chapter, theories used for this study are explained. Theory of solution algorithms, structural, heat transfer and coupled analysis equations and finite element method are discussed. Indeed, general equations of each solution method, structural analysis and heat transfer, and adapting them to finite element method are explained briefly. Moreover, theory of the coupled analysis procedure derived by utilizing these heat transfer and structural analysis solution is discussed.

2.2. Structural Analysis

Structural analysis solution is derived from principals of thermodynamics with the assumption of having uniform and constant temperature distribution over the body. The strong form of general mechanical equation second order differential equation is presented in Equation 2-1.

$$\rho \ddot{u} = C{:}\, u'' + \rho b \tag{2-1}$$

In Equation 2-1, ρ, C, b, and u indicate density, constitutive material matrix, body load and displacement, respectively. This equation can be rewritten in Galerkin functional form by using integration by parts and Gauss integral theorems (Equation 2-2).

$$G(u, \delta \mathrm{u}) = \int_V \delta \mathrm{u}\, \rho \ddot{u}\, dV - \int_S \delta \mathrm{u}\, (C{:}\, u')n \;\, dS + \int_V \delta \mathrm{u}' C{:}\, u' \;\, dV - \int_V \delta \mathrm{u} \;\, \rho b \; dV = 0 \tag{2-2}$$

In Equation 2-2, δu represent test function and it is zero at boundary. According to finite element discretization yields the following expressions.

$$\mathrm{u} = N\mathrm{d} \qquad \nabla \mathrm{u} = \nabla N d = \mathrm{B\ d} \qquad \ddot{u} = N\ddot{d}$$

$$\delta \mathrm{u} = N\delta \mathrm{d} \qquad \nabla \delta \mathrm{u} = \nabla N \delta \mathrm{d} = \mathrm{B}\ \delta \mathrm{d} \qquad \delta\ddot{\mathrm{u}} = N\delta\ddot{\mathrm{d}} \tag{2-3}$$

In Equations 2-3, d represents the element displacement vector and N is shape function. Inserting definitions (Equation 2-3) into the Galerkin functional yields to the Equation 2-4.

$$\int_V \delta d^T N^T \rho N \ddot{d}\, dV - \int_S \delta d^T N^T \;\mathrm{t}\;\, dS + \int_V \delta d^T B^T C{:}\, \mathrm{B\ d}\;\, dV - \int_V \delta d^T N^T \rho b \; dV = 0 \tag{2-4}$$

By rearranging the Equation 2-4, Equation 2-5 is obtained.

$$\sum_{e=1}^{n_{element}} \delta d^T \left(\int_V N^T \rho N \ddot{d}\, dV - \int_S N^T \;\mathrm{t}\;\, dS + \int_V B^T C{:}\, \mathrm{B\ d}\;\, dV - \int_V N^T \rho b \; dV\right) = 0 \tag{2-5}$$

Equation 2-5 may be stated in terms of internal and external forces (Equation 2-6).

$$\sum_{e=1}^{n_{element}} \delta d^T (f_{int} - f_{ext}) = 0$$

$$f_{int} = \int_V N^T \rho N \ddot{d}\, dV + \int_V B^T C\!:\mathrm{B\ d}\ dV$$

$$f_{ext} = \int_S N^T \mathrm{t}\ dS + \int_V N^T \rho b\ dV \tag{2-6}$$

For arbitrary test function δd the following equation (Equation 2-7) should be satisfied.

$$f_{int} = f_{ext} \tag{2-7}$$

The equation 2-6 implies that internal forces are function of nodal displacements, d.

$$f_{int} = \widehat{f_{int}}(d) \tag{2-8}$$

Therefore, internal forces may be expressed in matrix form (Equation 2-9).

$$f_{int} = M_e \ddot{d} + K_e \mathrm{d}$$

$$M_e = \int_V N^T \rho N\, dV$$

$$K_e = \int_V B^T C\!:\mathrm{B}\ dV \tag{2-9}$$

M_e and K_e stated in Equation 2-9 are element mass and stiffness matrices, respectively. In Equation 2-9, strain-displacement relation matrix is indicated with letter B and calculated from Equation 2-10.

$$B = \begin{bmatrix} \frac{\partial N_1}{\partial x} & \cdots & \frac{\partial N_m}{\partial x} \\ \frac{\partial N_1}{\partial y} & \cdots & \frac{\partial N_m}{\partial y} \\ \frac{\partial N_1}{\partial z} & \cdots & \frac{\partial N_m}{\partial z} \end{bmatrix} \tag{2-10}$$

Equation 2-10 is valid for 3D finite elements; whereas, B matrix of a 2D element has two rows. In other words, it includes derivative of shape functions with respect to two axes. In this equation, number of shape functions indicated with letter of m. Matrix form of general structural analysis equation (Equation 2-2) is presented in Equation 2-11.

$$M\ddot{d} + K\mathrm{d} = F \tag{2-11}$$

In Equation 2-11, M, K, F and d are mass and stiffness matrices and external force and displacement vectors, respectively. For linear static solution, time derivative of the displacement is zero. Accordingly, Equation 2-11 is simplified and general linear static equation (Equation 2-12) is obtained.

$$K\mathrm{d} = F \tag{2-12}$$

In the Equation 2-12, since the system is linear, stiffness matrix is computed by using initial geometry and linear material properties. The external force vector can be calculated as Equation 2-13.

$$F = F_{nodal} + F_{element} \tag{2-13}$$

External force vector can be divided into two parts, nodal loads and element loads (Equation 2-13). Nodal loads come from input directly. On the other hand, element loads are calculated by using the element geometry and material properties and converted to equivalent nodal loads. There are four different types of element loads; body load, surface load, thermal load, initial strain load presented in Equations 2-14 to 2-17, respectively.

$$F_{body} = \int_V N^T b dV \quad (2\text{-}14)$$

$$F_{Surface} = \int_S N_{surface}^T W dV \quad (2\text{-}15)$$

$$F_{thermal} = \int_V B^T C(\Delta t\ a) dV \quad (2\text{-}16)$$

$$F_{strain} = \int_V B^T C \varepsilon_{initial}\, dV \quad (2\text{-}17)$$

In Equations 2-14 to 2-17, W, Δ_t, a and ε represent uniform surface load, temperature change, thermal coefficient and strain vector, respectively.

In Equation 2-16, thermal load due to constant temperature change over body is calculated. Whereas, since in coupled analysis, nodal temperature change values are obtained from heat transfer solution, modification of calculation of thermal load is required. In fact, thermal strains and corresponding stresses due to temperature change at each nodal point are calculated (Equations 2-18 and 2-19). Then, these nodal stress values contribute to calculation of equivalent nodal load with the rate of weight value of the corresponding integration points. Numerical integration of calculation of equivalent load vector is presented in Equation 2-20.

$$\varepsilon_i = [\Delta t_i * a \quad \Delta t_i * a \quad \Delta t_i * a \quad 0 \quad 0 \quad 0]^T \quad (2\text{-}18)$$

$$\sigma_i = C\ \varepsilon_i \quad (2\text{-}19)$$

$$F_{equivalent} = \sum_{i=1}^{m} B_i^T \sigma_i |J_i| w_i \quad (2\text{-}20)$$

In equations 2-18 to 2-20, σ and w are stress vector and weight value of the integration point scheme.

Each integral is handled numerically by utilizing Gauss Quadrature rule. Some integration point schemes cause problematic element behaviors such as shear/ membrane locking or hourglassing modes etc. First, shear/membrane locking occurs in linear elements if full integration scheme is utilized (Dhondt, 2004). As a matter of fact, under pure bending load case, there is no shear strain in the body since no shear force exists. However, if full integration scheme is used, virtual shear strains occur at gauss points existence of shear strain makes the behavior stiffer. On the other hand, utilizing reduced integration scheme hinders generation of shear locking since virtual shear strain does not occur at center of the element.

The other problematic behavior is hourglassing mode called also zero energy mode. It occurs if displacement modes of element do not create any strain and stress at the integration points (Dhondt, 2004). Presence of this problematic behavior can be checked by using the Equation 2-21 (Dhondt, 2004).

$$nZEM = (nd * n) - (nIP * nS) - nRBM \quad (2\text{-}21)$$

In Equation 2-21, *nZEM*, *nd*, *n*, *nIP*, *nS*, and *nRBM* represent numbers of zero energy modes, degree of freedoms, nodes, integration points, strain components and rigid body modes, respectively. As seen in the equation, this problem can be handled by increasing the number of integration points.

2.3. Heat Transfer Analysis

The heat transfer occurs due to energy transfer between material bodies because of their temperature difference (Lewis et al., 2004). There are three different ways of energy transport:

- Conduction
- Convection
- Radiation

Conduction

Conduction mode occurs by transporting energy from one molecule to another without any motion of these molecules (Lewis et al., 2004). Therefore, conduction mode heat transfer occurs between solid bodies.

This mode can be explained by Fourier's law. The transferred energy per unit time and per unit area is presented in Equation 2-22.

$$q = -k\,(\nabla\theta) \tag{2-22}$$

In Equation 2-22, q, k, and divergence of θ represent heat flux (W/m^2), thermal conductivity ($W/m^{O}K$) and temperature gradient ($^{O}K/m$), respectively.

Convection

Convection mode comes into existence by transferring energy from one molecule to another with free motion of molecules belonging to liquids or gases (Lewis et al., 2004). Because of this, heat transfer between a solid and fluid can be described by heat convection. There are two types of convection; forced convection and free convection. In forced convection, fluid is sent to the solid material with an external force such as pump or fan; whereas, there is no external contribution in free convection.

Convection heat transfer can be described by Newton's law of cooling. The transferred energy per unit time can be calculated with Equation 2-23.

$$qn = h(\,\theta\,-\,\theta\,a) \tag{2-23}$$

In Equation 2-23, convection heat transfer coefficient ($W/m^2\,{}^{O}K$) and temperature difference between body and fluid (^{O}K) are symbolized with h and θ-θ_a, respectively. The direction of heat flux stated in Equation 2-23 is perpendicular to the boundary.

Radiation

Lewis et al. states that the radiation occurs in all bodies at all temperature. In fact, all bodies transfer their energy by emitting radiation (2004). Because of this, it is not required to contact between bodies to change their temperatures. When the radiation waves emitted by a body hit to surface of another body, some of these waves are reflected, some part is transmitted, and the remaining part is absorbed (Lewis et al., 2004).

Stefan – Boltzmann law is related with radiative heat transfer mode. The transferred energy per unit time is found by Equation 2-24.

$$qn = \sigma\,\theta^{4} \qquad (2\text{-}24)$$

In Equation 2-24, θ and σ are surface temperature (^{O}K) and Stefan – Boltzmann constant ($5.669*10^{-8}$ W/m^2 ^{O}K^4), respectively. Similar to heat convection, the direction of heat flux is perpendicular to the boundary.

Formulation of Heat Transfer

Total energy in current direction is calculated by multiplying the flux with the perpendicular area (Equation 2-25).

$$Q = qA \qquad (2\text{-}25)$$

According to conservation of energy law, energy storage in a system is equal to the difference between the inlet energy and outlet energy. Conservation of energy law is displayed in Equation 2-26.

$$\frac{dQ_{stored}}{dt} = \frac{dQ_{in}}{dt} - \frac{dQ_{out}}{dt} \qquad (2\text{-}26)$$

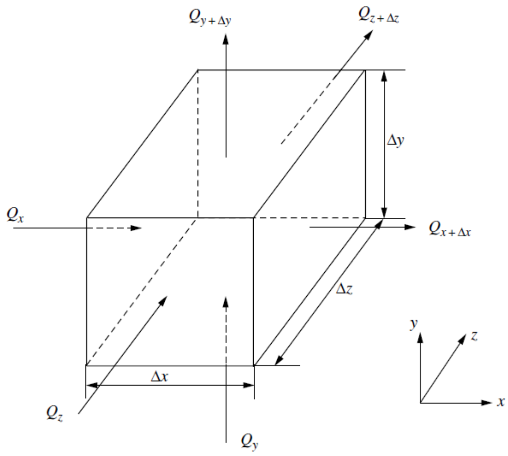

Figure 2-1 Control Volume (Lewis et al., 2004)

In Figure 2-1, control volume of a body and inlet/outlet heat energies are represented. The output energies can be redefined by substituting Taylor Series expansion without higher terms (Equation 2-27).

$$Qx + dx = Qx + \frac{\partial Qx}{\partial x}\Delta x$$

$$Qy + dy = Qy + \frac{\partial Qy}{\partial y}\Delta y$$

$$Qz + dz = Qz + \frac{\partial Qz}{\partial z}\Delta z \qquad (2\text{-}27)$$

Moreover, the heat generation and rate of energy storage of control volume are presented in Equations 2-28 and 2-29, respectively.

$$Q = G\ \Delta x \Delta y \Delta z \tag{2-28}$$

$$\frac{dQ_{stored}}{dt} = \rho c_p \frac{\partial\, \theta}{\partial t} \Delta x \Delta y \Delta z \tag{2-29}$$

In Equation 2-28, G is rate of internal heat generation per unit volume (W/m³). Similarly, in Equation 2-29, ρ and c_p indicate density and specific heat, respectively. Substituting Equations 2-27, 2-28 and 2-29 into conservation of energy equation (Equation 2-26) yields the general equation of heat transfer (Equation 2-30).

$$-\frac{\partial Qx}{\partial x}\Delta x - \frac{\partial Qy}{\partial y}\Delta y - \frac{\partial Qz}{\partial z}\Delta z\ + G\ \Delta x \Delta y \Delta z\ = \rho \Delta x \Delta y \Delta z c_p \frac{\partial\, \theta}{\partial t} \tag{2-30}$$

Simplified form of Equation 2-30 is presented in Equation 2-31.

$$-\nabla q_c + \mathrm{G} + q_C + q_r =\ \rho c_p\ \dot{\theta} \tag{2-31}$$

In Equation 2-31, q_c, q_C, and q_r are conduction, convection and heat radiation fluxes, respectively. Similar to structural analysis equation, Equation 2-31 can be solved by utilizing Galerkin functional. Galerkin functional form of the general heat transfer equation is presented in Equation 2-32.

$$G(\theta, \delta\theta) = -\int_V \delta\theta\ \nabla q_c dV + \int_S \delta\theta q_s dS + \int_V \delta\theta G dV - \int_V \delta\theta \rho c_p\ \dot{\theta}\ dV = 0 \tag{2-32}$$

In Equation 2-32, $\delta\theta$ is test function which is zero at boundaries and surface flux, q_s includes both heat convection and heat radiation fluxes. By utilizing integration by parts and Gauss integral theory, rearranged form of Equation 2-32 is obtained (Equation 2-33).

$$-\int_S (\delta\theta q_c) n dS + \int_V \nabla\delta\theta q_c dV + \int_S \delta\theta q_s dS + \int_V \delta\theta\rho G dV - \int_V \delta\theta\rho c\dot{\theta} dV = 0 \tag{2-33}$$

Finite element discretization of heat transfer equation yields to the following expressions.

$$\theta = N\mathrm{T} \qquad \nabla\theta = \nabla N\mathrm{T} = B\ \mathrm{T} \qquad \dot{\theta} = N\dot{T}$$

$$\delta\theta = N\delta\mathrm{T} \qquad \nabla\delta\theta = \nabla N\ \delta\mathrm{T} = B\ \delta\mathrm{T} \qquad \dot{\delta\theta} = N\dot{\delta T} \tag{2-34}$$

In Equations 2-34, T represents the element temperature vector and N is shape function of the element. Inserting definitions stated above into the Galerkin functional yields to the Equation 2-35.

$$\int_V \delta\mathrm{T}^T B^T q_c dV - \int_S \delta\mathrm{T}^T N^T \mathrm{h}(N\mathrm{T} -\ \theta\ a) dS - \int_S \delta\mathrm{T}^T N^T \sigma (N\mathrm{T})^4 dS + \int_V \delta\mathrm{T}^T N^T \rho G dV - \int_V \delta\mathrm{T}^T N^T \rho c_p\ N\dot{T} dV = 0 \tag{2-35}$$

Equation 2-35 can be written in matrix form (Equation 2-36).

$$C_e \dot{T} + K_e T = F \tag{2-36}$$

In Equation 2-36, C_e and K_e are element heat capacitance and thermal stiffness matrices and they are presented in Equations 2-37 and 2-38, respectively.

$$C_e = \int_V N^T \rho c_p N \, dV \tag{2-37}$$

$$K_e = \int_V B^T k \mathrm{B} \; dV + \int_S N^T h N \, dS \tag{2-38}$$

In Equation 2-38, stiffness matrix includes conduction and convection modes first and second term, respectively. Thermal forces, however, do not depend on element temperature vector. It is possible to separate element thermal forces into groups such as heat generation, heat convection, heat radiation and surface flux forces (Equation 2-39).

$$f_{ext} = f_{heat\ generation} + f_{heat\ convection} + f_{surface\ flux}$$

$$f_{heat\ generation} = \int_V N^T \rho G \, dV$$

$$f_{heat\ convection} = \int_S N^T \mathrm{h} \, \theta a \, dS$$

$$f_{heat\ radiation} = \int_S N^T \sigma (N\mathrm{T})^4 \, dS$$

$$f_{surface\ flux} = \int_S N^T \mathrm{qn} \, dS \tag{2-39}$$

In this study, radiation part was ignored; accordingly, there are three different thermal loadings, heat generation, heat convection, and surface flux (Equation 2-39). The direction of surface flux loading is inward to the body.

There are two boundary conditions of differential equation of heat transfer physic; constant nodal temperatures and surface flux. Indeed, constant temperature and surface flux are essential and Neuman boundary conditions, respectively (Equation 2-40). Surface flux boundary condition can include heat convection, heat radiation, and external flux.

Essential BC: $\theta = \theta_B$

Neuman BC: $q = q_B, \; q = h(\theta - \theta_a), \; q = \sigma\theta^4, \; q = 0$ (2-40)

2.4. Coupled Analysis Methods

The term coupled analysis refers to the combined analysis of multi-physics problems. There are two ways of coupled solution, strong and weak formulation.

In strong form, different physics analyses are performed at the same time. Therefore, each effect of these analysis types is included in solution of the problem. Strong form of coupled analysis equation in matrix form is presented in Equation 2-41.

$$\begin{bmatrix} K_{11} & K_{12} \\ K_{21} & K_{22} \end{bmatrix} \begin{Bmatrix} X_1 \\ X_2 \end{Bmatrix} = \begin{Bmatrix} F_1 \\ F_2 \end{Bmatrix} \tag{2-41}$$

In equation stated above, X_1 and X_2 represent solution vectors of two different physics. K and F are stiffness matrix and force vector, respectively. Indeed, first and second rows indicate different types of analysis systems. These two analysis systems are connected to each other due to K_{12} and K_{21} matrices.

On the other hand, in weak form of coupled analysis, different physics analyses are performed, sequentially. In other words, first one analysis system is performed and results of it implemented to the other solution system. Then the second analysis is executed. The matrix form of coupled analysis in weak form is presented in Equation 2-42.

$$\begin{bmatrix} K_{11} & 0 \\ 0 & K_{22} \end{bmatrix} \begin{Bmatrix} X_1 \\ X_2 \end{Bmatrix} = \begin{Bmatrix} F_1 \\ F_2 \end{Bmatrix} \tag{2-42}$$

Unlike strong form, off diagonal terms are zero matrices in weak form solution. This makes these analysis systems unbounded. However, force vector of second analysis system includes not only external load of it but also loads due to solution of first equation. This loading is the only connection between these equations.

Due to having unbounded stiffness matrix, weak form requires less memory during execution and implementation of it is easier than the strong form.

CHAPTER 3

IMPLEMENTATION

3.1. Introduction

In this chapter, implementation of solution algorithms and finite elements used for this study are discussed. In fact, linear static analysis algorithm, linear heat transfer algorithms (steady-state and transient) developed for this study, and coupled analysis system obtained by executing heat transfer and structural analysis algorithms sequentially, are explained. In fact, procedure of linear static and linear steady state algorithms solve linear system of equations. On the other hand, time integration schemes are used for solution of transient heat transfer algorithm. Finally, for coupled analysis, either steady-state or transient heat transfer solution and linear static algorithm are performed, sequentially.

Moreover, several two and three dimensional finite elements were developed. Each element has two formulation types, linear and quadratic and is suitable for two different physics problems, structural analysis and heat transfer. In structural analysis part, elements have routines required for linear static analysis such as calculation of linear stiffness matrix, internal force and element stress vectors. Moreover, they have the capability of converting element loads such as body load, surface load, temperature differences and initial strain to equivalent nodal loads. In addition to structural analysis part, each element has linear heat transfer analysis routines such as calculating linear conduction, heat capacitance and various types of loading such as heat convection, surface flux, and heat generation.

3.2. Structure of Panthalassa

For implementation of the new solution algorithms and finite element models, a finite element analysis platform, Panthalassa was used (Kurç et al., 2012). Panthalassa is an extensible finite element analysis environment which was developed by using C++ language with object-oriented data structure (Bahçecioğlu et al., 2012). Panthalassa includes an analysis engine that performs data input/output, handling of the structural objects, such as finite elements, loading definitions etc., and general routines such as matrix assembly, solution etc. the design of the engine allows addition of new solution algorithms, material models or finite elements externally as plug-in modules.

In this study, owing to extensibility property of the platform, several two and three dimensional finite element models and linear heat transfer solution algorithms were developed and added to the platform in the plug-in format. In fact, Panthalassa has virtual classes such as element, material model and solution algorithm etc. and these virtual classes let user to develop a new class including same properties with them and be implemented to the platform in plug-in format (Kurç et al., 2012). Because of this, heat transfer analysis plug-in having linear steady-state and transient solution algorithms can reach the model properties such as loading and boundary conditions from the platform and give the results to it. Similarly, each finite element reaches the geometry and material property of the system and gives the element matrices such as stiffness or stress etc. This process is illustrated in Figure 3-1.

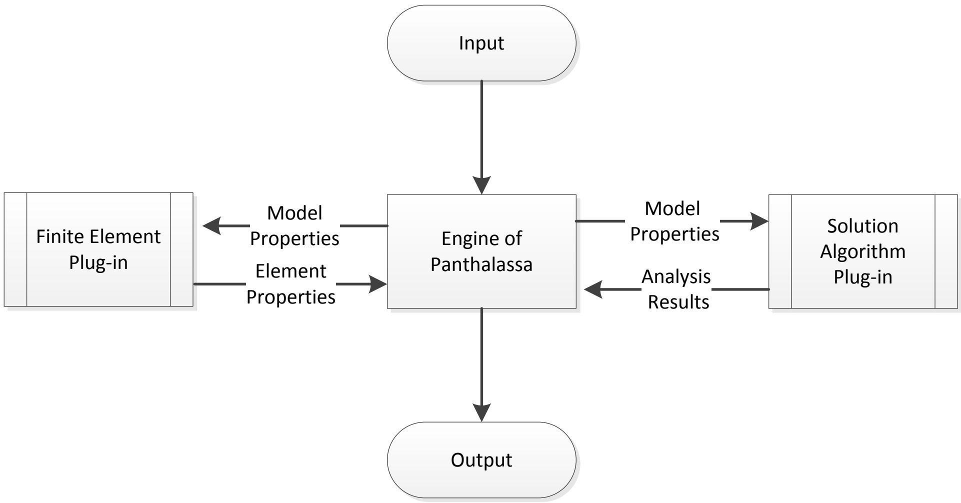

Figure 3-1 Connections of Plug-ins with Panthalassa Engine

3.3. Solution Algorithms

In this section, structure and implementation to the Panthalassa platform of solution algorithms, linear static and linear heat transfer (steady-state and transient) and coupled analysis with these two solutions are discussed.

3.3.1. Linear Static Analysis

In the linear static analysis for structural analysis problems, basically the equation system presented in Equation 3-1 is formed and solved. For the solution of the linear system of equations, LU decomposition method stated in MUMPS library is used (Kurç et al. 2012).

$$KU = F \tag{3-1}$$

In Equation 3-1, K, F, and U indicate stiffness matrix, nodal force vector, and nodal displacement vector, respectively. Nodal force vector includes both external nodal load and equivalent nodal loads due to element loads. Equivalent nodal loads of each element are computed by the subroutines of the element plug-ins and assembled by the subroutines of the solution algorithm plug-in utilizing the service routines of the Panthalassa Engine.

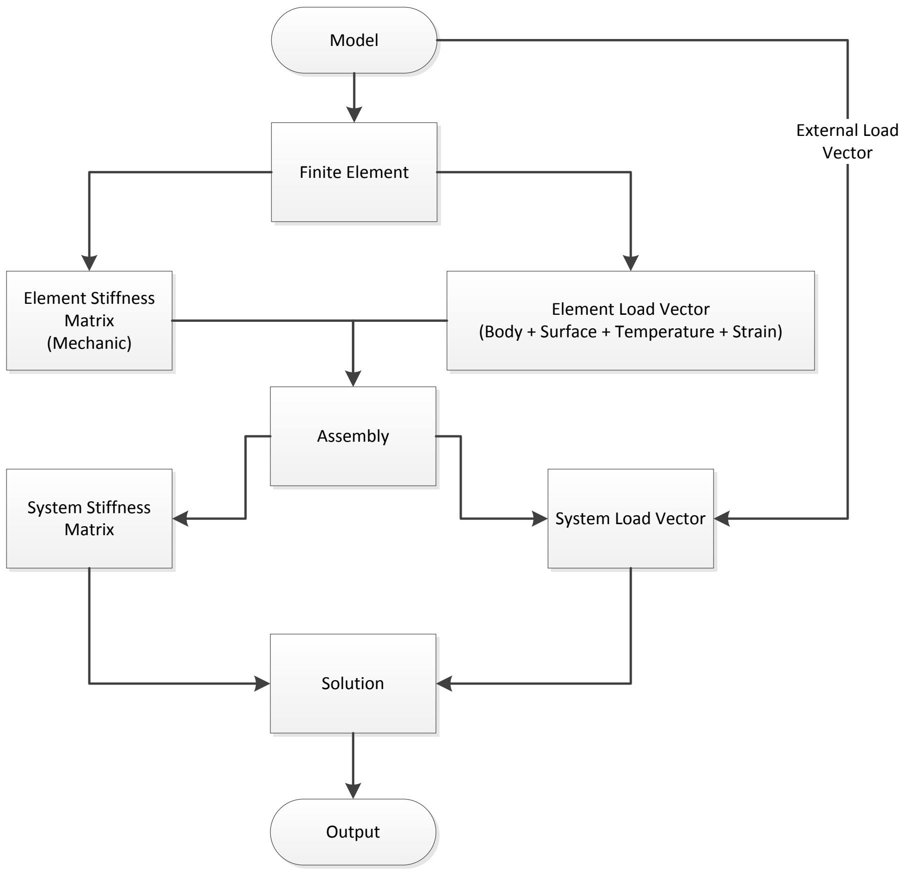

Figure 3-2 Flow Chart of Linear Static Analysis Algorithm

In Figure 3-2, flow chart of linear static analysis algorithm is presented. In fact, element stiffness matrix and equivalent element nodal load vector are computed by each finite element and they are assembled into to the system stiffness matrix and system nodal force vector. Such assembly operations are handled by Panthalassa routines automatically; whereas, the element loads computations are performed at the algorithms of the plug-ins. As the stiffness matrix and the force vector of the whole structure are obtained, they are solved by the LU decomposition based solver routines of Panthalassa and the nodal displacements are computed. By using the element nodal displacements, element stresses and forces are calculated. As a final step, nodal displacements and element stresses are written to the output file for post processing.

3.3.2. Linear Heat Transfer Analysis

The basic equation for the general heat transfer problem in matrix form is presented in Equation 3-2.

$$C\dot{\theta} + K_t\theta = F_t(t) \tag{3-2}$$

In the above equation, heat capacitance matrix, thermal stiffness matrix, thermal load vector, and nodal temperature vector are represented by letters C, K_t, $F_t(t)$, and θ, respectively.

The general heat transfer equation can be solved in two ways. In the first approach, called steady-state solution, time derivatives of temperatures are ignored. This way the solution of the equation is significantly simplified. This solution way gives the final equilibrium condition of the structure under given loads. Therefore, it is not possible to obtain time required for equilibrium condition like linear static analysis. Since the solution performs only once, duration of solution is not significant. On the other hand, linear transient solution uses time integration scheme for solution. Since the structure is solved for each time step, it consumes more time than the steady state way. However, transient solution calculates the behavior of the structure even if equilibrium condition has not been satisfied yet. Since this solution needs heat capacitance matrix, C and essential boundary conditions, more memory is required.

Linear Steady-State Analysis

Steady-state analysis system assumes no change of temperature with respect to time. Therefore, Equation 3-2 is simplified and general steady-state heat transfer analysis equation is obtained (Equation 3-3). In the linear steady-state analysis approach, K_t does not change with respect to temperature values.

$$K_t\theta = F_t \tag{3-3}$$

In the computational point of view, steady-state heat transfer analysis equation is similar to the linear static analysis equation (Equation 3-1). On the other hand, forming the thermal stiffness matrix and thermal load vector is quite different than the linear static analysis. First of all, heat stiffness matrix is composed of conduction and convection stiffness matrices. Conduction stiffness matrix is calculated by using material and geometric properties of the element; whereas, heat convection loading on the element influences the convection stiffness matrix in addition to the material and geometric properties of the element. Heat convection surface load also contributes to nodal load vector with ambient temperature. Flow chart of matrix assembly of heat transfer analysis algorithm is shown in Figure 3-3.

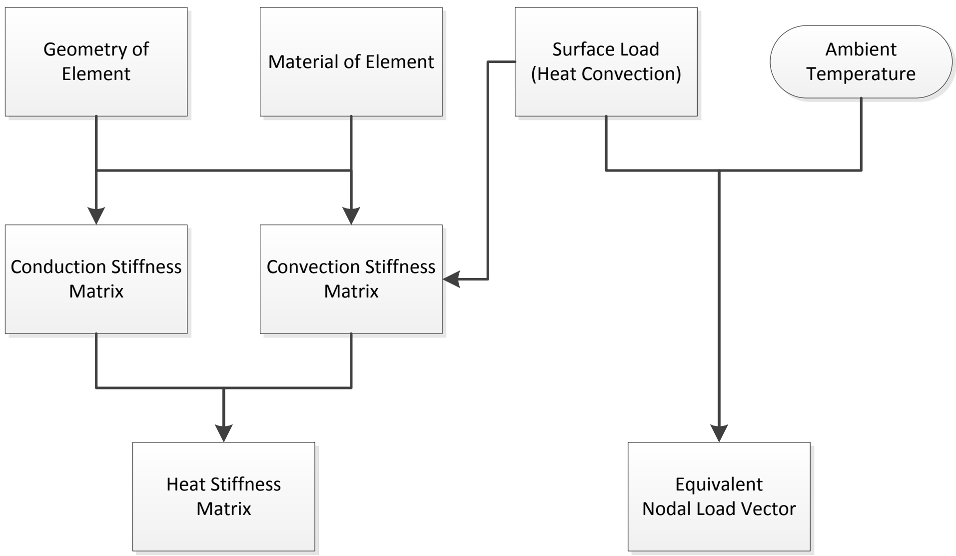

Figure 3-3 Flow Chart of Matrix Assembly of Heat Transfer Solution Algorithm

Three different boundary conditions, constant temperature, heat convection, and surface flux can be described for heat transfer problems. Constant temperature condition is defined at nodal points and taken into account as restraints. Whereas, heat convection and surface flux conditions need boundary definition. For Panthalassa, boundary of an element is defined by giving the element nodal ids of that boundary.

Element loads of heat transfer problems, heat convection, surface flux, and heat generation, are handled by element plug-ins and sent to the algorithm plug-in as element equivalent nodal load vector. Unlike linear static solution, system load vector is composed of only element loads since there is no nodal load definition for this type of problems.

In other words, the general process of the algorithm is similar with the one of linear static analysis except the assembly of the system matrices. Flow chart of linear steady-state heat transfer solution algorithm is displayed in Figure 3-4.

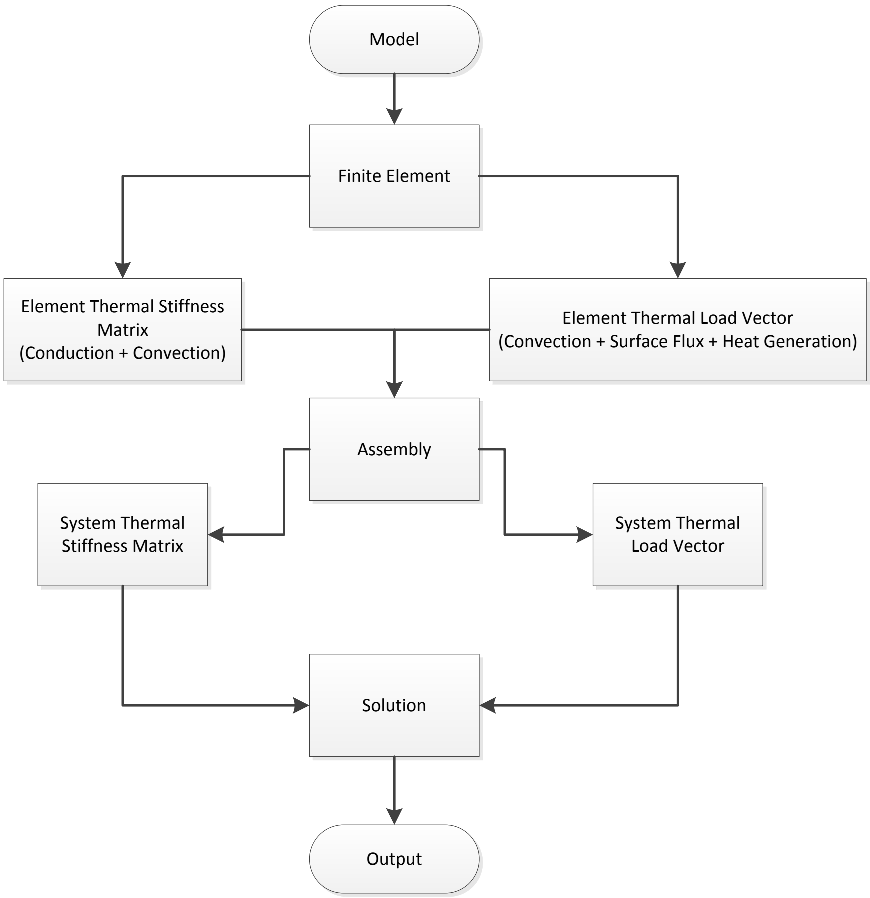

Figure 3-4 Flow Chart of Linear Steady-State Analysis Algorithm

As seen in Figure 3-4, general solution of the steady-state heat transfer algorithm is very similar to the one in linear static analysis algorithm. In fact, thermal stiffness matrix and nodal load vector of elements are obtained from finite element plug-ins and they are assembled into the system stiffness matrix and system load vector, respectively. These system matrix and system vector are then solved by using LU decomposition method and as a result, nodal temperatures and element fluxes are obtained. Nevertheless, the only difference from linear static analysis algorithm is the formation of system thermal stiffness matrix and thermal load vector. In linear static analysis algorithm, loadings whether element or nodal has contribution to the nodal load vector, only. Whereas nodal load vector includes only element loadings.

Linear Transient Analysis

The linear transient analysis is performed by utilizing two different time integration approaches; implicit and explicit Euler. As a first step, Taylor Series expansion of the general heat transfer equation (Equation 3-2) was calculated as shown in Equation 3-4.

$$f(x) = f(a) + f'(a)\,(x-a) + \frac{f''(a)}{2!}(x-a)^2 + \cdots = \sum_{i=1}^{n} \frac{f^{(i)}(a)}{i!}(x-a)^i \tag{3-4}$$

In Equation 3-4, ignoring the higher order terms yields to Equation 3-5.

$$f(x) = f(a) + f'(a)\,(x-a) \tag{3-5}$$

By adapting Equation 3-5 to the general equation of heat transfer, Equation 3-6 is obtained.

$$\{\theta\}_n = \{\theta\}_{n-1} + \{(1-\beta)\dot{\theta_{n-1}} + \beta(\dot{\theta_n})\}\Delta t \tag{3-6}$$

In Equation 3-6, θ, n, and Δt indicate nodal temperature vector, number of step, and time increment, respectively. Moreover, β is the coefficient used for selecting the solution method. In fact, the main point is to decide which slope, $\dot{\theta_{n-1}}$ or $\dot{\theta_n}$ is used. In here, different integration schemes having different slope definition such as forward, backward or central difference can be taken into account by changing β. In fact, for backward and forward Euler schemes, β is taken as 1 and 0, respectively. Backward integration scheme use the time derivation of temperatures at current time step. Since, the slope and temperatures at current time step (n) are not known, the method is called implicit. Whereas, forward integration scheme is called explicit since the slope in previous time step (n-1) is required. Therefore, only the temperature values of current time step is unknown. In addition to this, it is possible to use any other integration scheme by inserting appropriate coefficient, β.

Substituting Equation 3-6 into Equation 3-2 gives the following equation.

$$\theta_n = (C + \beta K \Delta t)^{-1}[\bar{F}\Delta t + C\theta_{n-1} + (\beta - 1)K\Delta t] \tag{3-7}$$

In Equation 3-7, $\bar{F}$ is total nodal force vector and calculated as stated in Equation 3-8.

$$\bar{F} = (1-\beta)F_{n-1} + \beta F_n \tag{3-8}$$

In linear transient heat transfer analysis algorithm, Equation 3-7 is solved. Flow chart of linear transient analysis algorithm is presented in Figure 3-5. In addition to thermal stiffness and thermal load vector, heat capacitance matrix, C is also calculated at the element level and assembled to the system matrices. These system matrices and temperature vector in previous time step (n-1) are solved by using implicit or explicit Euler integration scheme and temperature vector of the current time step (n) is obtained. Temperature vector of previous time step is updated and solution process repeats until the solution time is equal to end time. Nodal temperature vectors in any step are saved to the output file of the model.

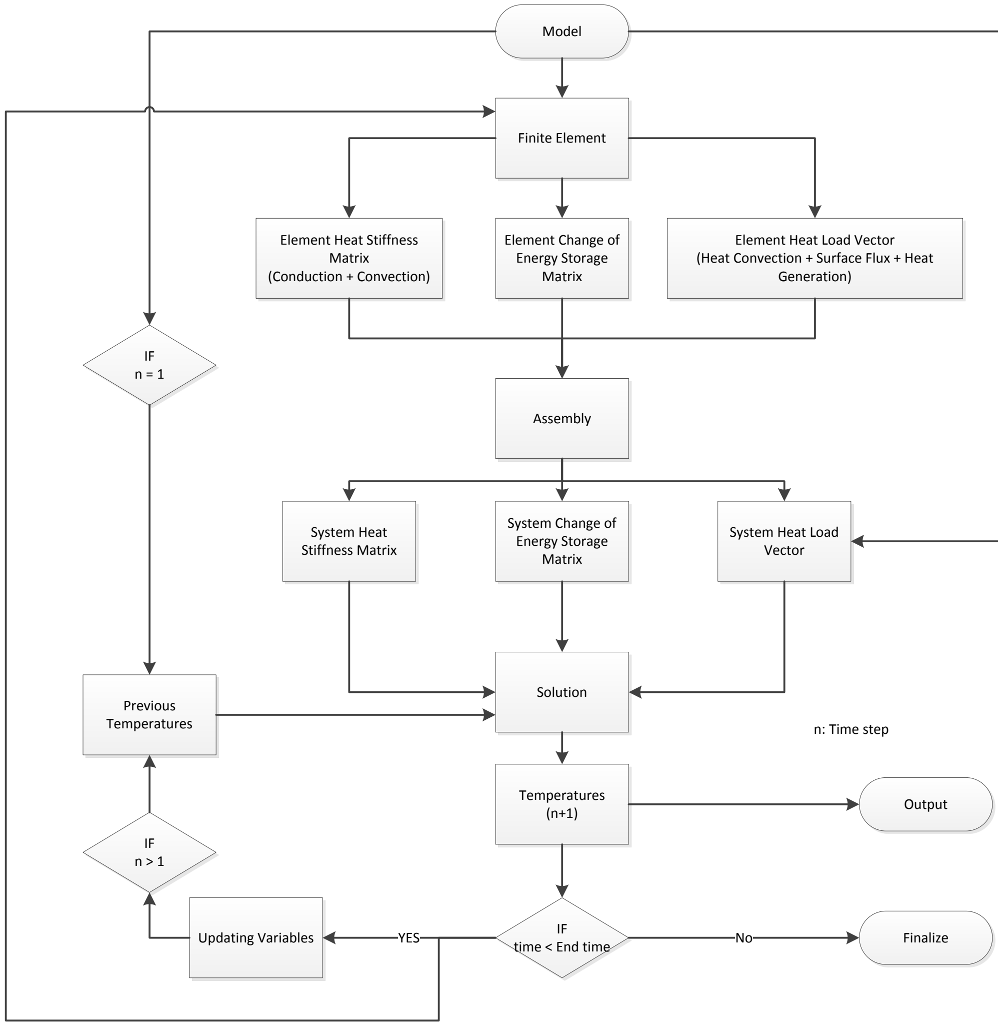

Figure 3-5 Flow Chart of Linear Transient Heat Transfer Analysis Algorithm

As stated above, implicit and explicit time integration schemes use the same equation (Equation 3-7) with different β coefficients. Taking β as zero (explicit scheme) and lumped heat capacitance matrix, C reduces the computational cost of inverse process. Whereas, even if lumped heat capacitance matrix, C is used, summation with thermal stiffness matrix damages the lumped property. This causes higher computational cost.

3.3.3. Coupled Analysis

The term coupled analysis refers to the combined analysis of multi-physics problems. The combination of different physics equations can be done by utilizing either strong or weak forms of the governing differential equations. Matrix form of weak form of coupled analysis is shown in Equation 3-9 (ANSYS, 2009).

$$\begin{bmatrix} K_{11} & 0 \\ 0 & K_{22} \end{bmatrix} \begin{Bmatrix} \theta \\ U \end{Bmatrix} = \begin{Bmatrix} F_T \\ F_u \end{Bmatrix} \tag{3-9}$$

In Equation 3-9, first and second row indicate heat transfer and structural analysis solution equations, respectively. Structural force vector, F_u includes both mechanical force and thermal force coming from heat transfer solution. Thus, it is required to solve heat transfer and structural analysis equations, sequentially.

In the weak form, first the analysis of a single physics problem, in this case heat transfer analysis, is performed and then the analysis of the second physics problem (linear static analysis) is conducted utilizing the output of the first analysis.

In this implementation, first of all, transient heat transfer analysis is performed and nodal temperature values for each time step are calculated. Then, subtracting output temperature values from initial ones, temperature change values are obtained for static analysis. Then, these values are inserted the linear static analysis algorithm; accordingly, nodal displacements and element stresses are obtained and saved to output file of the model. This procedure repeats until the solution time is equal to end time. Flow chart of coupled analysis implementation with transient solution is presented in Figure 3-6.

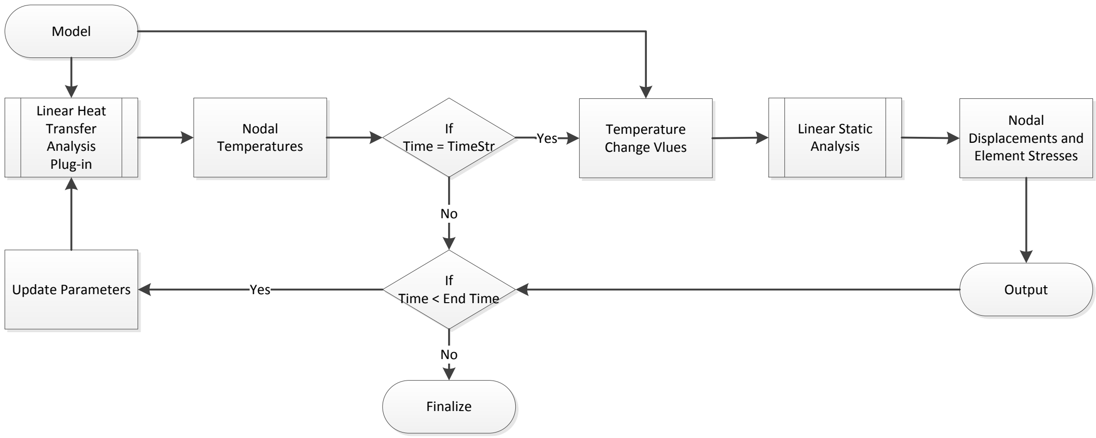

Figure 3-6 Flow Chart of Coupled Analysis Algorithms with Transient Solution in Weak Form

As heat transfer analysis, it is possible to use linear steady-state solution algorithm, also. Since this algorithm does not include iterative solution, implementation is quite simpler than the transient one. In fact, nodal temperatures and temperature change values are calculated once and then first solution process is finalized. The second process is same with the transient solution. This implementation process of steady-state solution is presented in Figure 3-7.

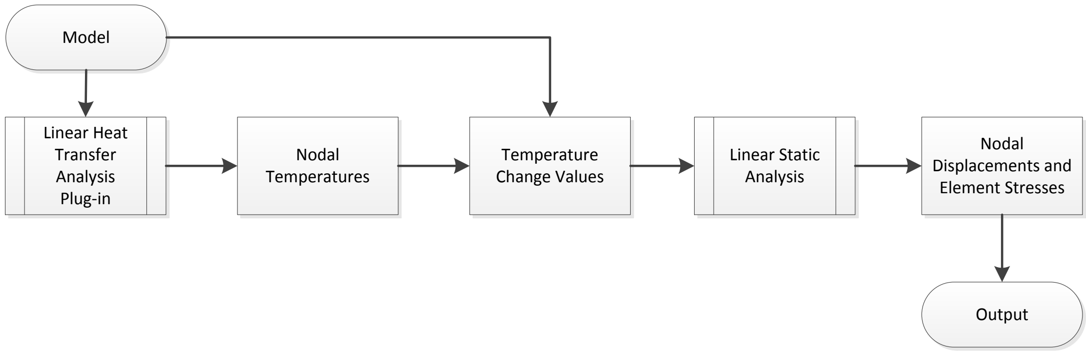

Figure 3-7 Flow Chart of Coupled Analysis Algorithm with Steady-State Solution in Weak Form

Linear static analysis algorithm sends nodal temperature change values to the finite element plug-in and equivalent nodal loads go back to the analysis plug-in. In fact, in finite element plug-ins, thermal strains due to nodal temperature change are calculated and these strains are converted to equivalent nodal force. These forces are sent back to the solution algorithm (linear static analysis algorithm) and assembled into the system nodal load vector. Flow chart of the process stated above is presented in Figure 3-8.

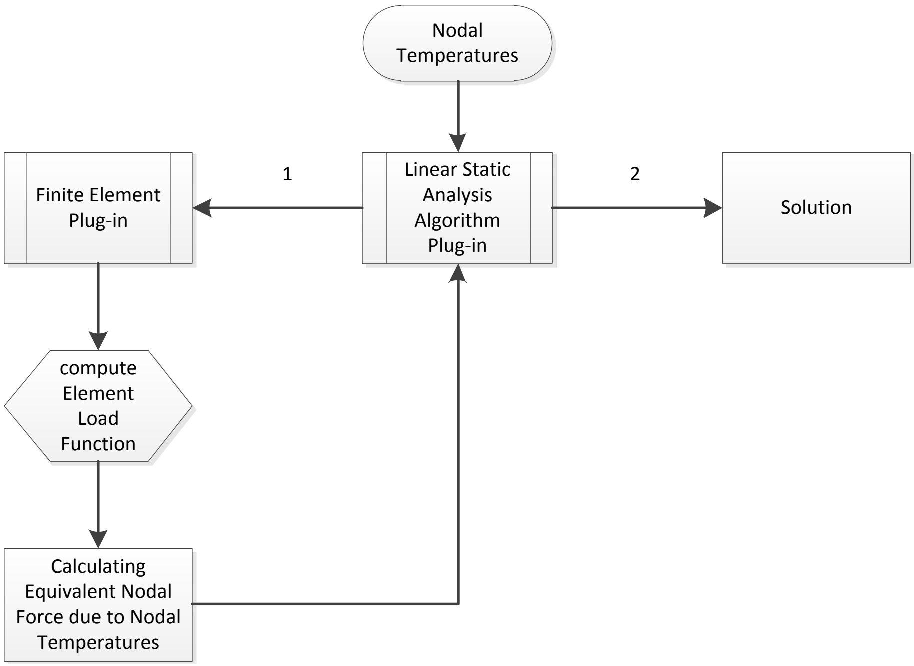

Figure 3-8 Flow Chart of Converting Nodal Temperatures to Equivalent Nodal Force

3.3.4. Parallel Solution Algorithms

Panthalassa has ability to execute parallel solution algorithms. Accordingly, parallel linear static and linear heat transfer analysis algorithms (steady-state and transient) were developed.

Linear static and linear steady-state analyses were parallelized by utilizing MUMPS (Multifrontal Massively Parallel Sparse Direct Solver) library (Amestoy et al., 2000). Indeed, in this study, solution of sparse matrix was performed by utilizing MUMPS. In these algorithms, sparse stiffness matrix is obtained at each core. MUMPS divides the sparse matrix and distributes each sub-matrix to all cores. Then the linear system is solved by MUMPS and the solution vector is sent to the main core. The flow chart of linear steady-state heat transfer analysis algorithm is presented in Figure 3-9. The procedure is the same for linear static analysis algorithm.

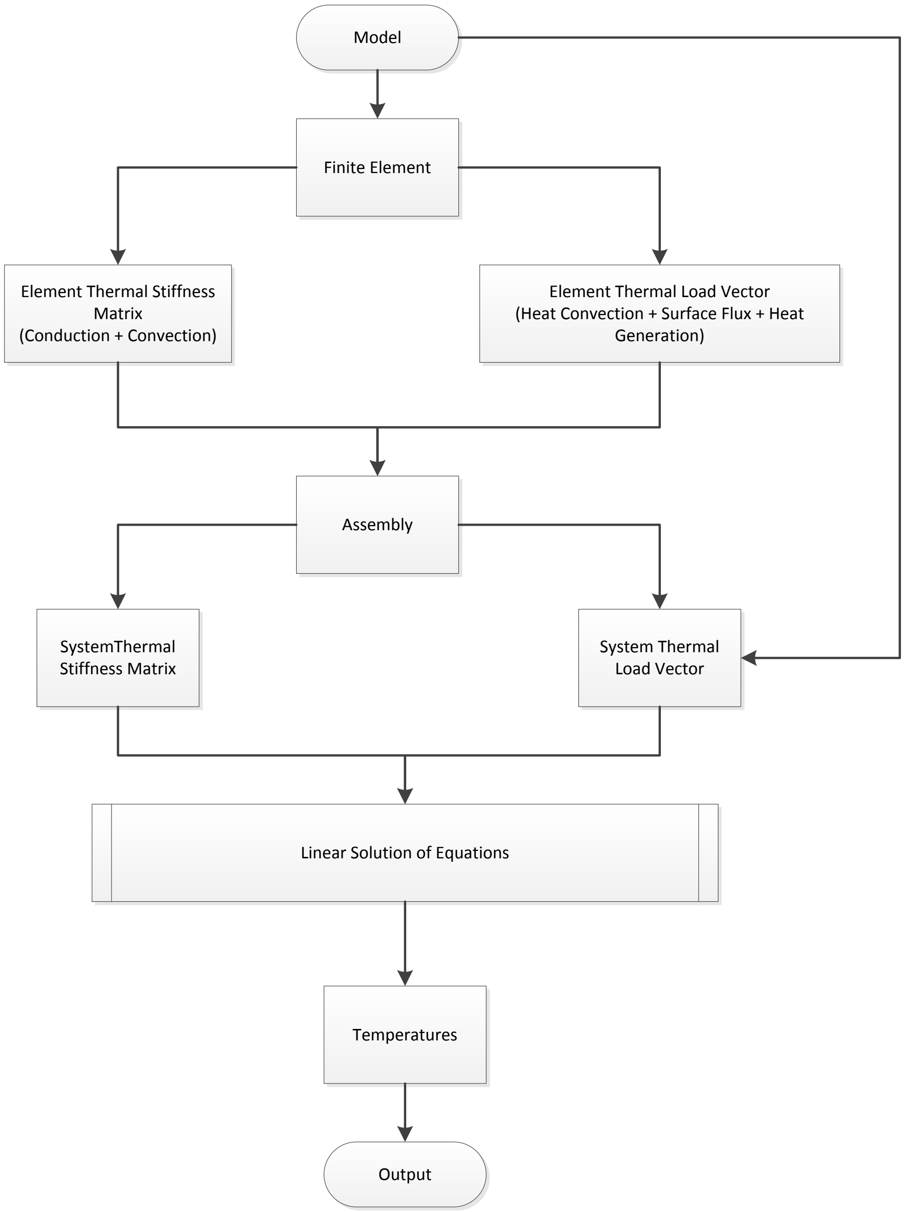

Figure 3-9 Flow Chart of Parallel Steady-State Heat Transfer Algorithm

For parallelization of linear transient heat transfer analysis algorithm, explicit Euler scheme was utilized assembly of the system equations and solution is performed at the element level. Accordingly, it is very suitable for parallelization. Indeed, in explicit scheme, heat capacitance matrix was taken as lumped; accordingly, taking inverse of lumped matrix does not cause significant computational cost. In this algorithm, thermal stiffness matrix is divided into sub-matrices and distributed to each core. Since each core knows the load vector and heat capacitance matrix, they solve the each substructure. Then they transfer the solution to each other; accordingly, each core has the total solution vector of the system. Each core updates the temperature values and repeats this procedure up to end time is reached. The flow chart of parallel transient heat transfer analysis algorithm is presented in Figure 3-10.

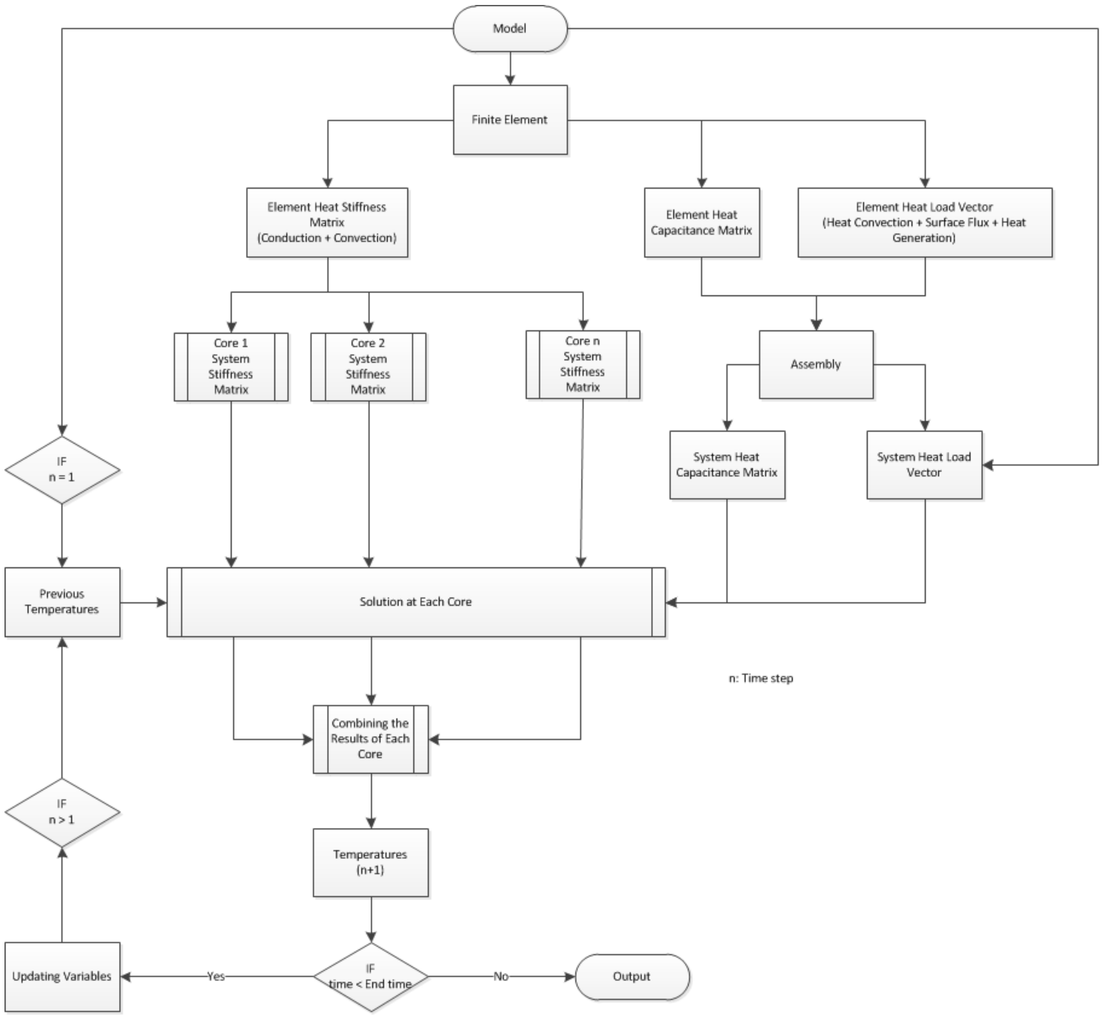

Figure 3-10 Flow Chart of Parallel Transient Heat Transfer Analysis Algorithm

3.4. Finite Elements

In this section, details of the two and three dimensional finite elements developed for this study are discussed. Linear and quadratic formulations of quadrilateral and triangular membrane elements were implemented as two dimensional elements. Similarly, linear and quadratic forms of hexahedral, wedge, and tetrahedral elements were implemented as three dimensional elements.

3.4.1. Geometrical Properties of Finite Elements

Description and general properties of 2D and 3D element are presented in Tables 3-1 and 3-2, respectively. In element geometry columns of the table, isoparametric and Cartesian geometry of the element are presented, respectively. Similarly, isoparametric boundary geometry of that element is listed in boundary geometry section. Moreover, shape functions of each finite element are presented in Table 3-3.

Table 3-1 Properties of 2D Finite Elements

Finite Element	Element Description	Number of Nodes	Degrees of Freedoms	Element Geometry	Boundary Geometry
Quad4	2D Linear Quadrilateral	4	Mechanical: Ux, Uy Heat Transfer: θ	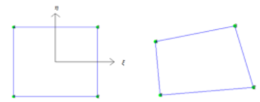	
Quad8	2D Quadratic Quadrilateral	8	Mechanical: Ux, Uy Heat Transfer: θ	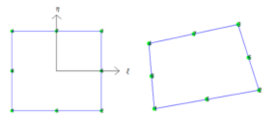	
TriM3	2D Linear Triangular Membrane	3	Mechanical: Ux, Uy Heat Transfer: θ	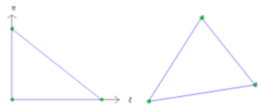	
TriM6	2D Quadratic Triangular Membrane	6	Mechanical: Ux, Uy Heat Transfer: θ	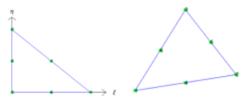	

Table 3-2 Properties of 3D Finite Elements

Finite Element	Element Description	Number of Nodes	Degrees of Freedoms	Element Geometry	Boundary Geometry
Brick8	3D Linear Hexahedral	8	Mechanical: Ux, Uy, Uz Heat Transfer: θ	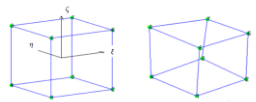	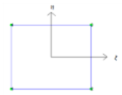
Brick20	3D Quadratic Hexahedral	20	Mechanical: Ux, Uy, Uz Heat Transfer: θ	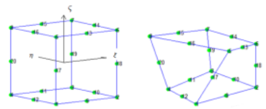	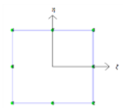
Wedge6	3D Linear Wedge	6	Mechanical: Ux, Uy, Uz Heat Transfer: θ	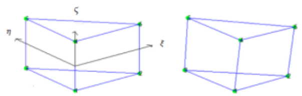	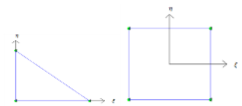
Wedge15	3D Quadratic Wedge	15	Mechanical: Ux, Uy, Uz Heat Transfer: θ	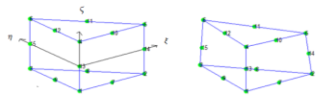	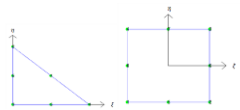
Tet4	3D Linear Tetrahedron	4	Mechanical: Ux, Uy, Uz Heat Transfer: θ	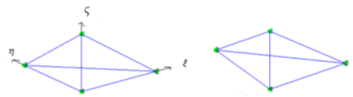	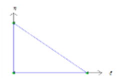
Tet10	3D Quadratic Tetrahedron	10	Mechanical: Ux, Uy, Uz Heat Transfer: θ	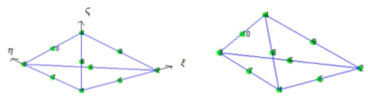	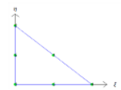

Table 3-3 Shape Functions for Finite Elements

Finite Element	Shape Functions	Limitations
Line2	$\frac{1-\xi}{2}, \frac{1+\xi}{2}$	-1 < ξ < 1
Line3	$\frac{\xi(\xi-1)}{2}, \frac{\xi(\xi+1)}{2}, 1-\xi^2$	-1 < ξ < 1
Quad4	$\frac{(1-\xi)\,(1-\eta)}{4}, \frac{(1+\xi)\,(1-\eta)}{4}, \frac{(1+\xi)\,(1+\eta)}{4}, \frac{(1-\xi)\,(1+\eta)}{4}$	-1 < ξ < 1 -1 < η < 1
Quad8	$\frac{(1-\xi)(1-\eta)-[(1-\xi)(1-\eta^2)+(1-\xi^2)(1-\eta)]}{4},$ $\frac{(1+\xi)(1-\eta)-[(1-\xi^2)(1-\eta)+(1+\xi)(1-\eta^2)]}{4}$ $\frac{(1+\xi)(1+\eta)-[(1+\xi)(1-\eta^2)+(1-\xi^2)(1+\eta)]}{4},$ $\frac{(1-\xi)(1+\eta)-[(1-\xi^2)(1+\eta)+(1-\xi)(1-\eta^2)]}{4},$ $\frac{(1-\xi^2)(1-\eta)}{4}, \frac{(1+\xi)(1-\eta^2)}{4}, \frac{(1-\xi^2)(1+\eta)}{4}, \frac{(1-\xi)(1-\eta^2)}{4}$	-1 < ξ < 1 -1 < η < 1
TriM3	$\xi, \eta, 1-\xi-\eta$	0 < ξ < 1 0 < η < 1
TriM6	$\xi(2\xi-1), \eta(2\eta-1), (1-\xi-\eta)(2(1-\xi-\eta)-1)$ $4\xi\eta, 4\eta(1-\xi-\eta), 4\xi(1-\xi-\eta)$	0 < ξ < 1 0 < η < 1
Brick8	$\frac{(1-\xi)\,(1-\eta)\,(1-\varsigma)}{8}, \frac{(1+\xi)\,(1-\eta)\,(1-\varsigma)}{8}, \frac{(1+\xi)\,(1+\eta)\,(1-\varsigma)}{8}, \frac{(1-\xi)\,(1+\eta)\,(1-\varsigma)}{8}$ $\frac{(1-\xi)\,(1-\eta)\,(1+\varsigma)}{8}, \frac{(1+\xi)\,(1-\eta)\,(1+\varsigma)}{8}, \frac{(1+\xi)\,(1+\eta)\,(1+\varsigma)}{8}, \frac{(1-\xi)\,(1+\eta)\,(1+\varsigma)}{8}$	-1 < ξ < 1 -1 < η < 1 -1 < ς < 1
Brick20	$\frac{(-1+\xi)\,(1-\eta)\,(1-\varsigma)\,(2+\xi+\eta+\varsigma)}{8}, \frac{(-1-\xi)\,(1-\eta)\,(1-\varsigma)\,(2-\xi+\eta+\varsigma)}{8}$ $\frac{(-1-\xi)\,(1+\eta)\,(1-\varsigma)\,(2-\xi-\eta+\varsigma)}{8}, \frac{(-1+\xi)\,(1+\eta)\,(1-\varsigma)\,(2+\xi-\eta+\varsigma)}{8}$ $\frac{(-1+\xi)\,(1-\eta)\,(1+\varsigma)\,(2+\xi+\eta-\varsigma)}{8}, \frac{(-1-\xi)\,(1-\eta)\,(1+\varsigma)\,(2-\xi+\eta-\varsigma)}{8}$ $\frac{(-1-\xi)\,(1+\eta)\,(1+\varsigma)\,(2-\xi-\eta-\varsigma)}{8}, \frac{(-1+\xi)\,(1+\eta)\,(1+\varsigma)\,(2+\xi-\eta-\varsigma)}{8}$ $\frac{2\,(1-\xi)\,(1+\xi)\,(1-\eta)\,(1-\varsigma)}{8}, \frac{2\,(1+\xi)\,(1-\eta)\,(1+\eta)\,(1-\varsigma)}{8}, \frac{2\,(1-\xi)\,(1+\xi)\,(1+\eta)\,(1-\varsigma)}{8}$ $\frac{2\,(1-\xi)\,(1-\eta)\,(1+\eta)\,(1-\varsigma)}{8}, \frac{2\,(1-\xi)\,(1+\xi)\,(1-\eta)\,(1+\varsigma)}{8}, \frac{2\,(1+\xi)\,(1-\eta)\,(1+\eta)\,(1+\varsigma)}{8}$ $\frac{2\,(1-\xi)\,(1+\xi)\,(1+\eta)\,(1+\varsigma)}{8}, \frac{2\,(1-\xi)\,(1-\eta)\,(1+\eta)\,(1+\varsigma)}{8}, \frac{2\,(1-\xi)\,(1-\eta)\,(1-\varsigma)\,(1+\varsigma)}{8}$ $\frac{2\,(1+\xi)\,(1-\eta)\,(1-\varsigma)\,(1+\varsigma)}{8}, \frac{2\,(1+\xi)\,(1+\eta)\,(1-\varsigma)\,(1+\varsigma)}{8}, \frac{2\,(1-\xi)\,(1+\eta)\,(1-\varsigma)\,(1+\varsigma)}{8}$	-1 < ξ < 1 -1 < η < 1 -1 < ς < 1

Table 3-3 (Continued)

Wedge6	$\frac{(1-\xi-\eta)(1-\varsigma)}{2}, \frac{\xi(1-\varsigma)}{2}, \frac{\eta(1-\varsigma)}{2}$ $\frac{(1-\xi-\eta)(1+\varsigma)}{2}, \frac{\xi(1+\varsigma)}{2}, \frac{\eta(1+\varsigma)}{2}$	$-1 < \xi < 1$ $-1 < \eta < 1$ $0 < \varsigma < 1$
Wedge15	$\frac{(-1+\xi+\eta)(1-\varsigma)(2\xi+2\eta+\varsigma)}{2}, \frac{\xi(1-\varsigma)(2\xi-\varsigma-2)}{2}$ $\frac{\eta(1-\varsigma)(2\eta-\varsigma-2)}{2}, \frac{(-1+\xi+\eta)(1+\varsigma)(2\xi+2\eta-\varsigma)}{2}$ $\frac{\xi(1+\varsigma)(2\xi+\varsigma-2)}{2}, \frac{\eta(1+\varsigma)(2\eta+\varsigma-2)}{2}$ $2\xi(1-\xi-\eta)(1-\varsigma), 2\xi\eta(1-\varsigma)$ $2\eta(1-\xi-\eta)(1-\varsigma), 2\xi(1-\xi-\eta)(1+\varsigma)$ $2\xi\eta(1+\varsigma), 2\eta(1-\xi-\eta)(1+\varsigma)$ $(1-\xi-\eta)(1-\varsigma^2), \xi(1-\varsigma^2), \eta(1-\varsigma^2)$	$-1 < \xi < 1$ $-1 < \eta < 1$ $0 < \varsigma < 1$
Tet4	$1-\xi-\eta-\varsigma, \xi, \eta, \varsigma$	$0 < \xi < 1$ $0 < \eta < 1$ $0 < \varsigma < 1$
Tet10	$(2(1-\xi-\eta-\varsigma)-1)(1-\xi-\eta-\varsigma), \xi(2\xi-1), \eta(2\eta-1)$ $\varsigma(2\varsigma-1), 4\xi(1-\xi-\eta-\varsigma), 4\xi\eta, 4\eta(1-\xi-\eta-\varsigma)$ $4\varsigma(1-\xi-\eta-\varsigma), 4\xi\varsigma, 4\eta\varsigma$	$0 < \xi < 1$ $0 < \eta < 1$ $0 < \varsigma < 1$

As seen in Table 3-1, Quad4 and Quad8, TriM3 and TriM6 are linear and quadratic form of 2D quadrilateral and triangular elements, respectively. These 2D elements have only in-plane (membrane) behavior. Triangular elements are better suited for modeling the irregularly shaped domains.

In addition to 2D elements, Brick8 and Brick20, Wedge6 and Wedge15, and Tet4 and Tet10 are linear and quadratic forms of hexahedral, wedge, and tetrahedral elements, respectively (Table 3-2). They can be used for modeling 3D solids.

Each element shown in Tables 3-1 and 3-2 has both mechanical and heat transfer degrees of freedom. 2D and 3D elements have two and three mechanical degrees of freedom for each node, respectively. For the heat transfer analysis part, whereas each element has only one degree of freedom.

Each element can calculate linear stiffness matrix, internal force and element stress vectors. In fact, element stresses are calculated at nodal points. Moreover, they can convert element loads such as body loads, surface loads, temperature change loads, and initial strains to equivalent nodal load vector. For computing equivalent nodal loads due to temperature change, two different methods were developed for each element. First method assumes constant temperature difference throughout the element and computes the nodal loads accordingly. During the coupled analysis, however, nodal temperatures are obtained at the end of heat transfer analysis. In other words, each element can have different temperature values at its nodal points. Because of this, second method was developed to compute nodal loads from different nodal temperatures. In fact, nodal temperature strains and corresponding stress values are calculated from nodal temperature values (Equations 3-10 and 3-11). Then, these nodal stress values contribute to calculation of equivalent nodal load with the rate of weight value of the corresponding integration points (Equation 3-12).

$$\varepsilon_i = [\Delta t_i * a \quad \Delta t_i * a \quad \Delta t_i * a \quad 0 \quad 0 \quad 0]^T \tag{3-10}$$

$$\sigma_i = C\, \varepsilon_i \tag{3-11}$$

$$F_{equivalent} = \sum_{i=1}^{n} B_i^T \sigma_i |J_i| w_i \tag{3-12}$$

In Equations 3-10 to 3-12, ε_i, Δt_i, σ_i, B_i, J_i, and w indicate strain, temperature change, stress, strain field, and Jacobian of i^th node, respectively. Similarly, thermal expansion coefficient, constitutive material matrix and number of node are represented by letters a, C, and n, respectively.

Each element can also calculate heat conduction and heat convection stiffness matrices and heat generation, heat convection, and surface flux load vectors. Heat generation is a kind of body loading; heat convection and surface flux loading conditions are surface loadings. Heat convection stiffness matrix is obtained from heat convection loading condition as stated in Solution Algorithm part.

In Table 3-3, shape functions for each geometry used for body and surface definition of finite elements are listed. As seen in Tables 3-1 and 3-2, volume elements have either triangular or quadrilateral faces and surface elements have linear edges. 2D surface elements can have linear or quadratic edges depending on the element's number of nodes. Likewise, linear and quadratic 3D solid elements have linear and quadratic quadrilateral/triangular faces. Whenever an edge loading in 2D elements and surface loading in 3D elements are converted into nodal values, the corresponding edge or face elements' shape functions are utilized. Thus, mechanical stiffness, element stresses, internal forces heat conduction, heat convection, heat generation, heat capacitance are obtained from body integration. On the other hand, by taking boundary integrals, mechanical surface loads such as distributed load over surface of a body, and surface loads of heat transfer problems such as surface flux and heat convection are converted to equivalent nodal load vector.

3.4.2. Numerical Integration

Body and boundary integrals are evaluated numerically by using Gauss Quadrature method. According to Gauss Quadrature method, function is evaluated at certain integration points and multiplied with the corresponding weight value. Then, by summing the results obtained from each integration point, integral over the domain is obtained. The general equation for Gauss Quadrature Rule is presented in Equation 3-13.

$$I = \int_{\Omega} f\, d\Omega = \int_{V} G\, dV = \sum_{i=1}^{n} Wi\, Gi \tag{3-13}$$

In Equation 3-13, n, W, and G represent number of integration points, weight of integration points, function defined in the mapped domain. Since the numerical integrations are valid for corresponding domains, it is required to map the function, f to the integration domain.

For each finite element, the choice of the location and number of integration points significantly affect the behavior and accuracy of the results. Due to problematic element behavior mechanisms such as shear locking or hourglassing, and accuracy condition of Gauss Quadrature rule, appropriate number of integration points with the domain should be chosen.

Quadrilateral membrane elements are integrated numerically by applying Multidimensional Gauss Quadrature method, called Gaussian product rule (Cook et al. 1989). For linear quadrilateral element, deciding the number of integration points for computation is a problematic issue. 2x2 full integration causes shear locking; whereas, single point integration results in zero energy modes (hourglassing). In this study, for linear elements, full integration scheme was selected (four integration points) for integration of both structural analysis and heat transfer part. On the other hand, for structural calculations of quadratic elements, nine integration points (full integration) were used. This way, the zero energy modes in quadratic elements were eliminated. Four integration points are however sufficient for heat transfer calculations. In order to improve the conditions of heat capacitance matrix, full integration was applied for both linear and quadratic elements. Properties of integration point schemes of quadrilateral are listed in Table A-2.

For linear and quadratic triangular elements, reduced integration (one and three integration points, respectively) was utilized. Such integration approach for stiffness calculation does not cause any zero energy (hourglassing) modes in triangular elements. Moreover, since the element has constant stress ditribution, shear locking phenomena occurs for linear triangular element. Using reduced integration for calculation of heat capacitance matrix, [C] however causes instability. Accordingly, six integration points were utilized for [C] matrix for each type of triangular element. Details of integration point schemes of linear and quadratic triangular elements are presented in Table A-3.

Full integration scheme (eight integration points) hindering zero energy modes were utilized for both structural and heat transfer matrices of hexahedral elements. However, twenty-seven integration points were preferred to improve conditions of heat capacitance matrix [C]. For quadratic element, all numerical integrations were calculated with twenty-seven points (full integration). Properties of integration point schemes for hexahedrons are listed in Table A-4.

Wedge elements are special 3D solid elements that have both triangular and rectangular faces. Because of this reason, distribution of integration points is quite different than other elements. For the triangular top and bottom faces integration points defined for triangular elements were used. On the other hand, along the depth of the element, integration points were distributed similar to quadrilateral elements. Two and nine integration points are utilized for the linear and quadratic wedge elements, respectively. Such number of integration points hinders zero energy mode. In order to improve conditions of heat capacitance matrix [C], eight-teen integration points advised by Dhondt (2004) are preferred. Details of integration point scheme of Wedge elements are listed in Table A-5.

For linear and quadratic tetrahedral elements, one and four integration points are utilized, respectively. They are the minimum number of integration points that do not create any hourglassing mode. Similar to the other solid elements, fifteen integration points suggested by Dhondt (2004) are utilized in order to improve the condition of heat capacitance matrix, [C]. Properties of integration points of tetrahedrons are illustrated in Table A-6.

The behavior of the boundaries of linear and quadratic forms of 2D quadrilateral and triangular elements are described by the linear and quadratic form of line elements, respectively. For taking line integrals, Gauss Quadrature method is used. In order to represent actual behavior of boundaries better, two and three integration points (full integration) are preferred for linear and quadratic line elements, respectively. For calculating the surface loads of heat transfer analysis, using more integration points provides higher accuracy. Details of integration point schemes of line element are shown in Table A-1.

In a similar manner, linear and quadratic forms of Quad and TriM elements were used to describe the behavior of the faces of 3D elements. Therefore, same integration schemes for Quad and Trim elements stated above were taken into account for integration of boundaries of 3D elements. In other words, four and nine integration points are utilized for linear and quadratic quadrilateral elements, respectively. Similarly, one and three integration points are sufficient for linear and quadratic triangular faces, respectively. Properties of the integration point scheme of a rectangle and a triangle are tabulated in Table A-2 and Table A-3, respectively.

CHAPTER 4

VERIFICATION PROBLEMS

4.1. Introduction

In this chapter, verifications of solution algorithms and finite elements stated in previous chapters are discussed. Two different types of engineering problems, linear structural analysis and linear heat transfer being part of coupled analysis system were solved.

Several structural analysis problems, proposed by MacNeal and Harder (1985) for finite element formulation verification were solved by using all the implemented elements. The test problems can be considered in two parts, problems with static loads and with temperature loads. This way the element performances under direct and indirect loading were examined.

Likewise, in order to verify the implemented heat transfer solution algorithms and finite elements for heat transfer, two different plate problems suggested by Reddy and Gartling (2010), square and rectangular plates were analyzed. While square plate problem only focuses on heat conduction and heat generation routines, the rectangular plate problem needs all routines heat conduction, heat convection, heat generation, surface flux of heat transfer part of finite elements.

4.2. Structural Analysis Verification

4.2.1. Linear Static Problems

This part includes the structural performance of elements, existing finite element library and linear solution algorithms under static loads. In order to verify finite elements for structural problems and corresponding solution algorithms, first straight cantilever beam problem recommended by MacNeal and Harder (1985) was solved. This beam problem was analyzed by using both two and three dimensional finite elements.

2D Straight Beam with Static Loads

Straight cantilever beams modeled with 2D quadrilateral and triangular elements suggested by MacNeal and Harder (1985) are presented in Figure 4-1 and Figure 4-2, respectively and the geometrical and material properties are tabulated in Table 4-1.

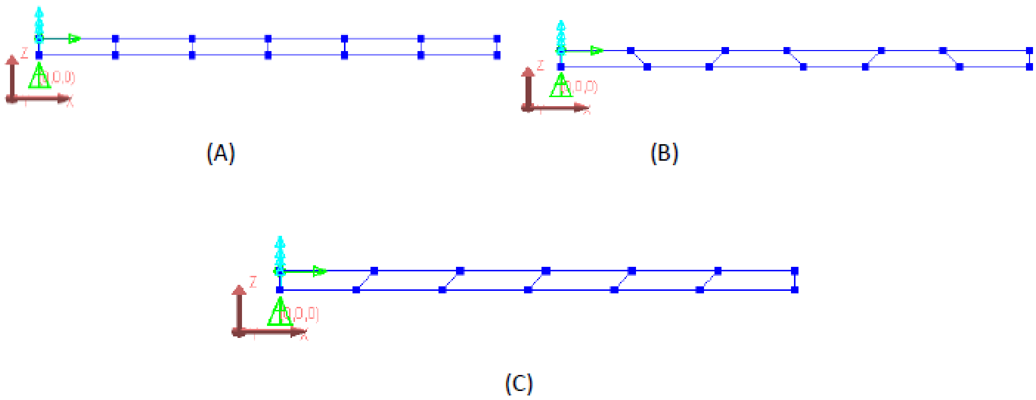

Figure 4-1 Straight Beams with Quadrilateral Elements. (A) Rectangular Meshed Beam. (B) Trapezoidal Meshed Beam.

(C) Parallelogram Meshed Beam

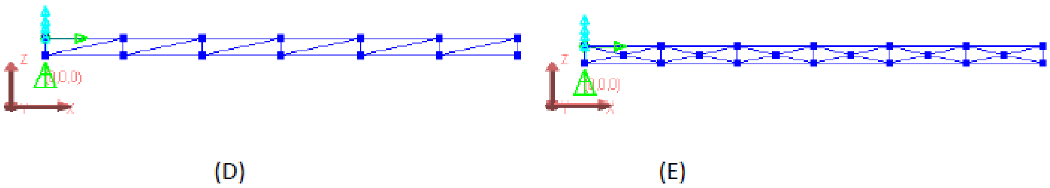

Figure 4-2 Straight Beams with Triangular Elements. (D) With 12 Triangular Elements. (E) With 24 Triangular Elements

Table 4-1 Straight Beam with Static Loads – Model Properties

Geometric Properties		Material Properties		Section Properties	
Length:	6 in	Modulus of Elasticity:	1,000,000 lb / in^2	Depth:	0.1 in
Height:	0.2 in	Poisson's Ratio:	0.3		
		Shear Modulus:	3,846,154 lb / in^2		

To display the performances of the finite elements under different loading conditions, the load cases listed in Table 4-2 were applied to the beam. Since 2D elements in the finite element library include only in-plane (membrane) action, out of plane loading cases were eliminated for analyses of these elements.

The beam was analyzed under different behavior modes and the accuracy of each element was investigated. The applied loadings and corresponding behavior modes are presented in Table 4-2. Currently, only membrane (in-plane) action was considered. Two types of quadrilateral and two types of triangular elements were examined.

Table 4-2 Straight Beam with Static Loads – Load Cases

Loading	Behavior Mode	Load
1	Axial Extension	F_x = 0.5 lb at each joints at the free end
2	Shear and Bending	F_z = 0.5 lb at each joints at the free end
3	Pure Bending	F_x = -5 lb at bottom joint of free end F_x = 5 lb at top joint of free end

Displacements at the free end and stresses at the fixed-end of the beam modeled with linear and quadratic quadrilateral elements (Quad4 and Quad8) and linear and quadratic triangular elements (TriM3 and TriM6) are compared with the analytical results. The results cover the beams modeled with distorted or uniform elements (Figure 4-1, model A,B,C) for every quadrilateral elements. Tables 4-3 and 4-5 present the displacement values for both quadrilateral and triangular elements, respectively. Whereas the stress results are shown in Tables 4-4 and 4-6.

Table 4-3 Straight Beam with Quad Elements (Quad4 & Quad8) – Displacements at the Free-End

Loading Condition	Model	Output Parameter	Quad4 (in)	Quad8 (in)	Analytical (in)
Axial Extension	A	u_x	$3.00*10^{-5}$	$3.02*10^{-5}$	$3.00*10^{-5}$
	B		$3.00*10^{-5}$	$3.02*10^{-5}$	
	C		$3.00*10^{-5}$	$3.02*10^{-5}$	
Shear and Bending	A	u_z	$1.01*10^{-2}$	$1.07*10^{-1}$	$1.08*10^{-2}$
	B		$2.90*10^{-3}$	$1.06*10^{-1}$	
	C		$3.60*10^{-3}$	$8.06*10^{-2}$	
Pure Bending	A	u_x	$8.40*10^{-5}$	$9.00*10^{-4}$	$9.00*10^{-4}$
	B		$2.06*10^{-5}$	$8.93*10^{-4}$	
	C		$2.82*10^{-5}$	$6.22*10^{-4}$	

According to the values stated in Table 4-3, linear quadrilateral element has slightly better performance than the quadratic one under axial loading cases. Since the axial deformation behavior is linear (Equation 4-1), shape functions of linear element coincides better with real behavior. On the other hand, for shear and bending and pure bending cases, results of quadratic element are closer to the analytical results than the ones of linear element. In fact, deformed shape under shear and bending and moment load cases has higher order function (Equation 4-2). Because of this reason, quadratic shape functions represent the deformed shape better than the linear ones.

$$\delta = \int \frac{P}{AE} dx \qquad (4\text{-}1)$$

$$\delta = \int \frac{P}{EI} x^2 dx \qquad (4\text{-}2)$$

In general, using elements with distorted shapes reduces the accuracy of the results. In order to show the performances of 2D linear and quadratic quadrilateral elements with distortions, same cantilever beam was modeled by using trapezoidal and parallelogram shaped elements (Figure 4-1 (B) and (C)). When the corner angles diverge from 90^{o}, the accuracy of the mapping with Jacobian matrix diminishes (Cook et al, 1989). According to the results stated in Table 4-3, for cases B and C under axial loading, models with trapezoidal and parallelogram elements display same accuracy with the analytical results for the linear element. The reason is again the function of axially deformed shape of beam is same order with the shape functions of linear element. Nevertheless, similar to models without any distortion, quadratic element is able to mimic the deformation function under shear-bending and pure bending cases even if it is distorted. The elements with parallelogram perform better than the trapezoidal one.

Table 4-4 Straight Beam with Quad Elements (Quad4 & Quad8) – Stresses at the Fixed-End

Behavior Mode	Model	Output Parameter	Quad4 (lb/in^2)	Quad8 (lb/in^2)	Analytical (lb/in^2)
Axial Extension	A	σ_x	$5.00*10^1$	$5.38*10^1$	$5.00*10^1$
	B		$5.00*10^1$	$4.99*10^1$	
	C		$5.00*10^1$	$5.02*10^1$	
Shear and Bending	A	σ_x	$8.46*10^2$	$9.00*10^3$	$9.00*10^3$
	B		$2.19*10^2$	$8.44*10^3$	
	C		$6.35*10^2$	$9.48*10^3$	
Pure Bending	A	σ_x	$1.54*10^2$	$1.50*10^3$	$1.50*10^3$
	B		$3.59*10^1$	$1.38*10^3$	
	C		$1.23*10^2$	$1.60*10^3$	

Stresses depend on strains which are the first derivatives of the displacements. Thus, the error in stresses is usually much larger than the error in displacements since they depend on the rate of change in displacements. According to the results presented in Table 4-4, the stress outputs of the quadratic element are much better than the linear ones. When compared with the analytical results, the error in the stress values of linear elements is unacceptable for both bending problems.

Table 4-5 Straight Beam with Triangular Elements (TriM3 & TriM6) – Displacements at the Free-End

Behavior Mode	Model	Output Parameter	TriM3 (in)	TriM6 (in)	Analytical (in)
Axial Extension	D	u_x	$3.00*10^{-5}$	$3.03*10^{-5}$	$3.00*10^{-5}$
	E		$3.00*10^{-5}$	$3.03*10^{-5}$	
Shear and Bending	D	u_z	$2.48*10^{-2}$	$1.07*10^{-1}$	$1.08*10^{-1}$
	E		$4.98*10^{-2}$	$1.08*10^{-1}$	
Pure Bending	D	u_x	$2.08*10^{-4}$	$9.00*10^{-4}$	$9.00*10^{-4}$
	E		$4.17*10^{-4}$	$9.00*10^{-4}$	

In Table 4-5, end displacements of the cantilever beam displayed in Figure 4-2 (D, E) under each loading conditions stated in Table 4-2 are tabulated and compared with analytical results. Similar to rectangular membrane elements, under axial loading case, performances of linear triangular element are slightly better than the quadratic one; on the other hand, under shear-bending and pure bending load cases, quadratic triangular membrane element has higher accuracy.

In fact, since axial deformation function is linear, increasing mesh does not provide higher accuracy for both linear and quadratic elements. Whereas under shear-bending and pure bending conditions, since the displacement function of the beam is a third order polynomial, quadratic element fits better than the linear one. Hence, increasing mesh density does not affect the accuracy of the problem for quadratic element. On the other hand, in order to obtain higher accuracy, mesh should be increased for linear elements. In other words, it is possible to get the performance same as with the one of quadratic element by using very fine meshed linear elements.

When performances of quadrilateral and triangular elements are compared, it can be seen that in general, quadrilateral elements have better performance. In fact, due to the fact that triangular elements have high stiffness values at mutual nodes, they behave stiffer than quadrilateral elements.

Table 4-6 Straight Beam with Triangular Elements (TriM3 & TriM6) – Stresses at the Fixed-End

Behavior Mode	Model	Output Parameter	TriM3 (lb/in^2)	TriM6 (lb/in^2)	Analytical (lb/in^2)
Axial Extension	D	σ_x	$5.00*10^{1}$	$5.30*10^{1}$	$5.00*10^{1}$
	E		$5.00*10^{1}$	$5.00*10^{1}$	
Shear and Bending	D	σ_x	$2.57*10^{2}$	$8.36*10^{3}$	$9.00*10^{3}$
	E		$4.76*10^{2}$	$8.41*10^{3}$	
Pure Bending	D	σ_x	$4.72*10^{1}$	$1.50*10^{3}$	$1.50*10^{3}$
	E		$8.65*10^{1}$	$1.50*10^{3}$	

In Table 4-6, normal stresses along x direction at fixed-end of the beam are tabulated. According to the results of Table 4-6, similar to the displacement behavior of linear elements, using more elements fits better to the actual behavior under shear-bending and pure bending cases. On the other hand, although increasing mesh does not affect the displacement performance of quadratic element, it provides better accuracy for stresses since the error in stress calculation is larger than the one in displacement.

3D Straight Beam with Static Loads

Same cantilever beam stated in previous part of this chapter was modeled with each three dimensional element in finite element library (Figure 4-3 and Figure 4-4). Properties of the beams are presented in Table 4-7.

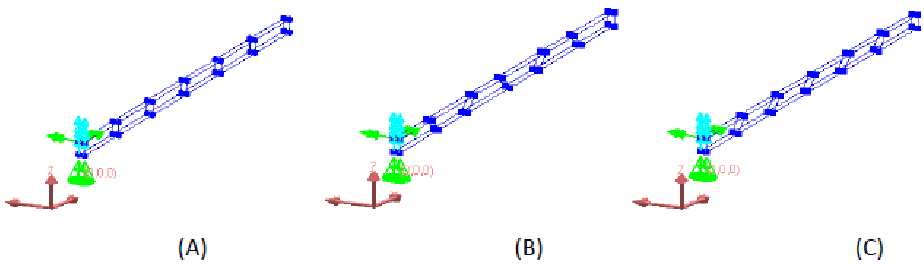

Figure 4-3 Straight Beams with Hexahedral Elements. (A) Rectangular Prismatic Element. (B) Trapezoidal Prismatic Element. (C) Parallelogram Prismatic Element

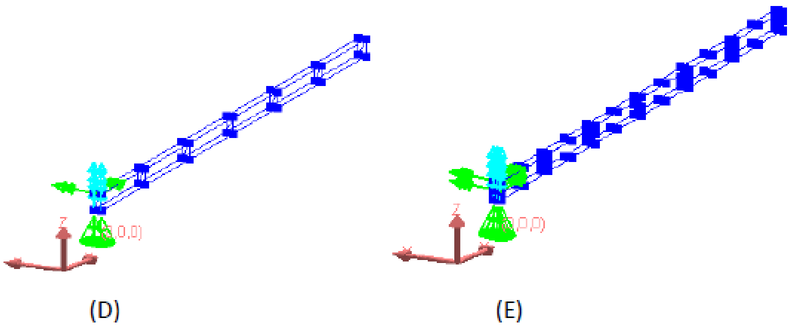

Figure 4-4 Straight Beams with Wedge Elements. (D) Beam with Linear Wedge Elements. (E) Beam with Quadratic Wedge Elements

Table 4-7 Straight Beam with Static Loads – Model Properties

Geometric Properties		Material Properties	
Length:	6 in	Modulus of Elasticity:	1,000,000 lb / in^2
Height:	0.2 in	Poisson's Ratio:	0.3
Width:	0.1 in	Shear Modulus:	3,846,154 lb / in^2

The cantilever beam was analyzed under different behavior modes and the accuracy of each 3D finite element was investigated. The applied loadings and the corresponding behavior modes are presented in Table 4-8.

Table 4-8 Straight Beam with Static Loads – Load Cases

Loading	Behavior Mode	Load
1	Axial Extension	F_x=0.25 lb at each joints at the free end
2	Shear and Bending in Strong Axis	F_z=0.25 lb at each joints at the free end
3	Shear and Bending in Weak Axis	F_y=0.25 lb at each joints at the free end
4	Twisting	F_y=-2.5 lb at bottom joints of free end F_y=2.5 lb at top joints of free end
5	Pure Bending in Strong Axis	F_x=-2.5 lb at bottom joints of free end F_x=2.5 lb at top joints of free end
6	Pure Bending in Weak Axis	F_x=5 lb at joints of free end exist on plane y=0 F_x=-5 lb at joints of free end exist on plane y=0.1

Displacement results of the cantilever beam at the free-end modeled by using linear and quadratic hexahedral (Brick8 & Brick20), linear wedge (Wedge6), quadratic wedge (Wedge15), linear tetrahedral (Tet4), and quadratic tetrahedral (Tet10) elements are presented in Table 4-9, Table 4-11, Table 4-13, Table 4-15, and Table 4-17, respectively. Similarly, stresses at the fixed end of the beam are shown in Table 4-10, 4-12, 4-14, 4-16, and 4-18 for hexahedral, wedge, and tetrahedral elements, respectively.

Table 4-9 Straight Beam with Hexahedral Elements (Brick8 & Brick20) – Displacements at the Free-End

Behavior Mode	Model	Mesh	Output Parameter	Brick8 (in)	Brick20 (in)	Analytical (in)
Axial Extension	A	6x1x1	u_x	$2.99*10^{-5}$	$3.01*10^{-5}$	$3.00*10^{-5}$
		30x1x1		$3.00*10^{-5}$	-	
		30x4x8		$3.71*10^{-5}$	-	
	B	6x1x1		$2.99*10^{-5}$	$3.01*10^{-5}$	
	C	6x1x1		$2.99*10^{-5}$	-	
Shear and Bending in Strong Axis	A	6x1x1	u_z	$1.00*10^{-2}$	$1.07*10^{-1}$	$1.08*10^{-1}$
		30x1x1		$7.18*10^{-2}$	-	
		30x4x8		$1.07*10^{-1}$	-	
	B	6x1x1		$2.84*10^{-3}$	$9.72*10^{-2}$	
	C	6x1x1		$3.46*10^{-3}$	-	

Table 4-9 (Continued)

Shear and Bending in Weak Axis		6x1x1		$1.09*10^{-2}$	$4.16*10^{-1}$	
	A	30x1x1		$1.56*10^{-1}$	-	
		30x4x8	u_y	$4.17*10^{-1}$	-	$4.32*10^{-1}$
	B	6x1x1		$4.65*10^{-3}$	$3.98*10^{-1}$	
	C	6x1x1		$6.23*10^{-3}$	-	
Twisting		6x1x1		$2.86*10^{-3}$	$2.90*10^{-3}$	
	A	30x1x1		$2.92*10^{-3}$	-	
		30x4x8	u_y	$3.39*10^{-3}$	-	$3.41*10^{-3}$
	B	6x1x1		$1.62*10^{-3}$	$3.09*10^{-3}$	
	C	6x1x1		$1.10*10^{-3}$	-	
Pure Bending in Strong Axis		6x1x1		$8.38*10^{-5}$	$9.00*10^{-4}$	
	A	30x1x1		$5.99*10^{-4}$	-	
		30x4x8	u_x	$9.55*10^{-4}$	-	$9.00*10^{-4}$
	B	6x1x1		$1.94*10^{-5}$	$8.30*10^{-4}$	
	C	6x1x1		$2.56*10^{-5}$	-	
Pure Bending in Weak Axis		6x1x1		$4.53*10^{-5}$	$1.80*10^{-3}$	
	A	30x1x1		$6.50*10^{-4}$	-	
		30x4x8	u_x	$1.87*10^{-3}$	-	$1.80*10^{-3}$
	B	6x1x1		$1.72*10^{-5}$	$1.66*10^{-3}$	
	C	6x1x1		$2.51*10^{-5}$	-	

In Table 4-9, end displacements of the cantilever beam created with hexahedral elements under each loading condition are listed and they are compared with the analytical results. According to results stated in Table 4-9, displacements under axial loading condition are close to analytical results. For the other cases, however, difference between results of linear element (Brick8) and analytical ones are much larger. Moreover, distorting the geometry of the elements affects the performances of each loading condition negatively as also observed for 2D membrane elements.

When behaviors of quadrilateral and hexahedral elements are compared, it can be seen that hexahedral elements behave more stiff under axial and moment load cases. This situation occurs because of the handling the Poisson's effect. Due to having stiffness along thickness, hexahedral element behaves stiffer. If Poisson's effect is neglected, the behaviors of these two types of elements become same.

Another important result observed from the results in Table 4-9 is increasing mesh size of the beam model provides more realistic behavior. In fact, since deformed shape of the beam with linear elements is a piecewise linear function, it is possible to get function closer to the actual one by dividing the structure into smaller elements. Because of this, displacements of the beam modeled with fine mesh model are close to the analytical one. However, axial deformation of beam with 30x4x8 meshed elements is greater than the analytical result. The reason is that dividing the cross section into parts causes another mechanism which is ignored during the analytical solution. This mechanism is the deformation of the cross section. In fact, the beam was solved in analytically according to “plane section remains plane” assumption. Nevertheless, meshing the cross section and not using uniformly distributed load over the cross section results in deformation of the section. Because of this, axial deformation exceeds the analytical value.

Table 4-10 Straight Beam with Hexahedral Elements – Stresses at the Fixed-End

Behavior Mode	Model	Output Parameter	Brick8 (lb/in^2)	Brick20 (lb/in^2)	Analytical (lb/in^2)
Axial Extension	A	σ_x	5.30*10^1	5.30*10^1	5.00*10^1
	B		5.30*10^1	5.20*10^1	
	C		5.30*10^1	-	
Shear and Bending in Strong Axis	A	σ_x	1.02*10^3	9.44*10^3	9.00*10^3
	B		2.32*10^2	8.87*10^3	
	C		8.33*10^2	-	
Shear and Bending in Weak Axis	A	σ_x	5.40*10^2	1.87*10^4	1.80*10^4
	B		2.06*10^2	1.83*10^4	
	C		4.97*10^2	-	
Twisting	A	σ_x	2.54*10^2	5.76*10^2	2.45*10^3
	B		1.64*10^2	6.77*10^2	
	C		1.27*10^2	-	
Pure Bending in Strong Axis	A	σ_x	1.87*10^2	1.67*10^3	1.50*10^3
	B		30.8*10^1	1.61*10^3	
	C		1.54*10^2	-	
Pure Bending in Weak Axis	A	σ_x	3.73*10^2	3.33*10^3	3.00*10^3
	B		3.10*10^1	3.23*10^3	
	C		9.10*10^1	-	

In Table 4-10, fixed end stresses of the structure are shown. Since nodal displacements contribute to the calculation of element stresses, stress values of quadratic element represent the analytical solutions better. Since quadratic element was developed with full integration, higher stress values compared to analytical ones were obtained. In addition, distortion causes reduction in accuracy of element stresses for both linear and quadratic elements as expected.

Table 4-11 Straight Beam with Linear Wedge Elements (Wedge6) – Displacements at the Free-End

Behavior Mode	Model	Mesh	Output Parameter	Brick8 (in)	Wedge6 (in)	Analytical (in)
Axial Extension	D	6x1x1 (Bri.) 12x1x1 (Wed.)	u_x	$2.99*10^{-5}$	$2.98*10^{-5}$	$3.00*10^{-5}$
Shear and Bending in Strong Axis	D	6x1x1 (Bri.) 12x1x1 (Wed.)	u_z	$1.00*10^{-2}$	$9.93*10^{-1}$	$1.08*10^{-1}$
Shear and Bending in Weak Axis	D	6x1x1 (Bri.) 12x1x1 (Wed.)	u_y	$1.09*10^{-2}$	$1.09*10^{-2}$	$4.32*10^{-1}$
Twisting	D	6x1x1 (Bri.) 12x1x1 (Wed.)	u_y	$2.86*10^{-3}$	$2.11*10^{-3}$	$3.41*10^{-3}$
Pure Bending in Strong Axis	D	6x1x1 (Bri.) 12x1x1 (Wed.)	u_x	$8.38*10^{-5}$	$8.29*10^{-5}$	$9.00*10^{-4}$
Pure Bending in Weak Axis	D	6x1x1 (Bri.) 12x1x1 (Wed.)	u_x	$4.53*10^{-5}$	$4.53*10^{-5}$	$1.80*10^{-3}$

Table 4-12 Straight Beam with Quadratic Wedge Elements (Wedge15) – Displacements at the Free-End

Behavior Mode	Model	Mesh	Output Parameter	Brick20 (in)	Wedge15 (in)	Analytical (in)
Axial Extension	E	6x1x1 (Bri.) 12x1x1 (Wed.)	u_x	$3.01*10^{-5}$	$3.01*10^{-5}$	$3.00*10^{-5}$
Shear and Bending in Strong Axis	E	6x1x1 (Bri.) 12x1x1 (Wed.)	u_z	$1.07*10^{-1}$	$1.06*10^{-1}$	$1.08*10^{-1}$
Shear and Bending in Weak Axis	E	6x1x1 (Bri.) 12x1x1 (Wed.)	u_y	$4.16*10^{-1}$	$4.17*10^{-1}$	$4.32*10^{-1}$
Twisting	E	6x1x1 (Bri.) 12x1x1 (Wed.)	u_y	$2.90*10^{-3}$	$2.85*10^{-3}$	$3.41*10^{-3}$
Pure Bending in Strong Axis	E	6x1x1 (Bri.) 12x1x1 (Wed.)	u_x	$9.00*10^{-4}$	$8.99*10^{-4}$	$9.00*10^{-4}$
Pure Bending in Weak Axis	E	6x1x1 (Bri.) 12x1x1 (Wed.)	u_x	$1.80*10^{-3}$	$1.80*10^{-3}$	$1.80*10^{-3}$

In Table 4-11 and Table 4-12, end displacements of cantilever beam created with linear and quadratic wedge elements under each loading condition are tabulated and the performances of the elements are compared with the analytical results.

Although the axial extension behavior of linear wedge element is the same with linear hexahedron, under other load cases, linear wedge element behaves stiffer. Since the nodes used mutually around cross section have higher stiffness values than the other nodes. In Figure 4-5, cross section of the beam modeled with linear wedge elements are presented. In the figure, stiffness of nodal points 1 and 3 are computed by considering both elements' contributions (Upper and lower).

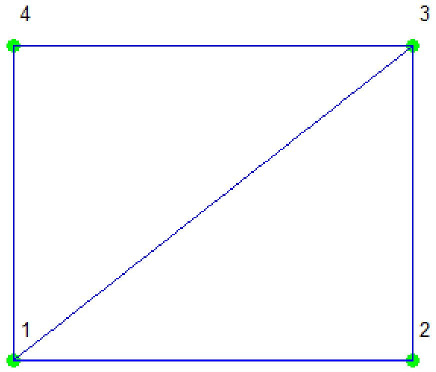

Figure 4-5 Cross Section of Beam with Linear Edge Elements

Same situation is also valid for quadratic wedge element. Similar to previous elements, quadratic element behaves more flexible than linear one and this makes it preferable for each condition except axial extension load case. On the other hand, as stated in "Finite Element" section, wedge elements cannot behave as well as hexahedral elements without any distortion. Hence, wedge elements should be preferred to distorted hexahedral elements.

Table 4-13 Straight Beam with Wedge Elements – Stresses at the Fixed-End

Behavior Mode	Model	Output Parameter	Wedge6 (lb/in^2)	Wedge15 (lb/in^2)	Analytical (lb/in^2)
Axial Extension	D/E	σ_x	5.3*10^1	5.3*10^1	5.00*10^1
Shear and Bending in Strong Axis	D/E	σ_x	1.01*10^3	8.82*10^3	9.00*10^3

Table 4-13 (Continued)

Shear and Bending in Weak Axis	D/E	σ_x	$5.56*10^{2}$	$1.85*10^{4}$	$1.80*10^{4}$
Twisting	D/E	σ_x	$3.86*10^{1}$	$3.07 *10^{2}$	$2.45*10^{3}$
Pure Bending in Strong Axis	D/E	σ_x	$1.85*10^{2}$	$1.57*10^{3}$	$1.50*10^{3}$
Pure Bending in Weak Axis	D/E	σ_x	$1.01*10^{2}$	$3.37*10^{3}$	$3.00*10^{3}$

Stresses at fixed end of the beam are displayed in Table 4-13. According to the table, quadratic elements calculate stresses more accurately. It is possible to improve stress values by using finer mesh providing results close to the actual deformation function of the beam.

In Table 4-14 and Table 4-15, displacements of linear and quadratic tetrahedral elements are displayed. In order to adapt tetrahedrons to the beam geometry, 288 elements were required. Thus, beam with linear tetrahedrons becomes more flexible under shear-bending and moment loading condition than one modeled with hexahedral elements. However performance of the linear tetrahedral element under twisting case is stiffer.

Table 4-14 Straight Beam with Linear Tetrahedral Elements (Tet4) – Displacements at the Free-End

Behavior Mode	Model	Mesh	Output Parameter	Brick8 (in)	Tet4 (in)	Analytical (in)
Axial Extension	A	288 Tet. 6 Bricks	u_x	$2.99*10^{-5}$	$2.98*10^{-5}$	$3.00*10^{-5}$
Shear and Bending in Strong Axis	A	288 Tet. 6 Bricks	u_z	$1.00*10^{-2}$	$1.28*10^{-2}$	$1.08*10^{-1}$
Shear and Bending in Weak Axis	A	288 Tet. 6 Bricks	u_y	$1.09*10^{-2}$	$1.44*10^{-2}$	$4.32*10^{-1}$
Twisting	A	288 Tet. 6 Bricks	u_y	$2.86*10^{-3}$	$8.99*10^{-5}$	$3.41*10^{-3}$
Pure Bending in Strong Axis	A	288 Tet. 6 Bricks	u_x	$8.38*10^{-5}$	$1.07*10^{-4}$	$9.00*10^{-4}$
Pure Bending in Weak Axis	A	288 Tet. 6 Bricks	u_x	$4.53*10^{-5}$	$6.07*10^{-5}$	$1.80*10^{-3}$

Table 4-15 Straight Beam with Quadratic Tetrahedral Elements (Tet10) – Displacements at the Free-End

Behavior Mode	Model	Mesh	Output Parameter	Brick20 (in)	Tet10 (in)	Analytical (in)
Axial Extension	A	288 Tet. 6 Bricks	u_x	$3.01*10^{-5}$	$3.01*10^{-5}$	$3.00*10^{-5}$
Shear and Bending in Strong Axis	A	288 Tet. 6 Bricks	u_z	$1.07*10^{-1}$	$9.55*10^{-2}$	$1.08*10^{-1}$
Shear and Bending in Weak Axis	A	288 Tet. 6 Bricks	u_y	$4.16*10^{-1}$	$3.57*10^{-1}$	$4.32*10^{-1}$
Twisting	A	288 Tet. 6 Bricks	u_y	$2.90*10^{-3}$	$3.10*10^{-3}$	$3.41*10^{-3}$
Pure Bending in Strong Axis	A	288 Tet. 6 Bricks	u_x	$9.00*10^{-4}$	$7.39*10^{-4}$	$9.00*10^{-4}$
Pure Bending in Weak Axis	A	288 Tet. 6 Bricks	u_x	$1.80*10^{-3}$	$1.29*10^{-3}$	$1.80*10^{-3}$

This stiff behavior is valid for quadratic tetrahedral element also. In spite of using 288 quadratic tetrahedral elements, beam with quadratic hexahedral elements behaves more flexible. This situation shows that using tetrahedral elements for regular geometries does not provide good performance. Accordingly, as stated in Finite Elements section, tetrahedral elements were developed for irregular geometries.

Table 4-16 Straight Beam with Tetrahedral Elements – Stresses at the Fixed-End

Behavior Mode	Model	Output Parameter	Tet4 (lb/in^2)	Tet10 (lb/in^2)	Analytical (lb/in^2)
Axial Extension	A	σ_x	$4.53*10^{1}$	$4.98*10^{1}$	$5.00*10^{1}$
Shear and Bending in Strong Axis	A	σ_x	$1.03*10^{2}$	$8.36*10^{3}$	$9.00*10^{3}$
Shear and Bending in Weak Axis	A	σ_x	$5.99*10^{2}$	$1.66*10^{4}$	$1.80*10^{4}$
Twisting	A	σ_x	$2.19*10^{0}$	$1.55*10^{2}$	$2.45*10^{3}$

Table 4-16 (Continued)

Pure Bending in Strong Axis	A	σx	1.77*102	1.44*103	1.50*103
Pure Bending in Weak Axis	A	σx	1.16*102	1.40*103	3.00*103

In Table 4-16, stresses at fixed end of the beam with both linear and quadratic tetrahedral elements are displayed. Similar to previous elements, calculating stress by using quadratic elements is more reliable due to order of its shape function. In addition to this, stress values can be cured by increasing mesh of the structure because it provides more realistic approximation for actual behavior of structure.

4.2.2. Temperature Load

In this part, behaviors of each finite element under temperature loading are examined. 2D and 3D plane models (MacNeal and Harder ,1985) were solved. For each case, displacements and stresses were compared with the analytical solutions.

2D Temperature Load

First, rectangular plate problem was solved in order to verify the performances of two dimensional elements (Quad and TriM) (Figures 4-6 and 4-7). To check nodal displacements and elements stresses, identical models with different restraint conditions were utilized. For displacement verification, only one corner node was fixed in order to see the expansion of the plate (Figures 4-6 and 4-7, Model A). On the other hand, for stresses due to temperature load, the plate was fully restrained (Figures 4-6 and 4-7, Model B). Model properties are presented in Table 4-17.

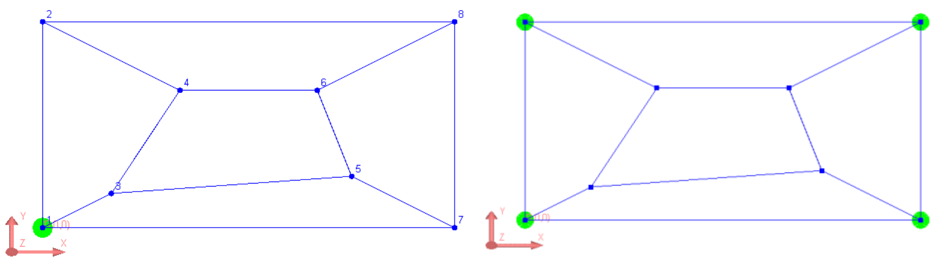

(A) (B)

Figure 4-6 Plate Models with Quadrilateral Elements

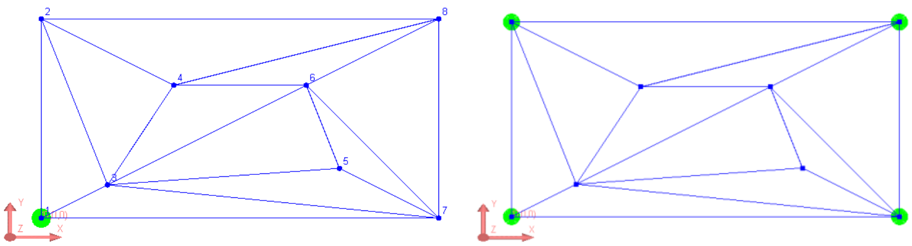

(A) (B)

Figure 4-7 Plate Models with Triangular Elements

Table 4-17 2D Temperature Load – Model Properties

Geometric Properties		Material Properties		Section Properties	
Length:	0.24 in	Modulus of Elasticity:	1,000,000 lb / in^2	Depth:	0.001 in
Height:	0.12 in	Poisson's Ratio:	0.25		
		Thermal Expansion Coefficient:	$5.5*10^{-6}$		

As loading, a 100^{O}F temperature increase was applied to the whole plate. Displacements and stresses due to temperature loading at the top corner of the plate (Node 8) are shown in Table 4-18 for each 2D finite element.

Table 4-18 2D Temperature Load – Displacements and Axial Stresses

Behavior Mode	Output Parameter	Quad4	Quad8	TriM3	TriM6	Analytical
Free Exp.	u_x	$1.72*10^{-4}$	$1.49*10^{-4}$	$1.54*10^{-4}$	$1.77*10^{-4}$	$1.32*10^{-4}$
	u_y	$-1.43*10^{-5}$	$3.30*10^{-5}$	$2.18*10^{-5}$	$-2.32*10^{-5}$	$6.60*10^{-5}$
	σ_{xx}	0	0	0	0	0
	σ_{yy}	0	0	0	0	0
Restr.	u_x	0	0	0	0	0
	u_y	0	0	0	0	0
	σ_{xx}	$-7.33*10^{2}$	$-7.33*10^{2}$	$-7.33*10^{2}$	$-7.33*10^{2}$	$-7.33*10^{2}$
	σ_{yy}	$-7.33*10^{2}$	$-7.33*10^{2}$	$-7.33*10^{2}$	$-7.33*10^{2}$	$-7.33*10^{2}$

According to Table 4-18, distortion also affects negatively the behavior under temperature change load. Similar to previous problems, quadratic element represents the actual behavior better for quad elements. On the other hand, for triangular elements, displacement of linear element is closer to the analytical solution. However, due to geometry of the model, the plate was not modeled by utilizing proper triangular mesh. Accordingly, the results do not represent the performance of the triangular elements under temperature change load. On the other hand, each element can calculate the same stress amount due to temperature change loading with analytical solutions.

Each finite element calculates total element stresses by the summation of stress due to temperature and stress due to displacements. Because of this, since Model A is free to expand due to temperature, stresses on the body are equal to zero. When expansion is restrained (Model B), only stresses due to temperature occurs. As seen in Table 4-18, each form of quadrilateral and triangular elements calculate stresses due to temperature change correctly.

3D Temperature Load

In this part, behavior of 3D finite elements under temperature loading is discussed. For this purpose, square plate proposed by MacNeal and Harder (1985) was modeled with each 3D finite element (Figure 4-8). Model properties are stated in Table 4-19.

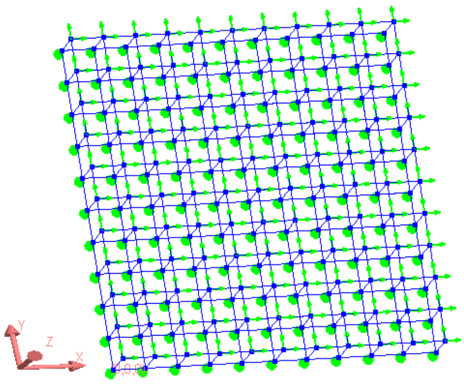

Figure 4-8 3D Temperature Load

Table 4-19 3D Temperature Load – Model Properties

Geometric Properties		Material Properties	
Length:	10 in	Modulus of Elasticity:	1,000,000 lb / in^2
Width:	10 in	Poisson's Ratio:	0.25
Depth:	1 in	Thermal Expansion Coefficient:	$5.5*10^{-6}$

In this model, nodes at bottom edge are totally restrained, other nodes are restrained in x and y direction. Similar to previous example, a 100^{O}F temperature increase was applied to the model as loading. Stress values in x and y direction at anywhere of the plate were compared with the analytical results in Tables 4-20 and 4-21 for each 3D element.

Table 4-20 3D Temperature Load – Axial Stresses (Bricks and Wedges)

Output Parameter	Brick8 (lb/in^2)	Brick20 (lb/in^2)	Wedge6 (lb/in^2)	Wedge15 (lb/in^2)	Analytical (lb/in^2)
σ_{xx} Anywhere in plate	$-7.33*10^2$	$-7.33*10^2$	$-7.33*10^2$	$-7.33*10^2$	$-7.33*10^2$
σ_{yy} Anywhere in plate	$-7.33*10^2$	$-7.33*10^2$	$-7.33*10^2$	$-7.33*10^2$	$-7.33*10^2$

Table 4-21 3D Temperature Load – Axial Stresses (Tetrahedrons)

Output Parameter	Tet4 (lb/in^2)	Tet10 (lb/in^2)	Analytical (lb/in^2)
σ_{xx} Anywhere in plate	$-7.33*10^2$	$-7.33*10^2$	$-7.33*10^2$
σ_{yy} Anywhere in plate	$-7.33*10^2$	$-7.33*10^2$	$-7.33*10^2$

According to Tables 4-20 and 4-21, stresses obtained from each elements type are same with the analytical one. This situation shows that calculations of stress due to temperature load algorithms of each element are acceptable.

4.3. Verification of Heat Transfer Analysis

Square and rectangular plate problems suggested by Reddy and Gartling (2010) were solved in order to verify the implementation heat transfer analysis algorithms and corresponding elements.

4.3.1. Square Plate Problem

In this part, heat conduction and heat generation definitions of the finite elements and steady-state solution algorithm was examined. For that purpose, quarter of a square plate suggested by Reddy and Gartling (2010) was solved with each element and performances of the elements were compared. Since the plate has four different symmetry axes (Figure 4-9 (A), x=0, y=0, x=y, and x=-y), solving only quarter of the plate provides simplicity. Square plate and quarter plate are presented in Figure 4-9 (A) and Figure 4-9 (B), respectively.

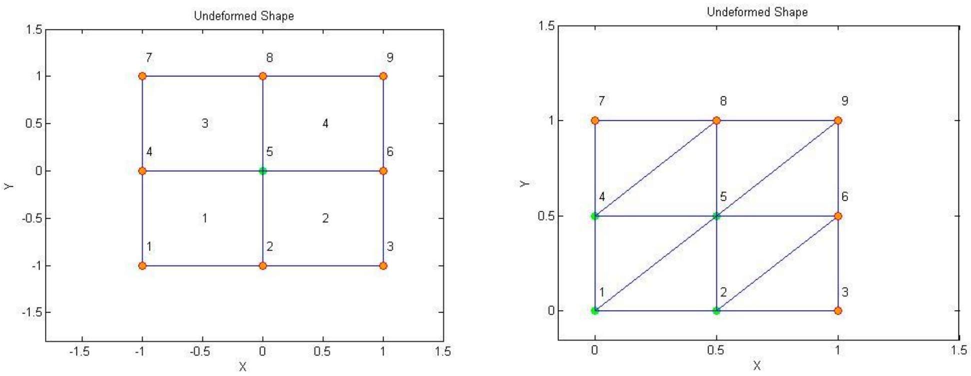

(A) (B)

Figure 4-9 Plate Models. (A) Full Plate. (B) Quarter Plate

As shown in Figure 4-9(A), temperature of nodes at edges are fixed to 0^{o}C (orange nodes) and heated uniformly with the amount of 1 W/cm^3. Since the plate is symmetric, quarter of it (Figure 4-9 (B)) is taken into account with no surface flux at symmetry edges (line x=0 and line y=0). Then temperature values at free nodes (green nodes) are observed. Model properties of quarter of plate are tabulated in Table 4-22.

Table 4-22 Square Plate Problem – Model Properties

Geometric Properties		Material Properties		Section Properties	
Length:	1 cm	Heat Conduction Coefficient:	1 W/cm ^{o}C	Depth:	1 cm
Width:	1 cm	Heat Generation per Volume:	1 W/cm^3		

Temperature distribution of full plate and quarter of that plate are shown in Figure 4-10 (A) and Figure 4-10 (B), respectively.

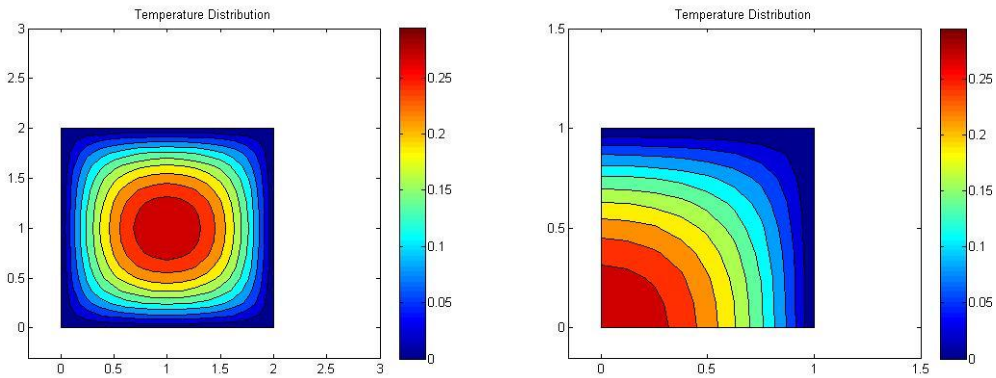

(A) (B)

Figure 4-10 Temperature Distribution of Full and Quarter Plate

Results obtained from the models with different elements are compared with the analytical results. Two different mesh densities were utilized for each case except tetrahedral elements. Nodal temperatures along the edge (x=0) for each model are presented in Table 4-23.

Table 4-23 Performances of Each Element

Element	Mesh	Temperatures at Nodes (°C)				
		y=0	y=0.25	y=0.5	y=0.75	y=1.0
Analytical	-	0.2947	0.2789	0.2293	0.1397	0.0000
Quad4	4	0.3107	0.2759	0.2411	0.1205	0.0000
	16	0.2984	0.2824	0.2322	0.1414	0.0000
Quad8	4	0.2941	0.2791	0.2292	0.1395	0.0000
	16	0.2946	0.2788	0.2293	0.1397	0.0000
TriM3	8	0.3125	0.2708	0.2292	0.1146	0.0000
	32	0.3013	0.2805	0.2292	0.1392	0.0000
TriM6	8	0.2950	0.2786	0.2296	0.1395	0.0000
	32	0.2947	0.2789	0.2294	0.1397	0.0000
Brick8	4	0.3107	0.2759	0.2411	0.1205	0.0000
	16	0.2984	0.2824	0.2322	0.1414	0.0000
Brick20	4	0.2941	0.2790	0.2292	0.1396	0.0000
	16	0.2946	0.2788	0.2293	0.1397	0.0000
Wedge6	8	0.3125	0.2708	0.2292	0.1146	0.0000
	32	0.3013	0.2805	0.2292	0.1392	0.0000
Wedge15	8	0.2950	0.2786	0.2296	0.1395	0.0000
	32	0.2947	0.2789	0.2294	0.1397	0.0000
Tet4	294	0.2939	0.2712	0.2177	0.1294	0.0000
Tet10	294	0.2946	0.2734	0.2293	0.1324	0.0000

According to the values in Table 4-23, it can be seen that using quadratic elements give closer results to the analytical ones when compared with the linear elements. Moreover, modeling with finer mesh provides better approximation of the actual temperature distribution function; therefore, accuracy of the solution increases.

When the performances of 2D and 3D elements are compared, their results are completely the same. Such a result is expected, since temperature distribution through the thickness is zero for this problem, 3D element behaves like 2D element.

Due to adaptation problem of tetrahedral elements to overall structure, more elements were required. Even so, linear element conducts less thermal energy when compared with the linear hexahedral element. On the other hand, results of quadratic tetrahedron are very close to the analytical ones.

Final point is that in general, accuracy of triangular elements is better than the quadrilateral elements. As heat generation load is applied to the body, not to nodal points, using finer mesh increases the accuracy of calculation of equivalent nodal load. In order to adapt triangular elements to geometry of the structure, more triangular elements are needed. Accordingly, using triangular elements behave better than the rectangular ones.

4.3.2. Rectangular Plate Problem

In addition to the element performances, linear steady-state and transient solution algorithms were tested by solving the rectangular plate problem suggested by Reddy and Gartling (2010). In this model, all types of loading and boundary condition definitions were verified. The rectangular plate model is presented in Figure 4-11.

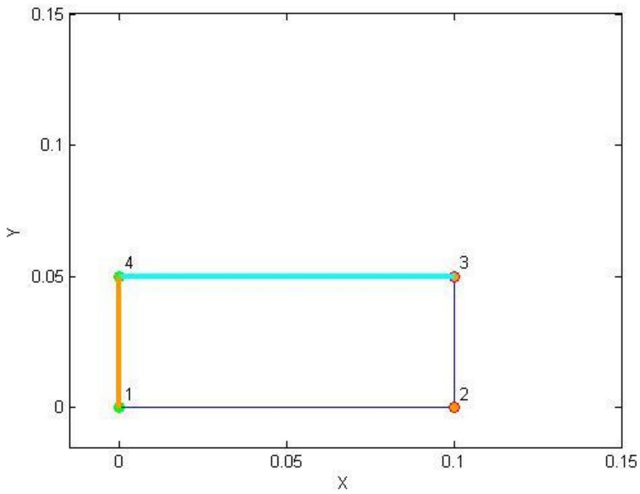

Figure 4-11 Rectangular Plate Model

As shown in Figure 4-11, temperature values of the nodes at the right side of the plate and colored with orange (2 and 3) are fixed to 25^{O}C. At the left side (orange line) and top side (light blue line) of the plate, surface flux and heat convection are defined, respectively. Moreover, heat generation exists in whole plate. Temperatures of nodes at right edge are fixed to 25^{O}C. Model properties are tabulated in Table 4-24.

Table 4-24 Rectangular Plate Problem – Model Properties

Geometric Properties		Material Properties		Section Properties
Length:	0.1 m	Heat Conduction Coefficient:	0.4 W/m ^{O}C	Depth: 1 m
Width:	0.05 m	Heat Convection Coefficient:	60 W/m^2	
		Ambient Temperature:	25^{O}C	
		Flux:	3,500 W/m^2	
		Heat Generation:	135,300 W/m^3	

The problem defined above was solved for each finite element and results were compared with the analytical solutions. Temperature values at node 1, node 4 and midpoint of node 3 and node 4, and flux amount at node 1 (Figure 4-11) of each model are tabulated in Table 4-26 and temperature distribution of the plate is illustrated in Figure 4-12. Results in Table 4-25 were obtained from linear steady-state analysis.

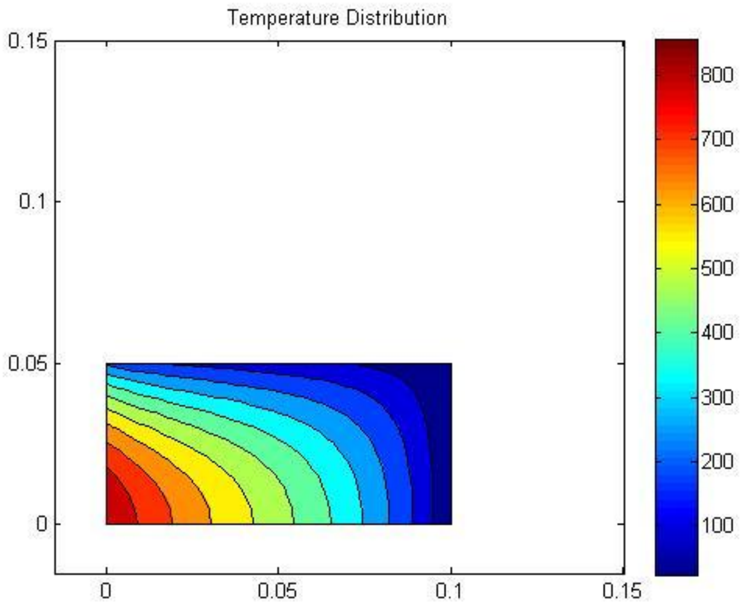

Figure 4-12 Temperature Distribution of Rectangular Plate Modeled with TriM3 Elements

Table 4-25 Performances of Elements in Element Library

Element Type	Number of Elements	1		Middle of points 3 and 4	4
		Temperature (^{O}C)	Flux (x) (W/m^2)	Temperature (^{O}C)	Temperature (^{O}C)
Analytical	-	$8.54*10^2$	$3.50*10^3$	$1.28*10^2$	$2.34*10^2$
Quad4	25	$8.55*10^2$	$3.12*10^3$	$1.28*10^2$	$2.27*10^2$
Quad8	25	$8.54*10^2$	$3.47*10^3$	$1.28*10^2$	$2.33*10^2$
TriM3	50	$8.55*10^2$	$3.21*10^3$	$1.28*10^2$	$2.32*10^2$
TriM6	50	$8.54*10^2$	$3.49*10^3$	$1.28*10^2$	$2.33*10^2$
Brick8	25	$8.55*10^2$	$3.12*10^3$	$1.28*10^2$	$2.27*10^2$
Brick20	25	$8.54*10^2$	$3.48*10^3$	$1.28*10^2$	$2.33*10^2$
Wedge6	50	$8.55*10^2$	$3.21*10^3$	$1.28*10^2$	$2.32*10^2$
Wedge15	50	$8.54*10^2$	$3.49*10^3$	$1.28*10^2$	$2.33*10^2$
Tet4	137	$8.40*10^2$	$2.14*10^3$	$1.18*10^2$	$2.86*10^2$
Tet10	137	$8.61*10^2$	$3.68*10^3$	$1.26*10^2$	$2.31*10^2$

This problem shows performances of surface load algorithms such as heat convection and surface flux of each element. As shown in Table 4-25, similar to previous example, quadratic elements represent the actual behavior better. Moreover, temperature distribution along z direction is zero then, results of 2D and 3D elements are the same except models with tetrahedrons. When the plate was modeled with unsymmetrical tetrahedral mesh, there is a nonzero temperature distribution along the plate thickness which causes a deviation from analytical results. In fact, the plate has symmetry along thickness; accordingly, temperature gradient along its thickness must be zero.

Rectangular plate was modeled with 1000 TriM3 elements and analyzed with the linear transient solution algorithm to check its accuracy. The analysis was repeated four times with different versions of the algorithm; i.e. Explicit and implicit integration with consistent heat capacitance matrix, explicit and implicit integration with lumped heat capacitance matrix. The model is shown in Figure 4-13. In addition to the properties of the model stated above, analysis time was taken as 40000 seconds. The results of linear transient analysis procedure are tabulated in Table 4-26.

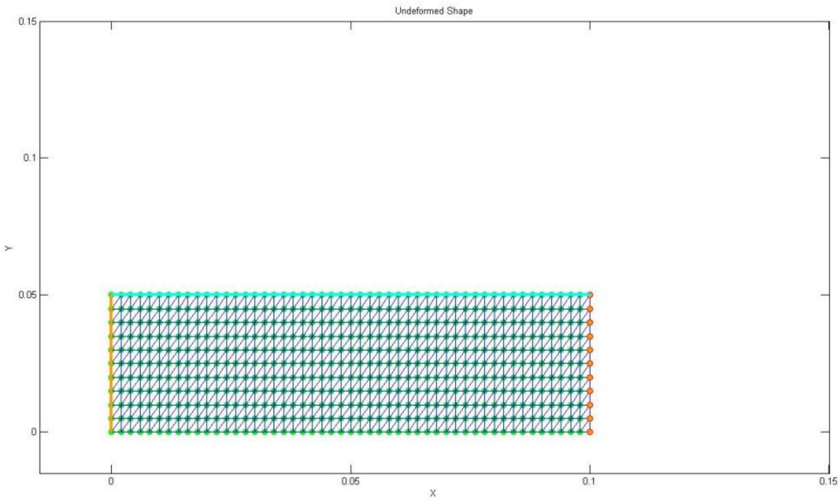

Figure 4-13 Rectangular Plate Modeled with 1000 TriM3 Elements

Table 4-26 Performance of Heat Transfer Analysis Algorithms

TriM3 1000 Elements t = 40000 seconds	Temperatures at Node 1 (^{O}C)
Steady-state	854.51
Explicit Transient (lumped)	853.55
Explicit Transient	853.57
Implicit Transient (lumped)	853.53
Implicit Transient	853.55

According to results of Table 4-26, temperature values obtained from implicit and explicit algorithm are close to each other. Similarly, using lumped or consistent heat capacitance matrix does not create important difference between the results of each other. Therefore, lumped energy storage change matrix can be used to reduce computational costs.

4.4. SUMMARY

To sum up, according to the structural analysis results, linear finite elements represent the axial extension behavior better; whereas, quadratic elements are more suitable for shear-bending and pure bending conditions. Since shear-bending and pure bending behaviors are higher order polynomial, linear elements does not fit this higher order polynomial.. The performances of linear elements under shear-bending and pure bending conditions are improved by increasing mesh of the model.

Meshing cross-section of the beam provides more flexible behavior because it refuses the assumption “plane sections remain plane”. Moreover, distortion reduces the accuracy of the elements. According to the results, parallelogram shaped distortion is more suitable for linear elements; whereas, trapezoidal shaped distortion is better for quadratic elements.

When triangular and quadrilateral elements are compared, quadrilateral elements behave more flexible. If the mechanism through the thickness of the element is ignored (i.e. neglecting the Poisson Effect), the behaviors of quadrilateral and hexahedral elements are completely the same. Otherwise, quadrilateral element is more flexible. Then, wedge and tetrahedral elements are stiffer than the hexahedral elements.

Heat transfer performances of the finite elements are similar to the structural analysis performances. Since the equation of heat transfer is not linear, quadratic elements represent the behavior better. In addition, increasing mesh provides better approximation of the actual behavior.

If the temperature gradient through the thickness of the element is ignored, the behaviors of the quadrilateral and hexahedral elements are completely the same. Finally, triangular elements are better for heat transfer problems due to having more accurate loading calculations.

CHAPTER 5

CASE STUDY

5.1. Introduction

According to PTI structures having large plans with short floor to floor distance such as parking structures are subjected to four different types of shortening. These are shortenings due to pre-compression in post-tension slabs, creep, shrinkage, and temperature change. Usually expansion/shortening of slabs due to temperature changes are up to one third of total shortening of slabs (PTI). Therefore, axial deformation of slabs due to temperature changes should be taken into account while designing the expansion joints, diaphragm reinforcement and slab column/wall connections.

In this chapter, the effect of thermal loading (temperature change) on slab stresses and internal forces of vertical components were investigated. For this purpose, top floors of two typical L-shaped buildings, parking and office buildings were modeled. In other words, the same structure was solved by utilizing different thermal conditions of parking structure and office structure, separately.

Both cases were solved by utilizing heat transfer and structural analysis, sequentially (coupled analysis in weak form). First, temperature distributions of the components were obtained by performing linear transient heat transfer analysis. Then, the structures were solved by utilizing linear static solution algorithm and stresses over the slabs and internal forces at columns and walls were computed.

5.2. Model Properties

As a case study, top story of a typical L-shaped building was modeled. This structure has a uniform and continuous moment frame system. In order to increase the lateral stiffness of the building, shear walls were added to the system. Plan view of the building and section properties of each structural element are presented in Figures 5-1 and 5-2, respectively.

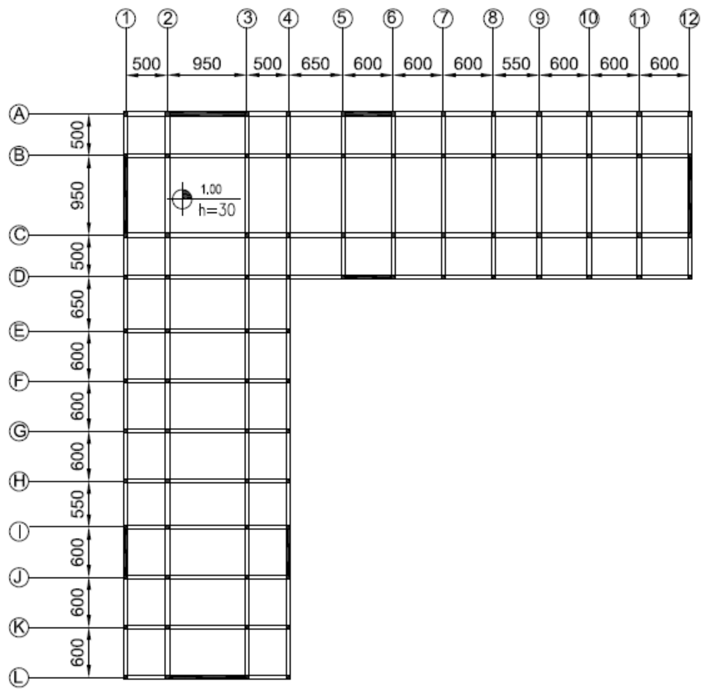

Figure 5-1 Plan View of L-Shaped Structure

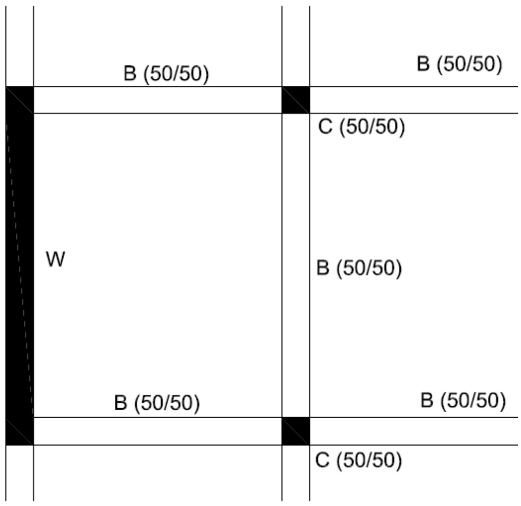

Figure 5-2 Section Properties of Structural Elements

As seen in Figure 5-2, each column and beam has square section whose dimensions are 50x50 cm. Similarly, the thicknesses of shear walls are 50 cm also. Floor to floor height is 400 cm. Finally, slab thicknesses were taken into account as 30 cm. 3D model of the L-shaped structure is shown in Figure 5-3.

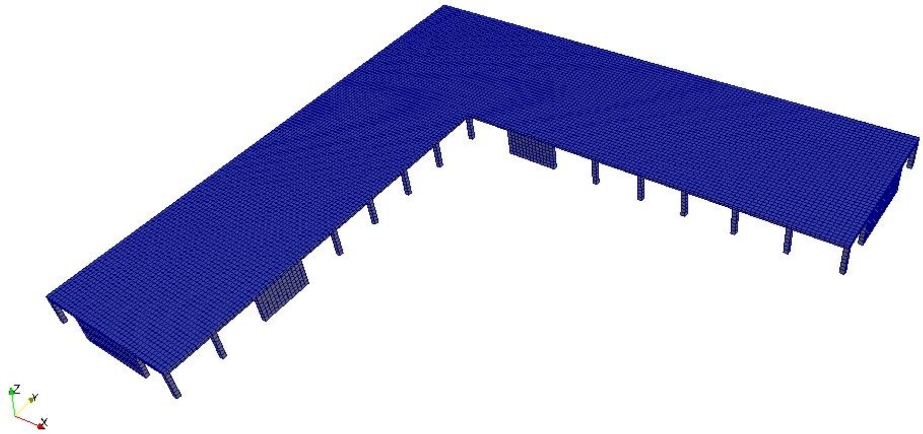

Figure 5-3 3D Model of L-Shaped Structure

Top story of an L-shaped structure was investigated under thermal loading. Each structural element was modeled by using three dimensional hexagonal (Brick) elements. Therefore, 35595 nodes and 21580 linear hexahedral elements were utilized to model this building. Slab element was meshed with two elements throughout the thickness in order to get temperature values of nodes at center level of the slab. This also provides more accurate temperature distribution on section of the slab. Meshing of structural elements is shown in Figure 5-4. According to verification results of linear hexahedron element, the current mesh size may not be sufficient to represent the actual bending behavior at columns and walls. On the other hand, since both cases were solved by using the model with the same mesh, approximately the same amount of error occurred for both cases.

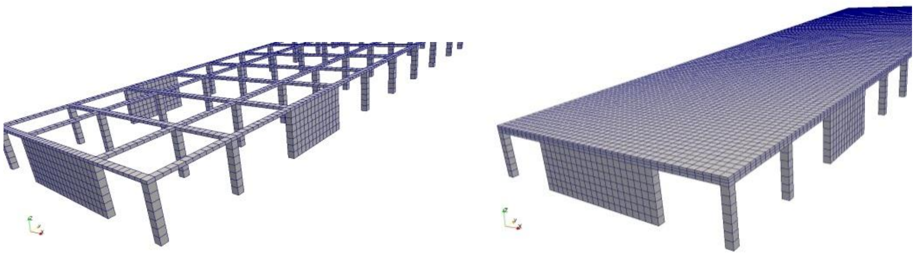

Figure 5-4 Model Mesh

These buildings were modeled with C35 reinforced concrete. Material properties of L-shaped structures are listed in Table 5-1.

Table 5-1 Material Properties of Parking Structure

Mechanical Properties		Chemical Properties	
Modulus of Elasticity: (TS500, 2000)	33000 MPa	Heat Conduction Coefficient: (ASHRAE, 2001)	1.5 W/m ^{O}K
Poisson's Ratio: (TS500, 2000)	0.2	Heat Convection Coefficient: (Air) (Free Conv.) (Lewis et al, 2004)	15 W/m^{2} ^{O}K
Thermal Expansion Coefficient: (TS500, 2000)	0.00001 /^{O}C	Specific Heat Capacity: (ASHRAE, 2001)	1 kJ/kg ^{O}K
Density: (Kosmatka et al., 2003)	2400 kg / m^{3}		

Although the heat convection coefficient depends on the geometry of the structure, in this study, heat convection coefficient was taken into account as a constant value.

For the thermal analysis, the initial temperature of concrete was assumed as 14^{O}C during the casting period (no hydration effect). For the first case parking structure, hourly temperature values in Adana at June 23rd (Bulut et al.) were applied to both bottom and top surface of the slab. On the other hand, for second case, the same temperature distribution was accounted only for the outside of the building; whereas, inside temperature was assumed to be 20^{O}C constant temperature. Temperature distribution of Adana on June 23rd is presented in Figure 5-5.

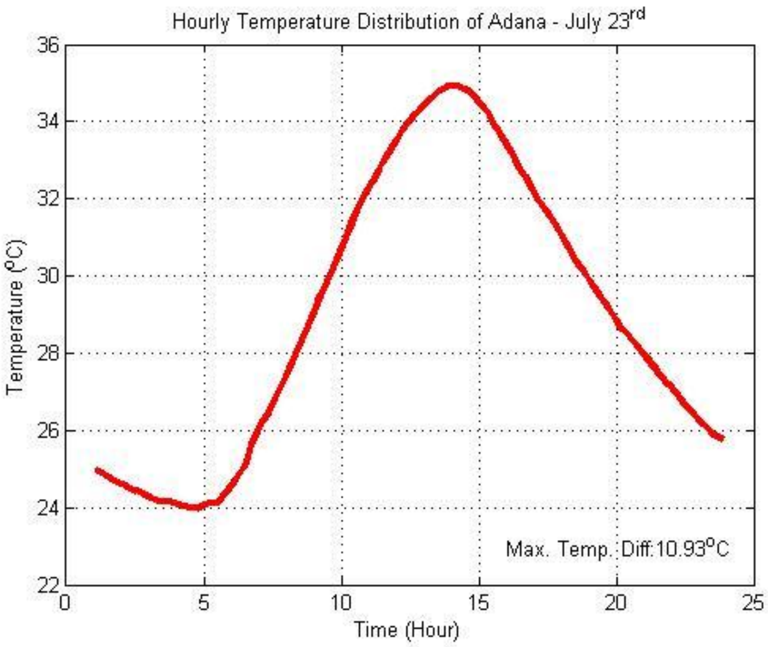

Figure 5-5 Hourly Temperature Distribution of Adana

Currently, the radiation effects were ignored; accordingly, these buildings were subjected to only heat convection as ambient thermal load. Another assumption is that no convection occurs at faces of the columns and walls of the system. Heat convection was defined only at the top face of the slabs and bottom faces of the beams and slabs.

5.3. Case 1: Parking Structure

For the parking structure, both top and bottom faces of the slab were subjected to same ambient temperature presented in Figure 5-5. In order to obtain temperature distribution of the slab, transient heat transfer analysis was performed for twenty-four hour duration and structure was solved by utilizing structural analysis for the several times, 5th, 12th, 14th, 20th and 24th hours. In 5th and 14th hours, air temperature reaches the minimum and maximum, respectively. In addition to this, stress distribution at 12th, 14th, and 24th hours were investigated. The temperature distribution of the slab along the slab section and at a single point for different times were presented in Figures 5-7 and 5-8, respectively. The location of the section cut and the point is presented in Figure 5-6. Units of temperature values presented in Figure 5-7 are ^{O}C.

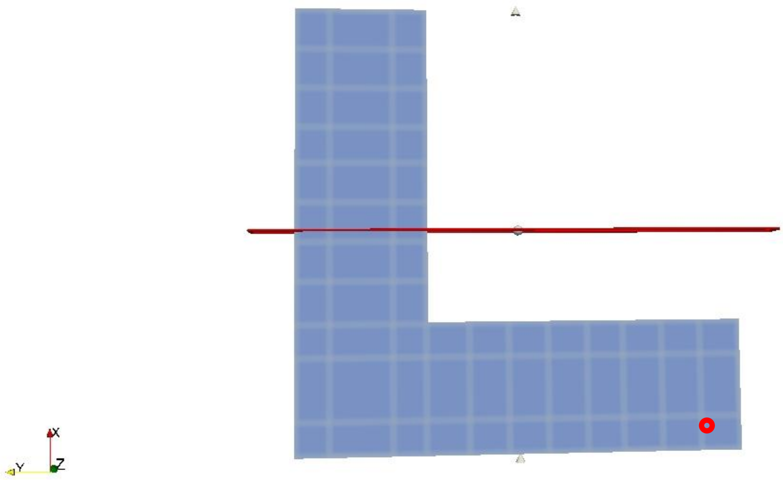

Figure 5-6 Section Cut of the Slab and Point 1

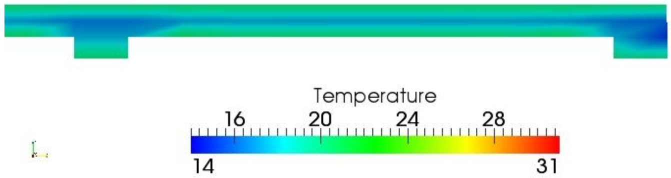

(A)

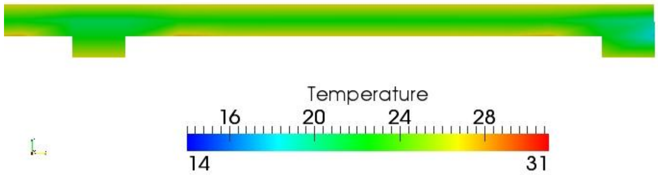

(B)

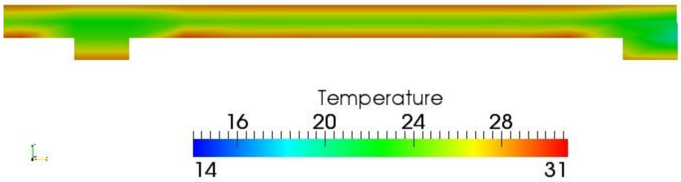

(C)

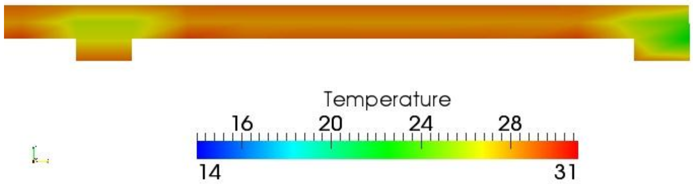

(D)

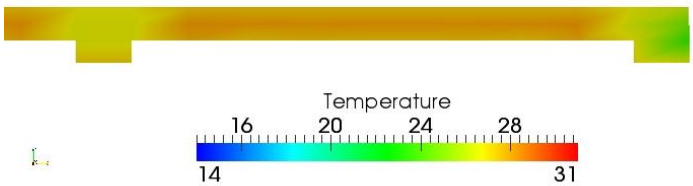

(E)

Figure 5-7 Temperature Distribution of Slab of Parking Structure (A) 5th hour (B) 12th hour (C) 14th hour (D) 20th hour (E) 24th hour

According to Figure 5-7, the top and bottom faces of the concrete slab were exposed to the same thermal energy and this energy expanded toward the midlevel of the section during warming of the slab and temperature of midlevel increases (Figure 5-7 A to D). Whereas during cooling, the thermal energy stored inside the concrete slab transforms to the ambient; accordingly, heat energy stored in the concrete section expands through the faces (Figure 5-7 E). In Figure 5-8, temperature gradients of the slab through thickness at Point 1 (Figure 5-6) are presented for the times stated above.

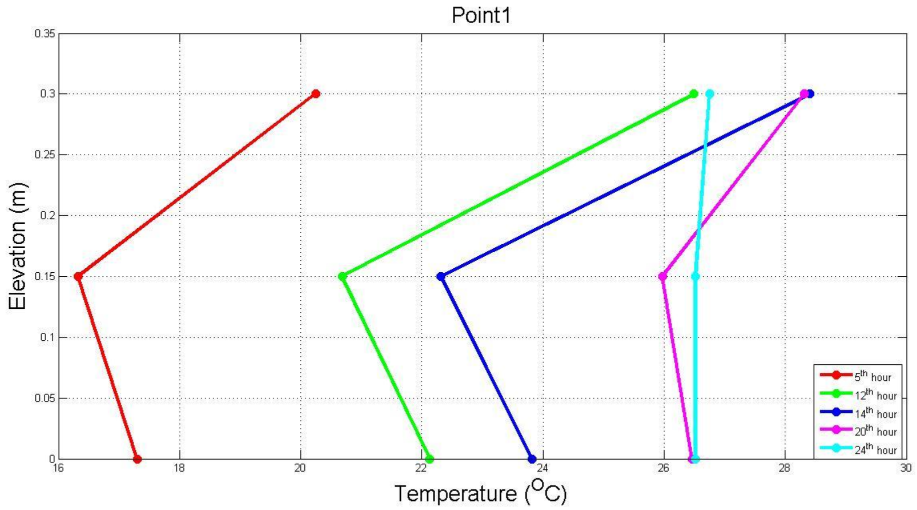

Figure 5-8 Temperature Gradient through Thickness

Since the thermal conditions at bottom and top faces of the slab were the same, same temperature values are expected for both faces. However, bottom faces of some slab elements have no contact with the air due to existence of beams. Therefore, the temperature values of bottom and top faces of the slab are not totally the same in spite of having the same ambient temperature. However, for whole slab, this behavior cannot create serious temperature gradient through the thickness. The mean temperature values at top, center and bottom layers of the whole slab are presented in Figure 5-9.

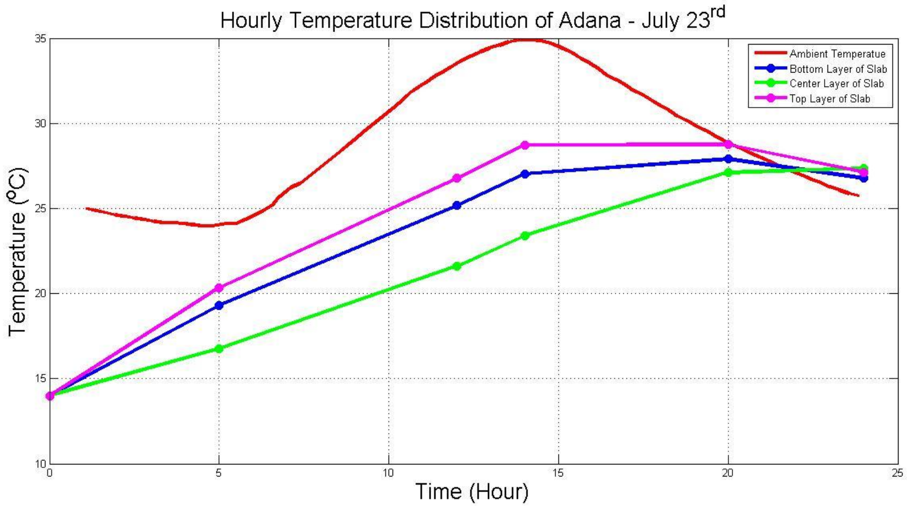

Figure 5-9 Mean Temperature Distribution of Slab Layers (Parking Structure)

According to the Figure 5-9, the temperature of the slab increases 15th hour and then cooling began at top and bottom faces. At the end of the day, temperature values through thickness were equalized and the structure became slightly hotter than the ambient.

Then, linear static analysis was performed for each time stated above by utilizing the temperature gradients for current time. This way, stress distribution of the slab was obtained. Displacements of midlevel slabs for 24th hour are presented in Figure 5-10. Moreover, stress distributions of slab for 5th, 12th, 14th, 20th, and 24th are presented in Figures 5-11 to 5-15, respectively.

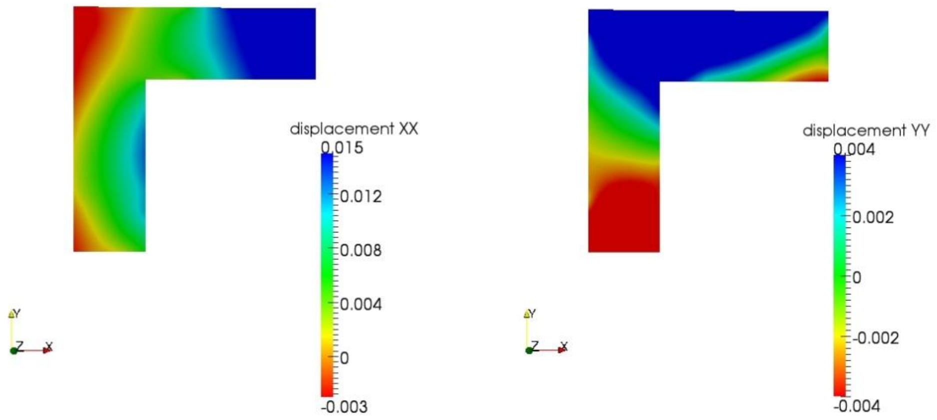

(A) (B)

Figure 5-10 Displacements at 24th Hour. (A) x Direction (B) y Direction

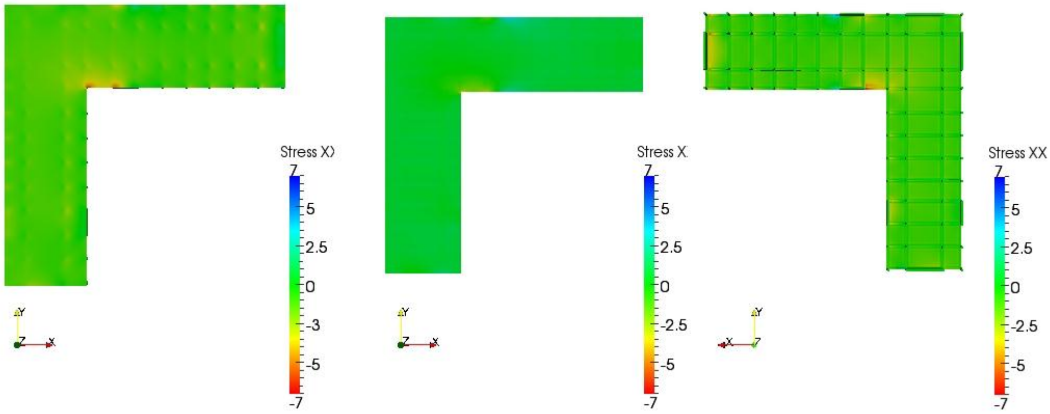

(A) Top – Mid – Bottom Layer

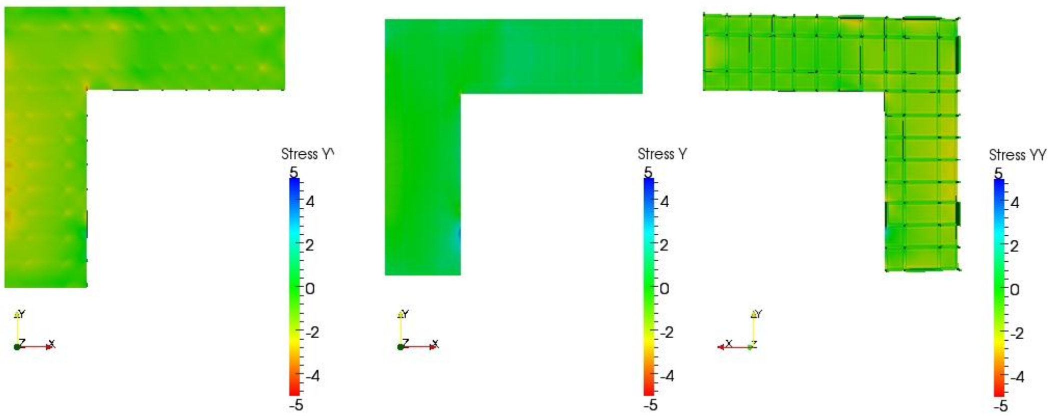

(B) Top – Mid – Bottom Layer

Figure 5-11 Stress Distributions of Slab at 5th Hour (Parking Structure) (MPa). (A) Stresses in x Direction. (B) Stresses in y Direction

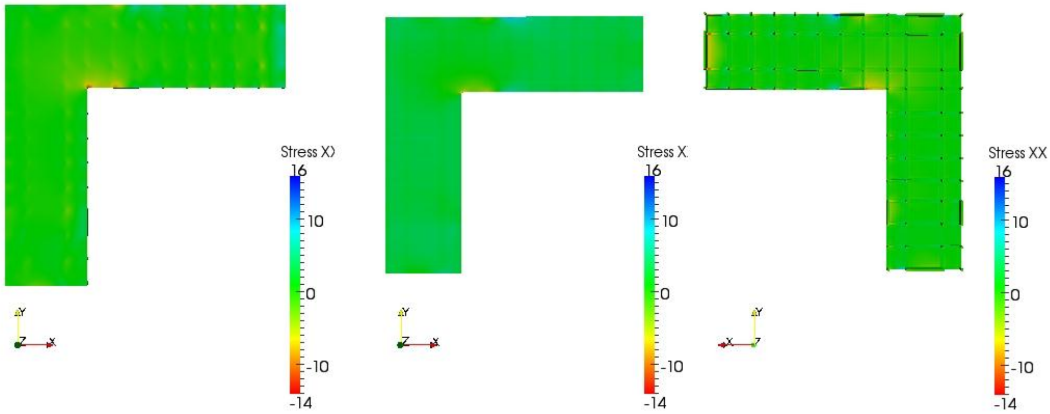

(A) Top – Mid – Bottom Layer

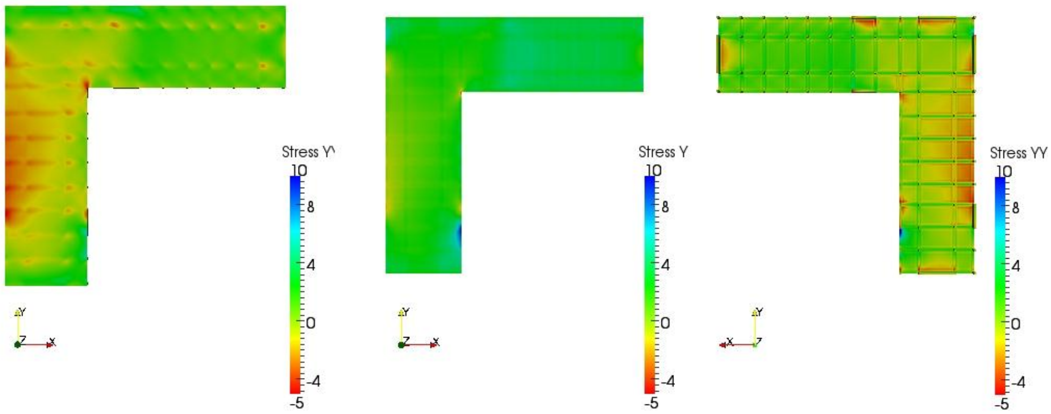

(B) Top – Mid – Bottom Layer

Figure 5-12 Stress Distributions of Slab at 12th Hour (Parking Structure) (MPa). (A) Stresses in x Direction. (B) Stresses in y Direction

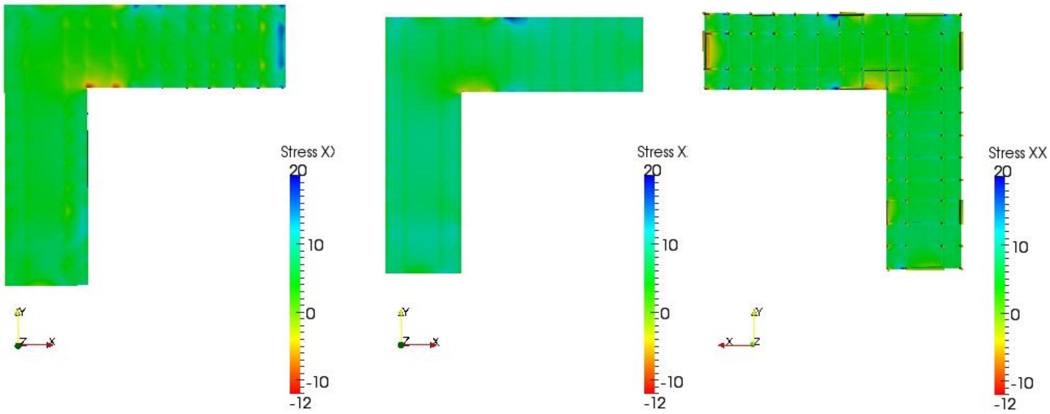

(A) Top – Mid – Bottom Layer

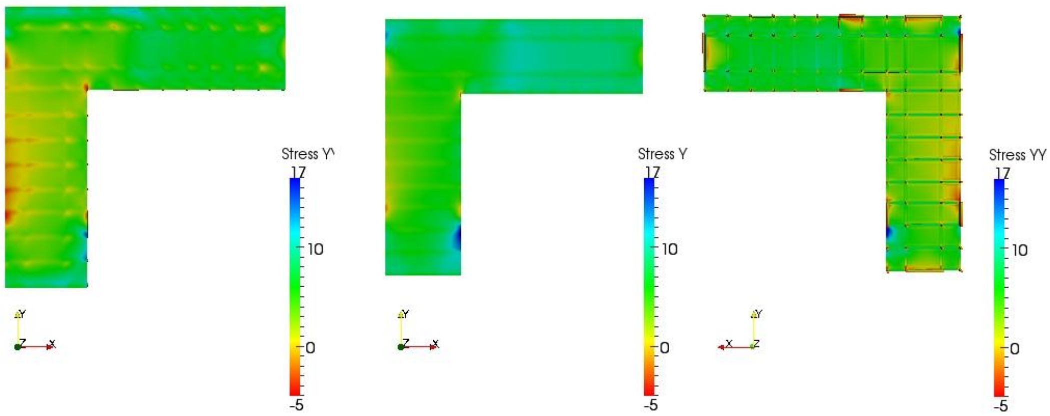

(B) Top – Mid – Bottom Layer

Figure 5-13 Stress Distributions of Slab at 14th Hour (Parking Structure) (MPa). (A) Stresses in x Direction (B). Stresses in y Direction

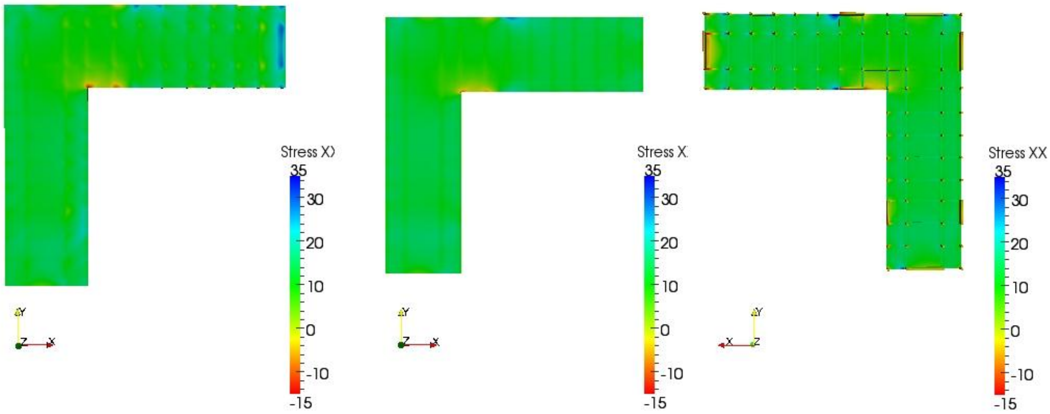

(A) Top – Mid – Bottom Layer

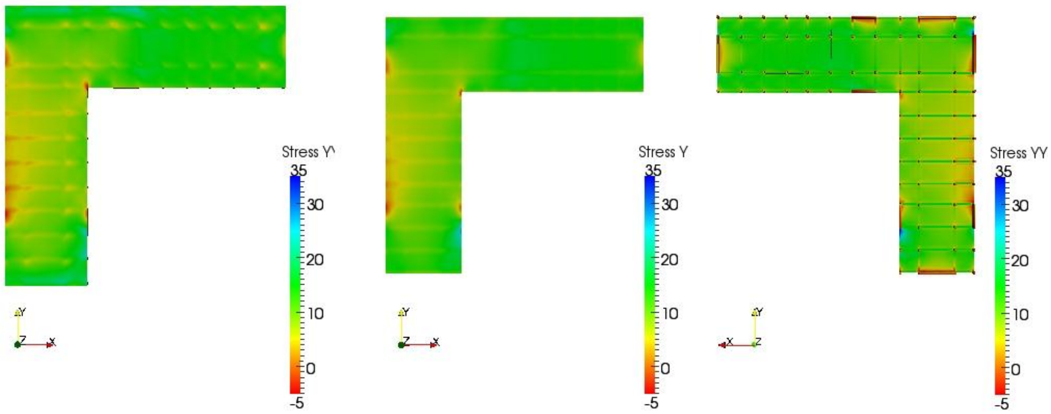

(B) Top – Mid – Bottom Layer

Figure 5-14 Stress Distributions of Slab at 20th Hour (Parking Structure) (MPa). (A) Stresses in x Direction (B). Stresses in y Direction

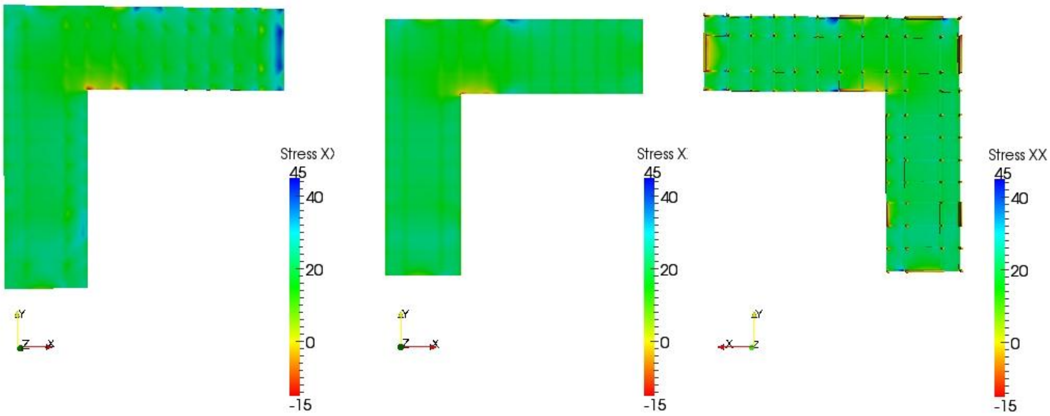

(A) Top – Mid – Bottom Layer

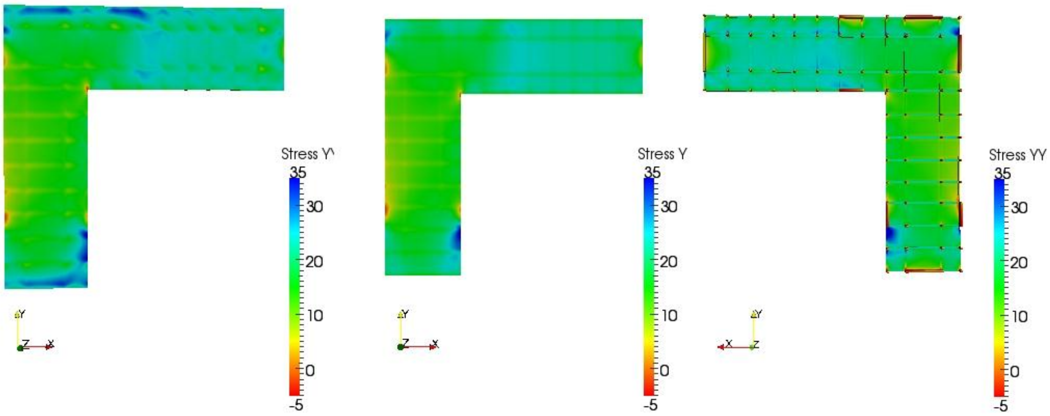

(B) Top – Mid – Bottom Layer

Figure 5-15 Stress Distributions of Slab at 24th Hour (Parking Structure) (MPa). (A) Stresses in x Direction (B). Stresses in y Direction

Since the orientation and location of the shear walls are not the same for both direction, x and y, displacements are not symmetric for both axes (Figure 5-9). Stress distributions in Figures 5-10 to 5-15 are related to the displacement distribution. Indeed, significant stresses occur at location where displacements have been restrained. For x direction, existing of shear wall being close to inner corner of L-shape causes significant compressive stress concentration at that region. On the other hand, for y direction, displacements at region between the inner corner of L-shape and shear walls in y direction are approximately zero; accordingly, corresponding compressive stress spreads at that region and magnitude is less than the one in x direction.

Since the top and bottom faces are subjected to the same ambient condition, stress distributions for each time were similar to each other. These stress distributions alter towards to the midlevel of the slab (Figures 5-10 to 5-15). At midlevel of the slab section, the zero displacement region becomes smaller with respect to time due to the increase in temperature change; accordingly, the region being subjected to compressive stress increases with time.

5.4. Case 2: Office Structure

In the second case, same structure was solved with different thermal conditions. As a matter of fact, inside temperature of the structure was assumed to be constant (20^{O}C) for twenty-four hours. On the other hand, top face of the slab was subjected to same convection conditions of parking structure. Similar to previous case, this structure was solved by utilizing linear transient heat transfer analysis and at several times and temperature change values at nodes of the slab were obtained. These temperature distributions at same slab section with are presented in Figure 5-16.

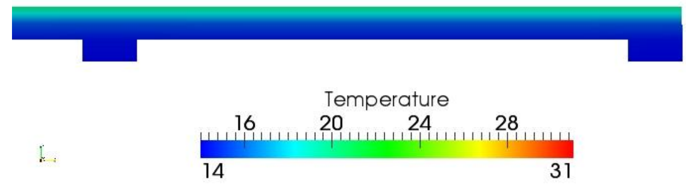

(A)

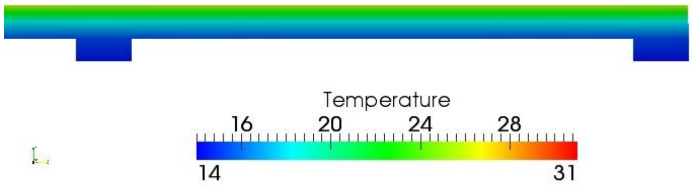

(B)

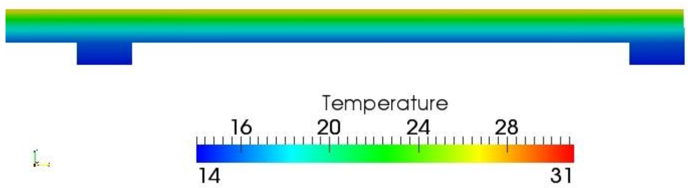

(C)

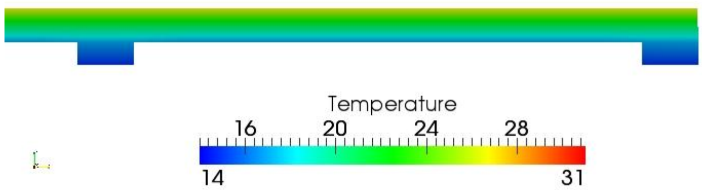

(D)

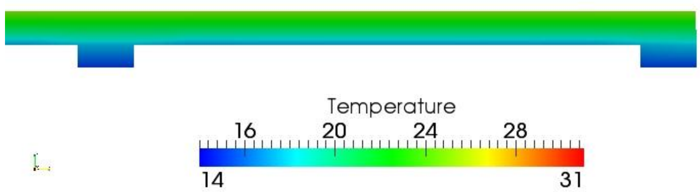

(E)

Figure 5-16 Temperature Distribution of Slab of Office Building (A) 5th hour (B) 12th hour (C) 14th hour (D) 20th hour (E) 24th hour

Since the ambient temperature affecting the top face is higher than the inside temperature, heat energy moves from top to bottom (Figure 5-16 A to D). Accordingly, bottom face has always the lowest temperature; whereas, top face has the highest temperature value. During cooling, temperature of the top faces begins to drop (Figure 5-16 E). The temperature gradient at Point 1 and mean temperature values at top, center and bottom layers are presented in Figures 5-17 and 5-18, respectively.

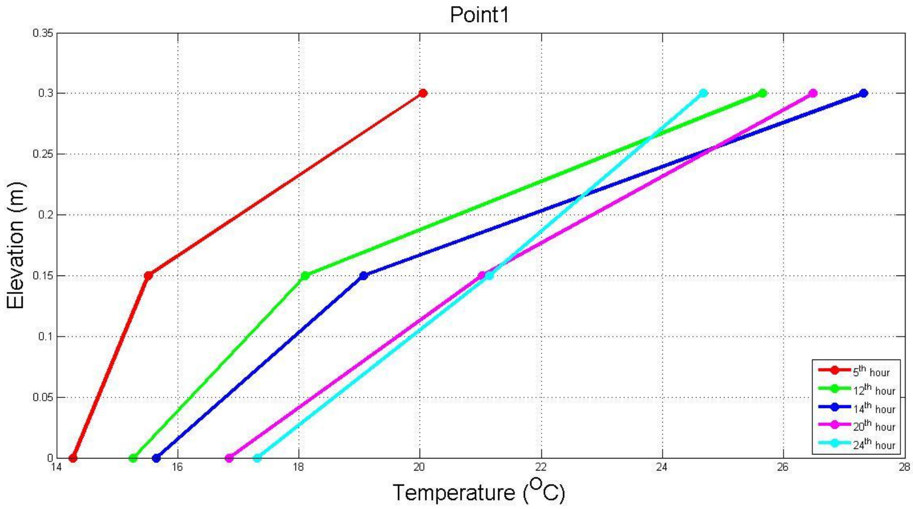

Figure 5-17 Temperature Gradient through Thickness at Point1

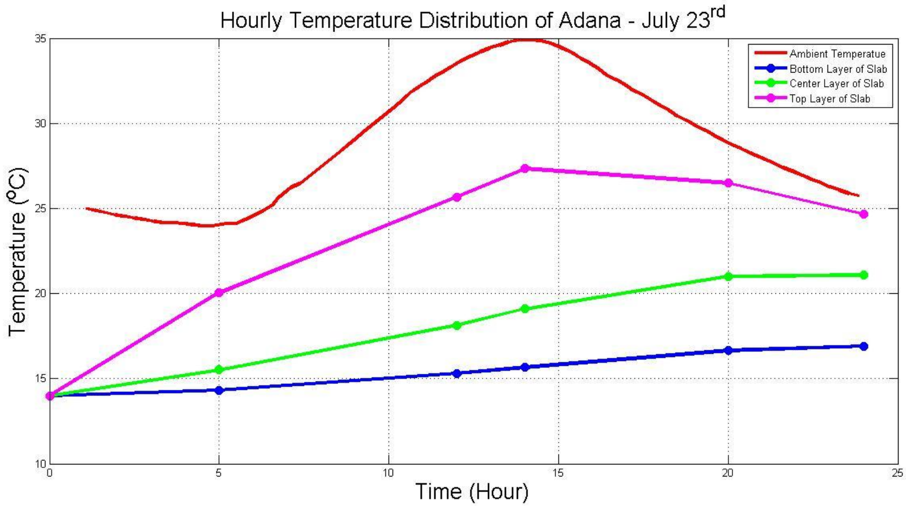

Figure 5-18 Mean Temperature Distribution of layers of Slab (Office Structure)

Mean values of the layers represent the behavior of slab under ambient temperature distributions. As seen in Figure 5-18, increase of temperature of bottom layer is about 3°C; whereas, temperature changes in top layer is approximately 13°C. As a result, temperature gradient occurs through the thickness of the slab of office structure. In addition, although, after 14th hour, top layer begins to cool, whereas the other layers stay warm for the whole day.

Then linear static solutions were performed for each time stated above and the stress distributions over the slab were obtained. Displacements of the slab in both x and y directions at the end of the day are presented in Figure 5-19. Moreover, stress distributions at top, middle, and bottom layers of the slab for 5th, 12th, 14th, 20th, and 24th are presented in Figures 5-20 to 5-24, respectively.

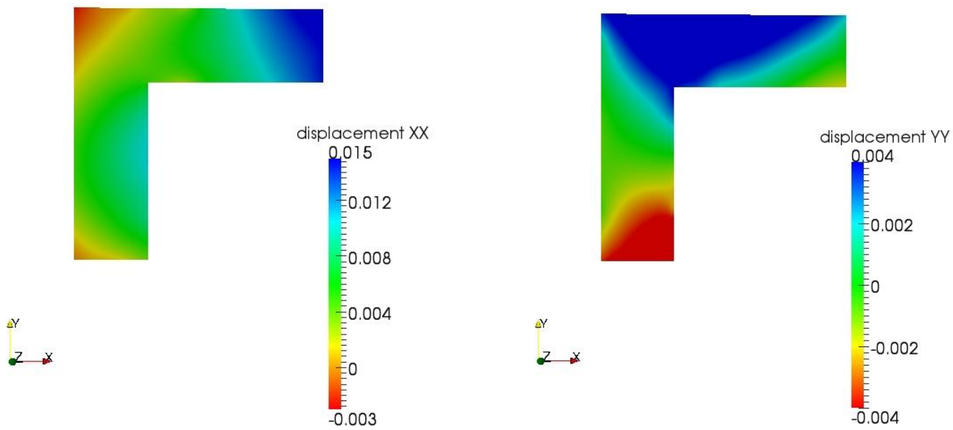

(A) (B)

Figure 5-19 Displacements at 24th Hour. (A) x Direction (B) y Direction

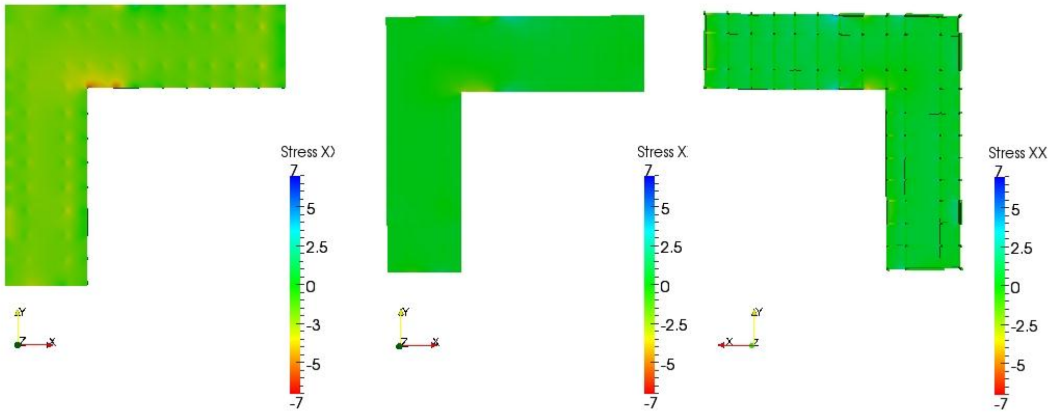

(A) Top – Mid – Bottom Layer

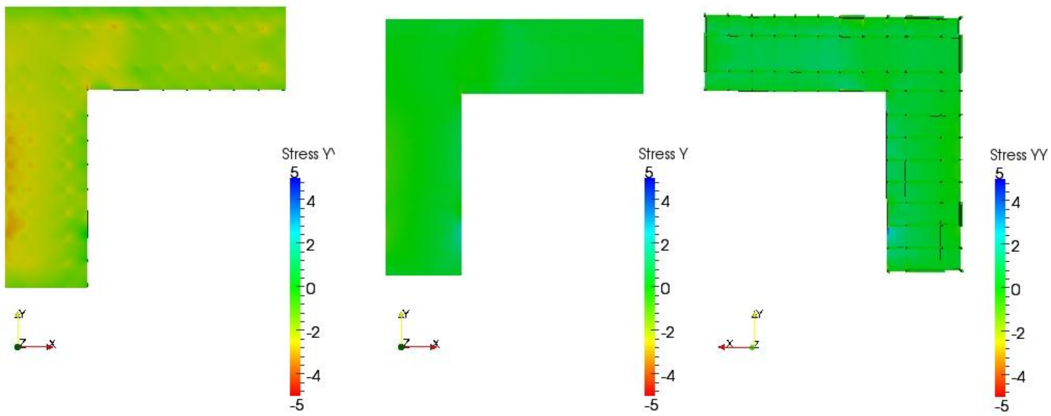

(B) Top – Mid – Bottom Layer

Figure 5-20 Stress Distributions of Slab at 5th Hour (Office Structure) (MPa). (A) Stresses in x Direction. (B) Stresses in y Direction

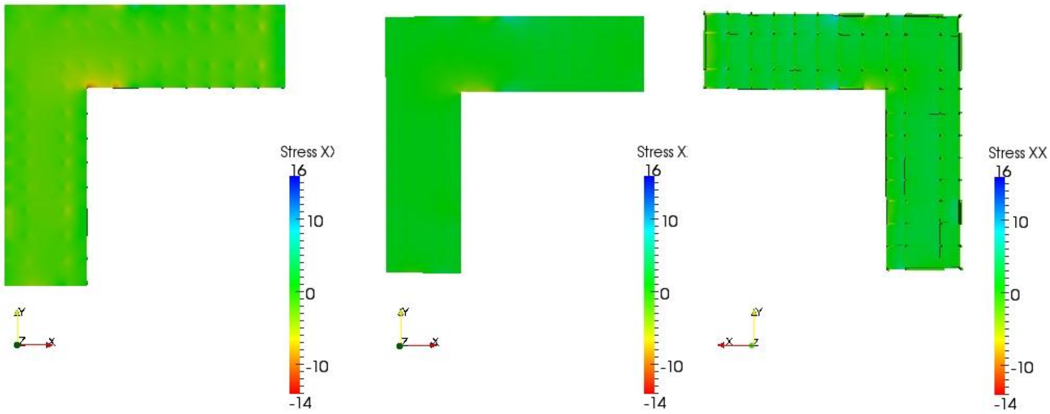

(A) Top – Mid – Bottom Layer

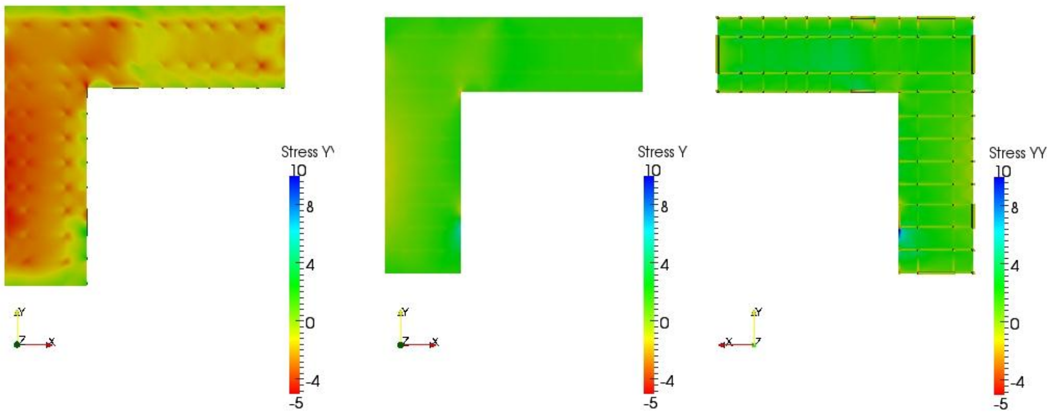

(B) Top – Mid – Bottom Layer

Figure 5-21 Stress Distributions of Slab at 12th Hour (Office Structure) (MPa). (A) Stresses in x Direction. (B) Stresses in y Direction

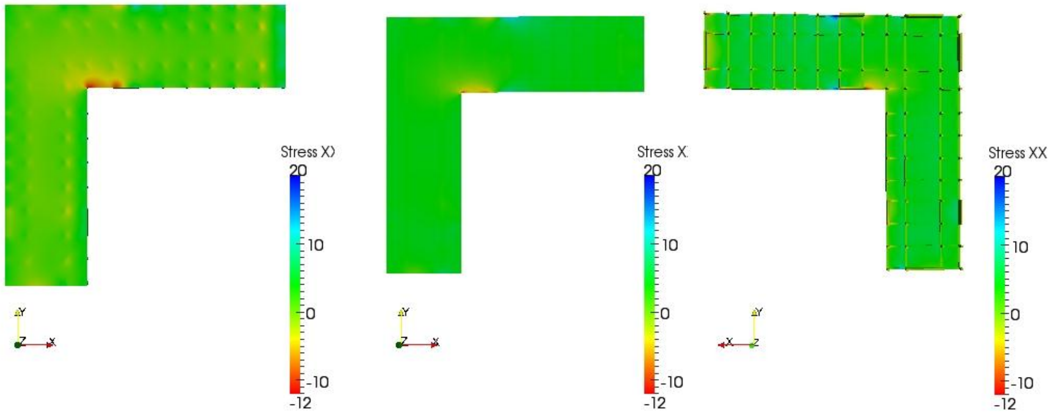

(A) Top – Mid – Bottom Layer

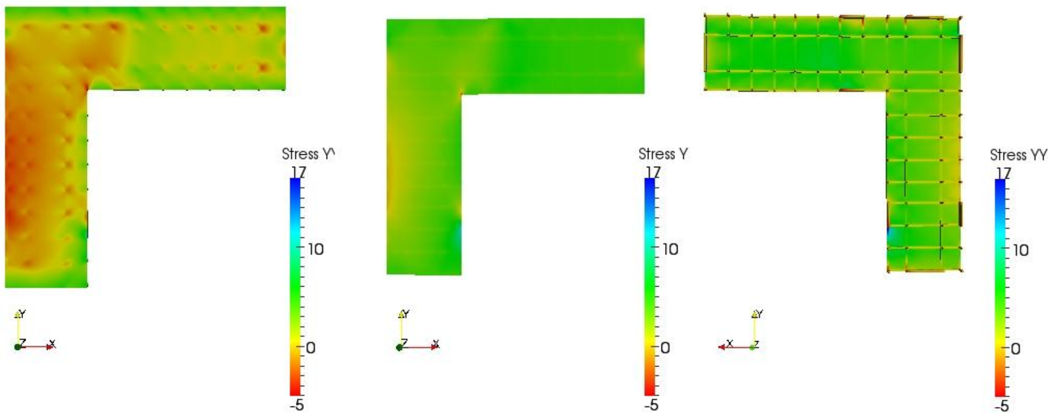

(B) Top – Mid – Bottom Layer

Figure 5-22 Stress Distributions of Slab at 14th Hour (Office Structure) (MPa). (A) Stresses in x Direction (B). Stresses in y Direction

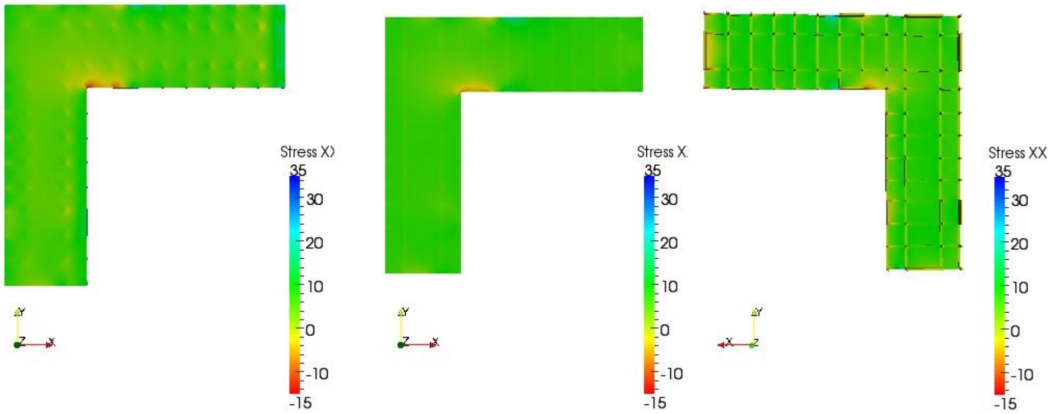

(A) Top – Mid – Bottom Layer

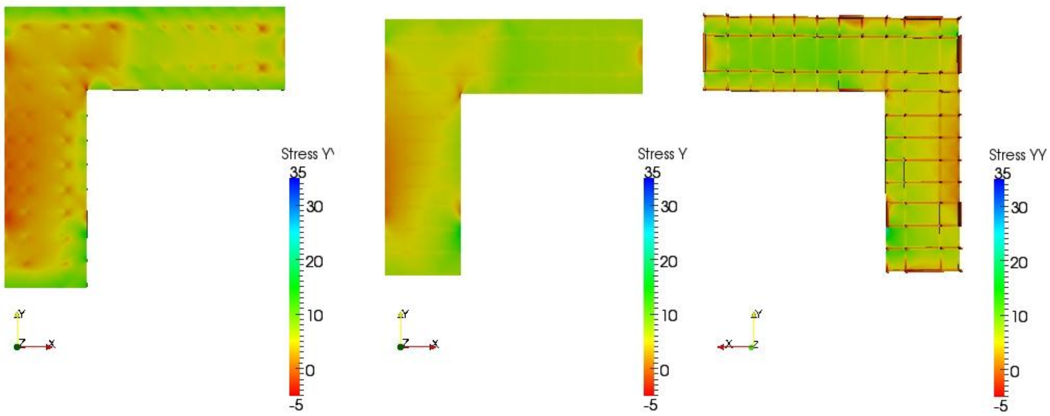

(B) Top – Mid – Bottom Layer

Figure 5-23 Stress Distributions of Slab at 20th Hour (Office Structure) (MPa). (A) Stresses in x Direction (B). Stresses in y Direction

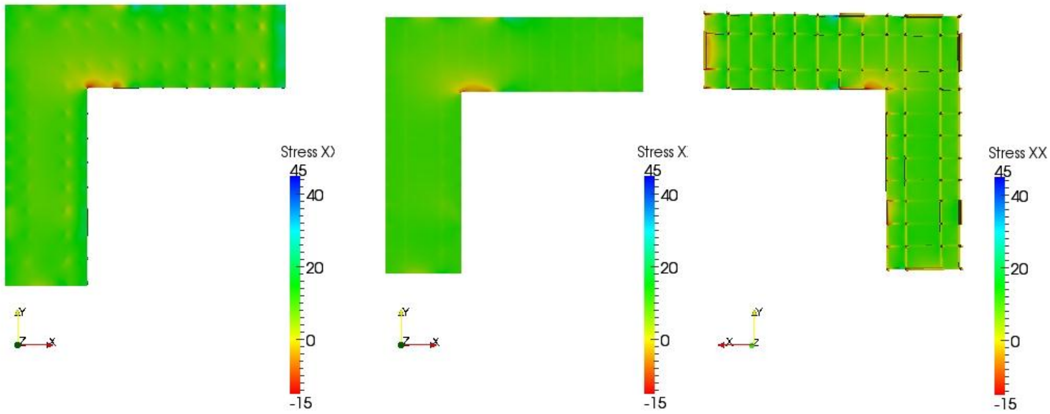

(A) Top – Mid – Bottom Layer

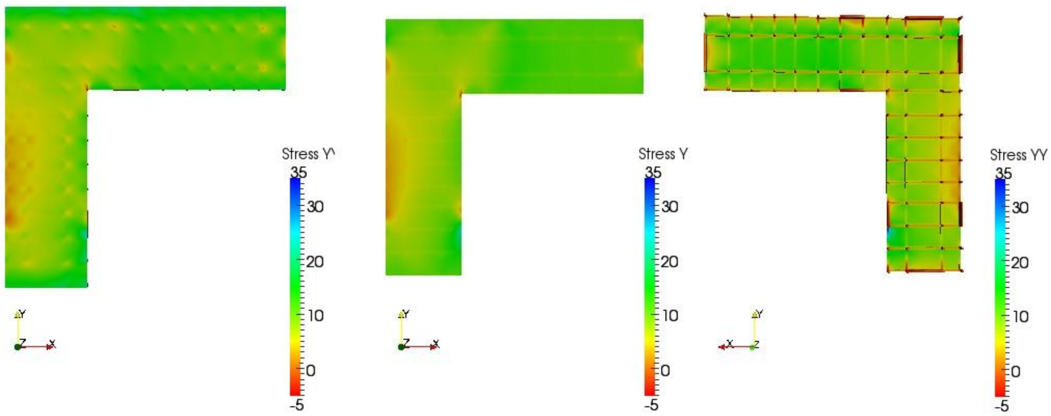

(B) Top – Mid – Bottom Layer

Figure 5-24 Stress Distributions of Slab at 24th Hour (Office Structure) (MPa). (A) Stresses in x Direction (B). Stresses in y Direction

According to Figure 5-19, although general displacement distributions in both x and y direction of midlevel of the slab at the end of the day are similar with the parking structure, the displacements of office structure less due to having smaller total temperature change amount.

Similar to first case, concentrated compressive stress occurs between inner corner of L-shape and shear walls in x direction due to restrained displacements. On the other hand, in y direction, zero displacement region is largely at region between inner corner and shear wall in y direction (Figure 5-19 B), compressive stresses spread to that region; accordingly, their amounts are less than the other direction. According to Figures 5-20 to 5-24, at midlevel, the same regions stated above becomes subjected to compression due increase in temperature and the compression region expands with time.

5.5. Comparison

Two top floors of typical L-shaped structures were subjected to different thermal loading and different stress distributions generated on slabs of the structures. Indeed, due to different thermal gradient on slab section, behaviors of the structural components were not the same.

Since parking structure was subjected to ambient conditions at both faces, temperature of the slab along its thickness was balanced with the outer face temperatures. Accordingly, the general temperature distribution of slab resembles to the distribution of ambient temperature with respect to time. On the other hand, slab of office building were subjected to heat convection with different ambient conditions for bottom and top faces. Accordingly, it was impossible for midlevel temperature to be balanced with the outer face temperatures and temperature gradient through thickness is not constant for the duration of day. Because of this reason, the slab temperature of parking structure is higher than the office building. Accordingly, displacements occurring on parking structure are greater than the office structure.

For both cases, the same regions between shear wall and inner corner of L-shape are critical. Although parking structure has higher temperature change, top face of the office structure is subjected to higher compressive stress due to having inconstant temperature gradient. Indeed, the mid and bottom levels of slab of office structure cannot expand as much as the top face; in other words, bottom levels try to restrict the expansion of the top level. Accordingly, at top face of slab of office building, additional compressive stresses occur. Similarly, slab of parking structure is subjected to higher tension. For both structures, stress distribution in x direction of top, midlevel and bottom faces at 14^{th} hour are presented in Figures 5-25.

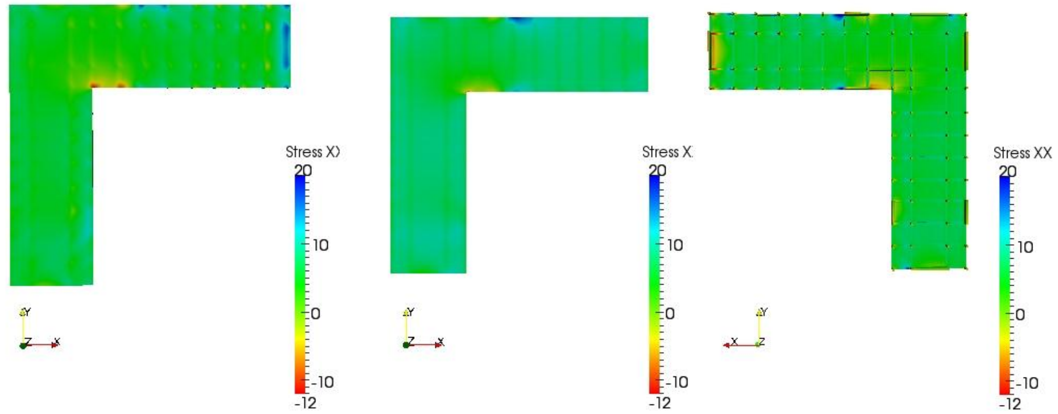

(A)

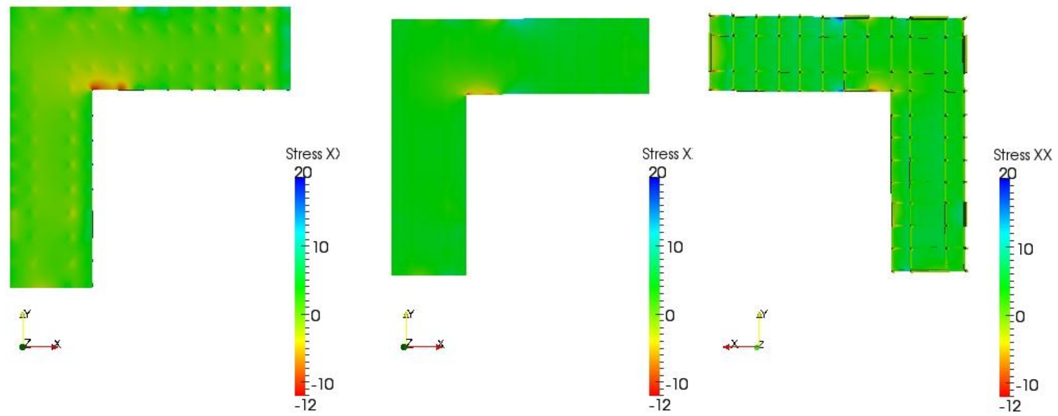

(B)

Figure 5-25 Stress Distribution in x Direction at 14th Hour. (A) Parking Structure (B) Office Structure

Internal forces of vertical elements, Wall 7 and Column 35, were investigated for both structures and compared with each other. These vertical components and their locations are presented in Figure 5-26.

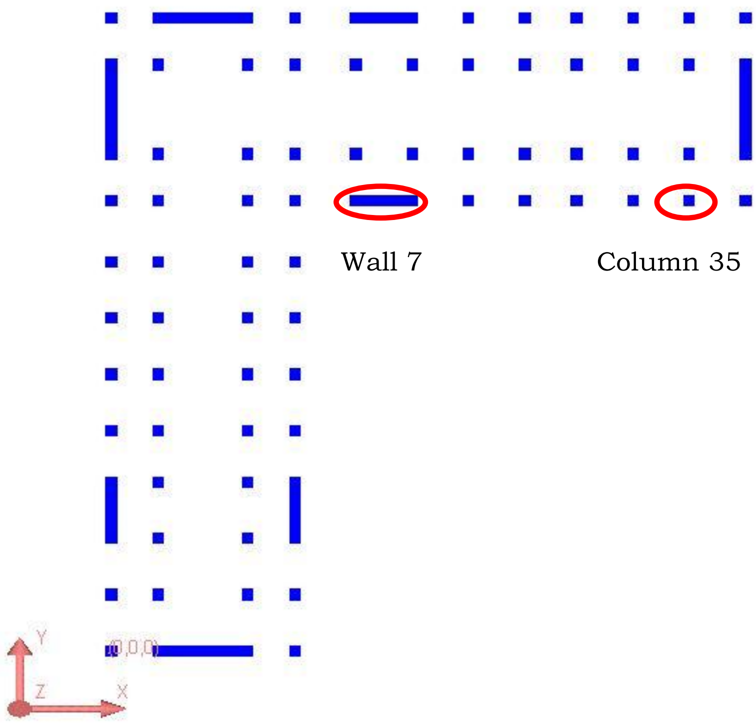

Figure 5-26 Plan View of L-Shaped Structure – Wall 7 and Column 35

For internal force investigation, Wall 7 was selected since maximum compressive stress in x direction occurs at region near it. Moreover, since maximum displacement in x direction occurs at region right hand side of the structure, the internal forces of Column 35 due to thermal load was examined. Shear force in x direction of bottom level of Wall 7 and Column 35 are presented in Figures 5-27 and 5-28, respectively.

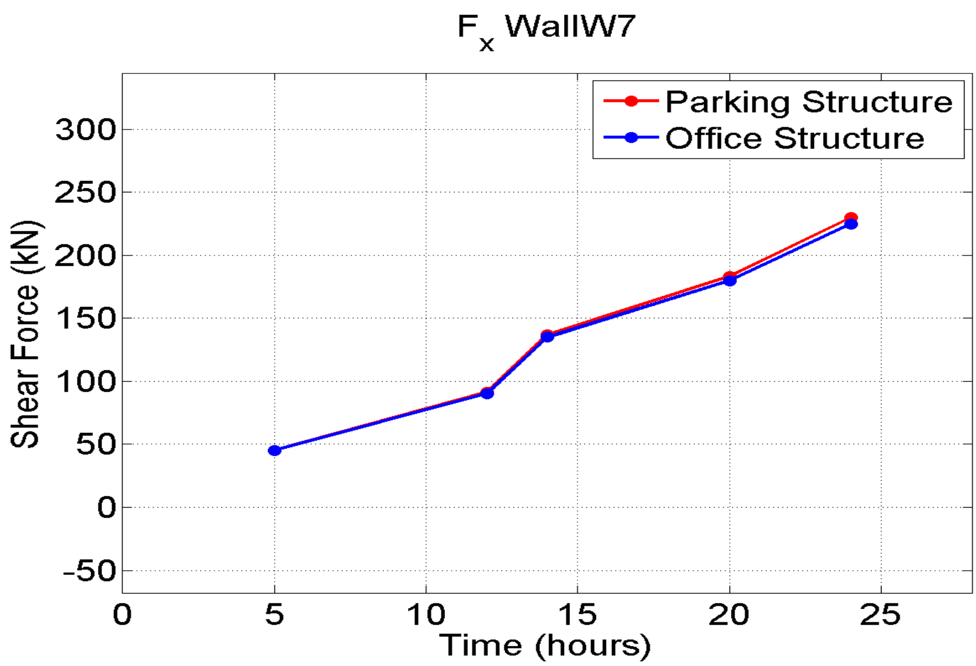

Figure 5-27 Shear Reaction Forces - Wall 7

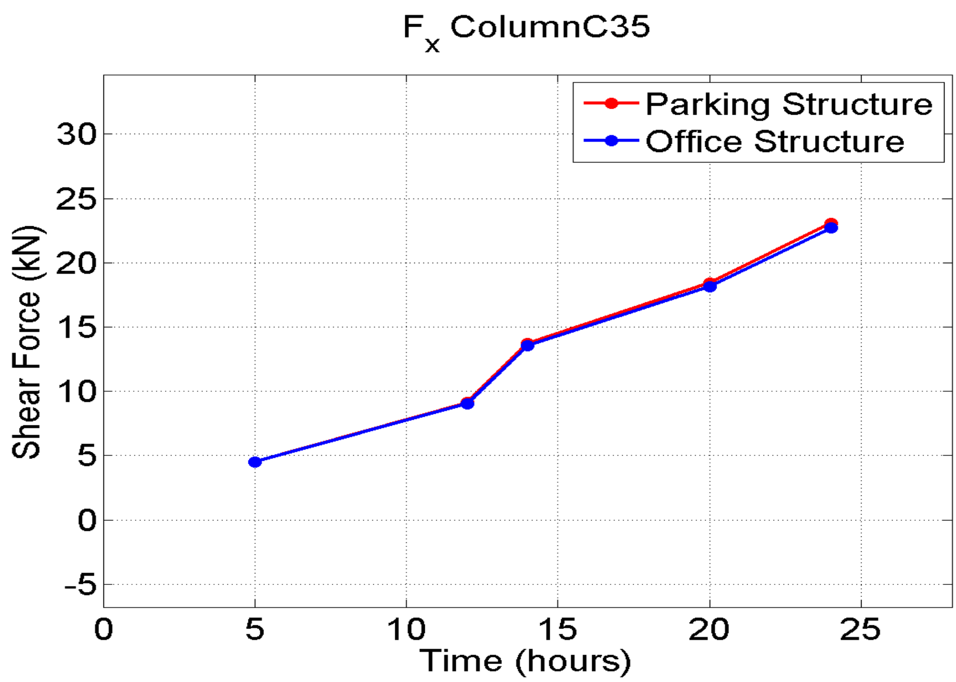

Figure 5-28 Shear Reaction Forces - Column 35

According to Figures 5-27 and 5-28, parking structure is subjected to shear force a little bit greater due to having higher temperature change. Shear force amounts increase with respect to time for both structural components as displacements of the slabs also increase due to thermal load.

5.6. Parallelization Aspect

The parking and office structures were solved by utilizing parallel solution techniques. Each structure has 35595 nodal points and 21580 linear hexahedral elements. In other words, 35595 and 106785 equations were solved by utilizing parallel solution techniques for transient heat transfer and linear static solutions, respectively. Actually, 8640 steps were taken into account for transient heat transfer analysis and 5 static cases were performed during the solution. Indeed, for linear static analysis algorithm, MUMPS library parallelizes the solution; whereas, transient heat transfer analysis algorithm uses MPI for partitioning of the model. Parallel performance of the solution of case study is presented in Figure 5-29.

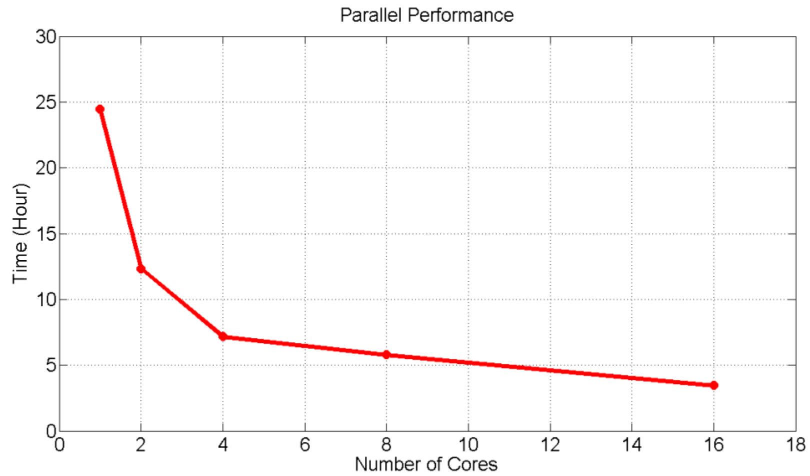

Figure 5-29 Parallel Performance of Solution Algorithm

According to the Figure 5-29, parallelization techniques provide a speed-up approximately 7 times with respect to the performance of one core. Parallel performance of initialization and one step duration of the transient heat transfer solution algorithm are presented in Figure 5-30.

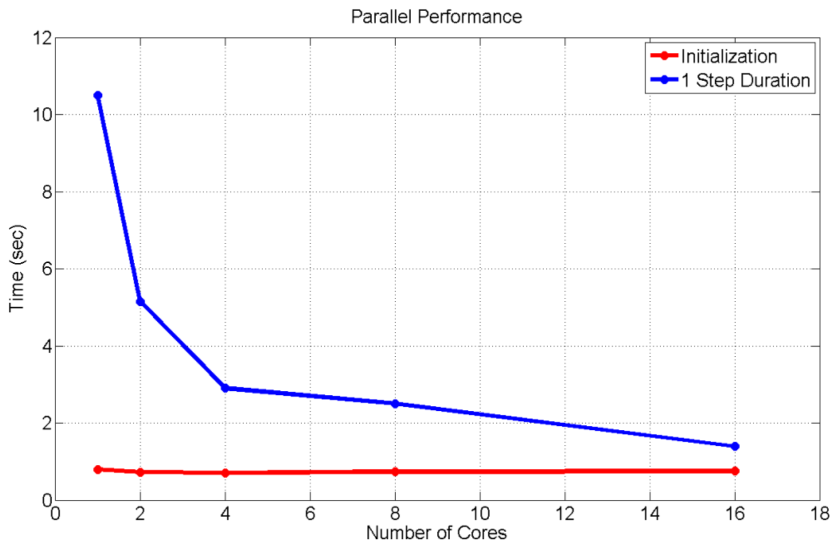

Figure 5-30 Parallel Performances of Initialization and Duration of One Step

According to Figure 5-30, initialization time is the same for each parallel solution. Whereas, the one step duration reduces up to 7.5 times with respect to the solution with one core.

CHAPTER 6

CONCLUSION AND FUTURE PLANS

6.1. Conclusion

For this study, coupled analysis with thermal and structural analysis, methods were implemented. Moreover, two and three dimensional finite elements having capability of both heat transfer and structural analysis solutions were developed and their performances for several benchmark problems were verified. Finally, top floors of two typical L-shaped structures, parking and office buildings, were analyzed by utilizing coupled analysis and results of these two structures were compared.

According to the verification results of finite elements for structural analysis problems, the following conclusions were obtained. First, linear elements represent axial extension behavior better; whereas, under shear-bending and pure bending loading conditions, quadratic elements have better performance. For shear-moment or pure moment related problems, the behavior of linear elements may be improved by utilizing finer mesh.

Distortion on elements reduces the accuracy and parallelogram shaped distortion for linear element is more reliable than the trapezoidal shaped distortion; whereas, for quadratic elements, accuracy of trapezoidal element is greater. According to results of verification problems, quadrilateral elements behave more flexible then the triangular ones since triangular elements have high stiffness at mutual nodes.

For problems having negligible action in out-of-plane direction, the behavior of hexahedron element become the same with the quadrilateral element. Accordingly, for such situations, using quadrilateral element reduces the computational cost. However, if action in the out-of plane direction cannot be ignored, hexahedral elements behave stiffer than the quadrilateral elements.

Applying non-uniform loading on meshed cross – section of an element behaves more flexible for axial extension condition since the assumption of “plane section remains plane” is not valid for that section. Finally, wedge and tetrahedral elements may be preferred for modeling of irregular geometries. Because they are stiffer than hexahedral elements; accordingly, finer meshing is required to improve the behavior.

In general, heat transfer behaviors of finite elements are similar to the structural analysis ones. Since the temperature gradient is not linear, quadratic elements represent the actual behavior better. Similarly, utilizing finer mesh provides closer results to the analytical results. Behaviors of 2D and 3D elements are the same if temperature gradient through the third axis is assumed to be equal to zero. Finally, performance of triangular element is better than the quadrilateral one as having finer mesh for triangular element provides more accurate calculation of thermal body loads such as heat convection or surface flux etc.

Finally, two L-shaped structures, parking and office structures, under different thermal loading were analyzed. According to the results, parking structure is subjected to higher stress amounts due to having higher temperature change. Moreover, for both structures, critical stresses occur at location where the displacements are restrained; accordingly, at regions between inner corner of the L-shape and shear walls, maximum compressive stress occurs. If this region is small, the stress amount is high; whereas, for large regions, compressive stress is distributed to the region.

6.2. Future Plans

This study has some limitations in order to simplify the procedure. However, by utilizing some improvements, more accurate results may be obtained. These improvements are presented below.

- **Modeling Improvement:**

  Since the linear element is not sufficient for calculation of stresses, increasing mesh or using higher order finite elements should be used to get better stress density. As discussed in "Verification Chapter", linear hexahedral element is subjected to shear locking; accordingly, stress distribution does not represent the actual behavior. This problem may be handled by increasing number of elements or utilizing higher order finite element. Quadratic hexahedral element provides better temperature distribution through the thickness and stress distribution over the slab.

- **Ambient Conditions**

  In this study, radiation condition was ignored. However, radiation effect provides increase in temperature on top faces of the slabs and more significant temperature gradient through thickness may occur. Especially, for parking structures, radiation effect hinders the occurring of the same temperature values on top and bottom layer. Accordingly, stress distribution may become more significant.

- **Ambient Conditions for Columns and Walls**

  For the solution of L-shaped structures, heat convection occurring on faces of columns and walls was ignored. However, temperature gradient through thickness of outer columns and walls induce additional bending for those elements and accordingly additional internal forces in vertical elements and stresses on horizontal elements.

- **Nonlinear Material**

  For solution of both physics problems, heat transfer and structural, linear material models were utilized. However, nonlinear behaviors in both solutions represent the actual behavior better. Actually, in heat transfer solution, conductivity of concrete material depends on the temperature. Similarly, elastic properties are related with the temperature, time and loading history. In addition to this, thermal expansion coefficient is a function of temperature. By considering these mechanisms, more reliable results may be obtained.

- **Crack Model**

  Cracking is a complex mechanism for reinforced concrete structures. Although, in general, cracks occur at regions having higher stresses, after cracking, stresses relaxation occurs and the behavior of the structure may change. By implementing the cracking mechanism to the constitutive material model, this complex mechanism may be investigated in details.

By considering all of these conditions, more realistic solution of large structures built with reinforced concrete may be utilized.

REFERENCES

Amestoy P. R., Duff I. S., and Koster J., Mumps: A general purpose distributed memory sparse solver,_ in In Proc. PARA2000, 5th International Workshop on Applied Parallel Computing, pp. 122_131, Springer-Verlag, (2000)

Bahçecioğlu, T., Albostan, U., Kurç, Ö., (2012, October). *An Extensible Parallel Finite Element Analysis Environment: Panthalassa.* , Ankara.

Borst, R., Peeters, P. P. J. M. (1988). Analysis of Concrete Structures under Thermal Loading. Computer Methods in Applied Mechanics and Engineering 77 (1989 293-310). North-Holland, Elsevier Science Publishers B. V.

Bulut, H., Büyükalaca, O., Yılmaz, A. (n.d.). *Türkiye'nin 15 İli için Bazı İklim Verilerinin Eşitliklerle İfadesi.* Adana. Retrieved November 5, 2012, from http://eng.harran.edu.tr/~hbulut/Makale_MMO_Tesisat.pdf

Chou, C., Cheng, H. (2005). *Analysis of Concrete Joint Movements and Seasonal Thermal Stresses at the Chiang Kai-Shek International Airport.* Journal of the Eastern Asia Society for Transportation Studies (Vol. 6, pp. 1217 – 1230).

Cook, R., D., Malkus, D., S., Plesha, M., E. (1989). *Concepts and Applications of Finite Element Analysis.* (3 ed., p. 172, 199) Canada, John Wiley & Sons Inc.

Dhondt, G. (2004). The Finite Element Method for Three-Dimensional Thermomechanical Applications. (p. 67-80, 87-90) England, John Wiley & Sons Ltd.

Federal Construction Council, "Expansion Joints in Buildings", Technical Report No. 65, Building Research Advisory Board, Division of Engineering, National Academy of Science, Washington, DC, 1974, 39 pp.

Iqbal, M. (2012). Design of expansion joints in parking structures. *PTI Journal, 8*(1), 22.

Kosmatka, S. H., Kerkhoff, B., Panarese, W. C. (2003). Design and Control of Concrete Mixtures. Portland Cement Association (14 ed., p. 8) Illinois, USA.

Kurç, Ö., Polat, U., Bahçecioğlu, T., Albostan, U., Kurt, T., Lüleç, A., Özmen, S. (2012, October). *Yapı Mekaniği için Genişletilebilir Paralel Sonlu Elemanlar Çözümleme Platformu.* Ankara

Lewis, R. W., Nithiarasu, P., & Seetharamu, K. N. (2004). *Fundamentals of the finite element method for heat and fluid flow.* (p.4) John Wiley & Sons Ltd.

Li, X., Ma, S., Hou, X. (2009). Deflection and Stress Analysis of Concrete Slab under Temperature and Axle Load Coupling. GeoHunan International Conference (2009) New Technologies in Construction and Rehabilitation of Portland Cement Concrete Pavement and Bridge Deck Pavement. Retrieved from www.ascelibrary.org

MacNeal, R. H., Harder, R. C. (1985). *A Proposed Set of Problems to Test Finite Element Accuracy*. Finite Element in Analysis and Design (Vol. 1, p. 3-20). North Holland.

PTI DC20.7-01 Design Construct & Maintenance CIP PT Concrete Parking Struct. Retrieved November 5, 2012, from http://www.post-tensioning.org/product/x_zkTPk3lGcmcY2lkPT/Design

Reddy, J. N., Gartling, D. K. (2010). The Finite Element Method in Heat Transfer snd Fluid Dynamics. (3 ed., p. 76-81, 139-141) CRC Press, Boca Raton.

Saetta, A., Scotta, R., Vitaliani, R. (n.d.). *Stress Analysis of Concrete Structures Subjected to Variable Thermal Loads.* Journal of Structural Engineering.

Thelanderson, S. (1987). *Modeling of Combined Thermal and Mechanical Action in Concrete*. Journal of Eng. Mech. (113:893-906). Retrieved from www.ascelibrary.org

TS500/2000 February. *Requirements for Design and Construction of Reinforced Concrete Structures.*

Vecchio, F. J. (1987). *Nonlinear Analysis of Reinforced Concrete Frames Subjected to Thermal and Mechanical Loads*. ACI Structural Journal (84-S51).

Vecchio, F. J., Agostino, N., Angelakos, B. (1992). *Reinforced Concrete Slabs Subjected to Thermal Loads.*

(2001). Wessel D. J. (Ed) ASHRAE Fundamentals Handbook. (p. 25.8).

(2009). *Coupled-Field Analysis Guide* (Release 12). USA: ANSYS, Inc. Retrieved May 10, 2011, from http://www1.ansys.com/customer/content/documentation/121/ans_cou.pdf

APPENDIX A

INTEGRATION POINTS

A.1. Integration Points for Line Element

To calculate line integrals, 'Gauss Quadrature Rule' is used. It is possible integrate a function whose limits are from -1 to 1 by using Gauss Quadrature Rule. In other words, any line integral can be calculated numerically by transforming the limits to the limits stated above.

$$I = \int_{L1}^{L2} f\, dx = \int_{-1}^{1} G\, d\xi = \sum_{i=1}^{n} Wi\, Gi \qquad \text{(A-1)}$$

Where n: Number of integration points

It is important to choose appropriate order with rule of (2n-1). In fact, Gauss Quadrature method has acceptable accuracy of functions with order of (2n-1) if n integration points are taken into account (Cook et al. 1989).

Table A-1 Integration Point Scheme for Line Element

Total Number of Points	Location (ξi)	Number	Weight Factor (Wi)
2	$\pm\frac{1}{\sqrt{3}}$	2	1
3	$\pm\sqrt{0.6}$	2	$\frac{5}{9}$
	0	1	$\frac{8}{9}$

Where $-1 < \xi < 1$

A.2. Integration Points for a Quadrilateral Element

It is possible to consider that there are two line integrals through two different axes x and y in order to handle rectangular surface integral, numerically. In other words, the location of integration points and their weights are obtained by combining these two line integral parameters. Hence, the limits of both integrals are again from -1 to 1. These parameters are tabulated at table A.2.

Table A-2 Integration Point Scheme for Quadrilateral Element

Total Number of Points	Location (ξi, ηi)	Number	Weight (Wi)
4	$\pm\frac{1}{\sqrt{3}}, \pm\frac{1}{\sqrt{3}}$	4	1
9	$\pm\sqrt{\frac{3}{5}}, \pm\sqrt{\frac{3}{5}}$	4	$\frac{25}{81}$
	$0, \pm\sqrt{\frac{3}{5}}$	4	$\frac{40}{81}$
	0, 0	1	$\frac{64}{81}$

Where -1 < ξ < 1 and -1 < η < 1

A.3. Integration Points for Triangular Element

For triangular surface integrals, it is not acceptable to use Gauss Quadrature Rule. Because of this, new definition is needed for the 'Quadrature Rule'. According to Quadrature Rule, the limits are from 0 to 1, different from the previous ones. The locations of the integration points and the consistent weights are listed at table A.3.

Table A-3 Integration Point Scheme for Triangular Element

Total Number of Points	Location (ξi, ηi)	Number	Weight Factor (Wi)
1	0, 0	1	1
3	0, 0.5	2	$\frac{1}{3}$
	0.5, 0.5	1	$\frac{1}{3}$
6	0.816847, 0.091576	2	0.109951
	0.091576, 0.091576	1	0.109951
	0.108103, 0.445948	2	0.223381
	0.445948, 0.445948	1	0.223381

Where 0 < ξ < 1 and 0 < η < 1

A.4. Integration Points for Hexahedral Element

Similar to rectangular surface integral, it is possible to use Gauss Quadrature Rule multiple times in order to calculate volume integral of hexahedral element. In fact, three line integrations through local axes, x, y, and z, are needed. Therefore, the location of integration points and their weight factors can be calculated by using the ones stated at table A.1.

Table A-4 Integration Point Scheme for Hexahedral Element

Total Number of Points	Location (§i, ηi, Ϛi)	Number	Weight Factor (Wi)
8	$\pm\frac{1}{\sqrt{3}}, \pm\frac{1}{\sqrt{3}}, \pm\frac{1}{\sqrt{3}}$	8	1
27	$\pm\sqrt{\frac{3}{5}}, \pm\sqrt{\frac{3}{5}}, \pm\sqrt{\frac{3}{5}}$	8	$\frac{125}{729}$
	$0, \pm\sqrt{\frac{3}{5}}, \pm\sqrt{\frac{3}{5}}$	12	$\frac{200}{729}$
	$0, 0, \pm\sqrt{\frac{3}{5}}$	6	$\frac{320}{729}$
	0, 0, 0	1	$\frac{512}{729}$

Where $-1 < \xi < 1$, $-1 < \eta < 1$, and -1 < Ϛ <1

A.5. Integration Points for Wedge Element

Table A-5 Integration Point Scheme for Wedge Element

Total Number of Points	Location (§i, ηi, Ϛi)	Number	Weight Factor (Wi)
2	$\frac{1}{3}, \frac{1}{3}, \frac{1}{3}, \pm\frac{1}{\sqrt{3}}$	2	$\frac{1}{2}$
9	$\frac{1}{6}, \frac{1}{6}, \frac{4}{6}, \pm\sqrt{\frac{3}{5}}$	6	$\frac{5}{54}$
	$\frac{1}{6}, \frac{1}{6}, \frac{4}{6}, 0$	3	$\frac{8}{54}$
18	$\frac{1}{6}, \frac{1}{6}, \frac{4}{6}, \pm\sqrt{\frac{3}{5}}$	6	$\frac{1}{12}$
	$\frac{1}{6}, \frac{1}{6}, \frac{4}{6}, 0$	3	$\frac{2}{15}$
	$\frac{1}{2}, \frac{1}{2}, 0, \pm\sqrt{\frac{3}{5}}$	6	$\frac{1}{108}$
	$\frac{1}{2}, \frac{1}{2}, 0, 0$	3	$\frac{2}{135}$

Where $0 < \xi < 1$, $0 < \eta < 1$, and $0 < \varsigma < 1$

A.6. Integration Points for Tetrahedral Element

Table A-6 Integration Point Scheme for Tetrahedral Element

Total Number of Points	Location (ξ_i, η_i, ς_i, $1-\xi_i-\eta_i-\varsigma_i$)	Number	Weight Factor (Wi)
1	$\frac{1}{4}, \frac{1}{4}, \frac{1}{4}, \frac{1}{4}$	1	$\frac{1}{6}$
4	$\frac{5-\sqrt{5}}{20}, \frac{5-\sqrt{5}}{20}, \frac{5-\sqrt{5}}{20}, \frac{5+3\sqrt{5}}{20}$	4	$\frac{1}{24}$
15	$\frac{1}{4}, \frac{1}{4}, \frac{1}{4}, \frac{1}{4}$	1	$\frac{16}{810}$
	$\frac{7-\sqrt{15}}{34}, \frac{7-\sqrt{15}}{34}, \frac{7-\sqrt{15}}{34}, \frac{13+3\sqrt{15}}{34}$	4	$\frac{2665+14\sqrt{15}}{226800}$
	$\frac{7-\sqrt{15}}{34}, \frac{7-\sqrt{15}}{34}, \frac{7-\sqrt{15}}{34}, \frac{13+3\sqrt{15}}{34}$	4	$\frac{2665-14\sqrt{15}}{226800}$
	$\frac{10-2\sqrt{15}}{40}, \frac{10-2\sqrt{15}}{40}, \frac{10+2\sqrt{15}}{40}, \frac{10+2\sqrt{15}}{40}$	6	$\frac{20}{2268}$

Where $0 < \xi < 1$, $0 < \eta < 1$, and $0 < \varsigma < 1$

APPENDIX B

INPUT FORMAT OF PANTHALASSA

```
<ptlx version="8" solution_space="000111">

    <MaterialModel id="1" plugin="linear_material" E="33000000" Mu="0.2" conductivity_x="1.5" conductivity_y="1.5" conductivity_z="1.5" specific_heat="1000.0" convection_coeff="15.0" density="2400.0" thermal_expansion="0.00001" Sy="0.0" Et="0.0"/>

    <Process rank="all">

        <Structure id="0">

            <Nodes>

                <Node id="1" x="0.0" y="0.0" z="0.0"/>

                <Node id="2" x="0.5" y="0.0" z="0.0"/>

                <Node id="3" x="1.0" y="0.0" z="0.0"/>

                <Node id="4" x="1.5" y="0.0" z="0.0"/>

                <Node id="5" x="2.0" y="0.0" z="0.0"/>

                <Node id="6" x="2.5" y="0.0" z="0.0"/>

                <Node id="7" x="3.0" y="0.0" z="0.0"/>

                <Node id="8" x="3.5" y="0.0" z="0.0"/>

            </Nodes>


            <Elements plugin="Brick8" material="1">

                <Element id="1" nodes="1,42,43,2,3978,4019,4020,3979"/>

                <Element id="2" nodes="2,43,44,3,3979,4020,4021,3980"/>

                <Element id="3" nodes="3,44,45,4,3980,4021,4022,3981"/>

                <Element id="4" nodes="4,45,46,5,3981,4022,4023,3982"/>

            </Elements>


            <LoadingCondition id="1">

                <!-- Restraints -->

                <NodeLoad id="1" type="Restraint" nodes="31844,31845,31846,31847,31872" dimensions="000111">

                </NodeLoad>
```

```
<!-- Initial Temperatures -->
<NodeLoad id="2" type="Temperature" nodes=" 1, 2, 3, 4, 5" dimensions="000001">
<Step magnitude="287.15" time="0.000000">
</Step>
</NodeLoad>

<!-- Top Surface Convection -->
<ElementLoad id="1" type="HeatConvection" elements="3841, 3842" dimensions="000001" matrix_dim="1,5">
<Step magnitude="[5 6 7 8 298.139500;]" time="0.000000"/>
<Step magnitude="[5 6 7 8 298.139500;]" time="3891.024000"/>
<Step magnitude="[5 6 7 8 298.013200;]" time="3891.024000"/>
</ElementLoad>

</LoadingCondition>

<LoadCombo id="1">
<LoadingCondition id="1" multiplier="1.0">
</LoadingCondition>
</LoadCombo>
</Structure>
</Process>

<Analyzer force_create_temperature="true">
<TimeTable start_time="0.000000">
<TimeLine sithe="85860.50000" delta="400.00000">
</TimeLine>
</TimeTable>

<!-- Transient Heat Transfer (0 - 5 hours) -->
<Algorithm id="1" plugin="heat_transfer" analysis_type="transient_explicit_parallel" start_time="0.000000" end_time="18000.000000" structure="0" loadcombo="1" OutputFolder="d:\\utku\\Output\\case_study\\Brick8_21580_Adana_parking">
```

```
</Algorithm>

<!-- Linear Static (@ 5th hour) -->

<Algorithm id="2" plugin="mumps_linear_static" apply_temp_loads="true" start_time="18000.000000" end_time="18000.000000" structure="0" loadcombo="1">

</Algorithm>

<!-- Transient Heat Transfer (5 - 12 hours) -->

<Algorithm id="3" plugin="heat_transfer" analysis_type="transient_explicit_parallel" is_continue="true" previous_id="1" start_time="18000.0001000" end_time="43200.000000" structure="0" loadcombo="1" OutputFolder="d:\\utku\\Output\\case_study\\Brick8_21580_Adana_parking">

</Algorithm>

<!-- Linear Static (@ 12th hour) -->

<Algorithm id="4" plugin="mumps_linear_static" apply_temp_loads="true" start_time="43200.0000000" end_time="43200.000000" structure="0" loadcombo="1">

</Algorithm>

<Tracker id="1" plugin="nodal" output_file="d:\utku\Output\case_study\Brick8_21580_office_Output.nodal" nodes="1">

<TimeTable start_time="0.0">

<TimeLine sithe="1.0" delta="1.0">

</TimeLine>

</TimeTable>

</Tracker>

</Analyzer>


</ptlx
```

APPENDIX C

OUTPUT FORMAT OF PANTHALASSA


```
<VTKFile type="UnstructuredGrid" version="0.10000000000000001" byte_order="LittleEndian">
	<UnstructuredGrid>
		<Piece NumberOfPoints="35595" NumberOfCells="21580">
			<PointData>
				<DataArray Name="displacement" type="Float32" format="ascii" NumberOfComponents="6">0.000163634 9.48534e-005 -2.785e-005 0 0 0 0.000169823 6.49232e-005 -6.46195e-006 0 0 0 </DataArray>
				<DataArray Name="temperature" type="Float32" format="ascii" NumberOfComponents="1">0.222224 0.221567 </DataArray>
				<DataArray Name="avg_stress_at_nodes" type="Float32" format="ascii" NumberOfComponents="6">183126 232641 -992720 88564.5 -461962 -393456 429308 194578 59900.4 17884.4 -258331 -222645 </DataArray>
			</PointData>
			<CellData/>
			<Points>
				<DataArray Name="" type="Float32" format="ascii" NumberOfComponents="3">0 0 0 0.5 0 0 </DataArray>
			</Points>
			<Cells>
				<DataArray Name="connectivity" type="Int32" format="ascii" NumberOfComponents="1">0 41 42 1 3977 4018 4019 3978 1 42 43 2 3978 4019 4020 3979 </DataArray>
				<DataArray Name="offsets" type="Int32" format="ascii" NumberOfComponents="1">8 16 </DataArray>
				<DataArray Name="types" type="UInt8" format="ascii" NumberOfComponents="1">12 12 </DataArray>
			</Cells>
		</Piece>
	</UnstructuredGrid>
</VTKFile>
```